

8-2017

Improvements in four-dimensional and dual energy computed tomography

Rachael M. Martin

Follow this and additional works at: https://digitalcommons.library.tmc.edu/utgsbs_dissertations



Part of the [Analytical, Diagnostic and Therapeutic Techniques and Equipment Commons](#), [Oncology Commons](#), and the [Other Physics Commons](#)

Recommended Citation

Martin, Rachael M., "Improvements in four-dimensional and dual energy computed tomography" (2017). *The University of Texas MD Anderson Cancer Center UTHealth Graduate School of Biomedical Sciences Dissertations and Theses (Open Access)*. 796.
https://digitalcommons.library.tmc.edu/utgsbs_dissertations/796

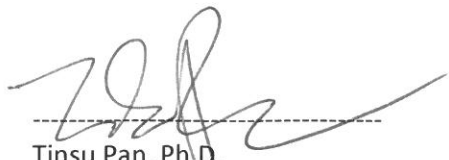
This Dissertation (PhD) is brought to you for free and open access by the The University of Texas MD Anderson Cancer Center UTHealth Graduate School of Biomedical Sciences at DigitalCommons@TMC. It has been accepted for inclusion in The University of Texas MD Anderson Cancer Center UTHealth Graduate School of Biomedical Sciences Dissertations and Theses (Open Access) by an authorized administrator of DigitalCommons@TMC. For more information, please contact digitalcommons@library.tmc.edu.

IMPROVEMENTS IN FOUR-DIMENSIONAL AND DUAL ENERGY COMPUTED TOMOGRAPHY

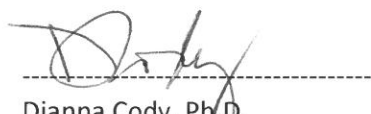
by

Rachael Marianne Martin, B.S.

APPROVED:



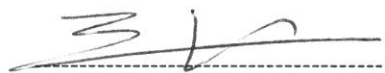
Tinsu Pan, Ph.D.
Advisory Professor



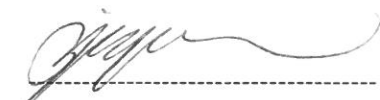
Dianna Cody, Ph.D.



Laurence Court, Ph.D.



Jinzhong Yang, Ph.D.



Ying Yuan, Ph.D.

APPROVED:

Dean, The University of Texas
MD Anderson Cancer Center UTHealth Graduate School of Biomedical Sciences

IMPROVEMENTS IN FOUR-DIMENSIONAL AND DUAL ENERGY COMPUTED TOMOGRAPHY

A

DISSERTATION

Presented to the Faculty of

The University of Texas

MD Anderson Cancer Center UTHealth

Graduate School of Biomedical Sciences

in Partial Fulfillment

of the Requirements

for the Degree of

DOCTOR OF PHILOSOPHY

by

Rachael Marianne Martin, B.S.

Houston, Texas

August 2017

ACKNOWLEDGEMENTS

I would first of all like to thank my advisor, Dr. Tinsu Pan for providing guidance through insightful discussions and encouraging me to make the most out of my graduate school experience. I would also like to thank my current and past committee for providing input that has improved the quality of my research.

A number of fellow graduate students have contributed to this work. Chief among them is Dr. Ashley Rubinstein for helping with small animal scans on and answering questions about the small animal irradiator used in this work and Dr. Moiz Ahmad for providing cone-beam CT reconstruction code and patiently and skillfully answering questions about cone-beam CT.

I would also like to thank the Small Animal Imaging Facility staff for their help in using the small animal irradiator and GE Healthcare employees for assistance in using and understanding the data driven 4D CT product tested in this work. Another deserving acknowledgement is Dr. Geoffrey Hugo from Virginia Commonwealth University for providing long scan cone-beam CT data.

Funding support for this work was provided in part by the Cancer Prevention Research Institute of Texas and through MD Anderson Cancer Center support grants.

Finally, I would like to thank my family for all their support and encouragement along the way.

IMPROVEMENTS IN FOUR-DIMENSIONAL AND DUAL ENERGY COMPUTED TOMOGRAPHY

Rachael Marianne Martin, B.S.

Advisory Professor: Tinsu Pan, Ph.D.

Dual energy and 4D computed tomography (CT) seek to address some of the limitations in traditional CT imaging. Dual energy CT, among other purposes, allows for the quantification and improved visualization of contrast materials, and 4D CT is often used in radiation therapy applications as it allows for the visualization and quantification of object motion. While much research has been done with these technologies, areas remain for potential improvement, both in preclinical and clinical settings, which will be explored in this dissertation. Preclinical dual energy cone-beam CT (CBCT) can benefit from wider separation between the peak energy of the two energy spectra. Using simulations and an x-ray source with a wide kVp range the contrast to noise ratio and Iodine concentration accuracy and precision were determined from Iodine material images. Improvements of 80% in CNR and 58% in precision were observed in the optimal energy pair of 60kVp/200kVp compared to a standard energy pair of 80kVp/140kVp. In 4D imaging, using projection data to obtain the required respiratory signal (“data driven”) can reduce setup complexity and cost of preclinical respiratory monitoring and reduce clinical 4D CT artifacts. Several clinical data driven 4D CBCT methods were modified for mice. Errors in projection sorting were within 4% of a breathing phase and were statistically less than the previous method for data driven 4D CBCT in mice. In clinical 4D CT, semi-automatically drawn target volumes and artifacts were compared between data driven and standard 4D CT images. Target volumes were shown to be statistically at least as large as standard contours, and artifacts were significantly reduced using the data driven

technique. 4D CBCT is promising for use in evaluating tumor motion immediately prior to radiation treatment, but suffers from under sampling artifacts. An iterative volume of interest based reconstruction (I4D VOI) that aims to reduce artifacts without increases in computation time was compared to several other reconstruction techniques using a long scan patient data set. No statistical difference in tumor motion error was observed between I4D VOI and any of the other reconstruction methods. However, potential improvement over non-iterative VOI was demonstrated and computation time was reduced compared to TV minimization.

Table of Contents

Approval Page.....	i
Title Page.....	ii
Acknowledgements.....	iii
Abstract.....	iv
List of Figures.....	ix
List of Tables	xviii
Chapter 1: Introduction	1
Chapter 2: Optimization of Dual Energy CT for small animal contrast enhanced imaging	21
2.1 Introduction.....	21
2.2 Methods	22
2.2.1 Simulations	22
2.2.2 Simulation calibration.....	24
2.2.3 Image reconstruction and analysis.....	24
2.2.4 Justification for image based material decomposition on the X-RAD.....	25
2.2.5 Image based calibration for Dual Energy CBCT on the X-RAD.....	28
2.2.6 Determining optimal energy pairs.....	30
2.3 Results	32
2.3.1 Simulations	32
2.3.3 Optimal energy pairs	39
2.3.4 Dose dependence	43
2.4 Discussion	45
2.5 Conclusion	48
Chapter 3: Translation of several data driven 4D CBCT techniques to mice.....	49
3.1 Introduction.....	49
3.2 Methods	51
3.2.1 CBCT scanning protocol.....	51
3.2.2 Respiratory signal determination	52
3.2.2.1 Modified Amsterdam shroud method	52
3.2.2.2 Fourier Transform phase method	54
3.2.2.3 Intensity method	55

3.2.2.4 Center of mass method	55
3.2.2.5 Manual method	55
3.2.3 Four dimensional image reconstruction	56
3.2.4 Modified four dimensional imaging	57
3.2.5 Region of interest size variation	57
3.3 Results	58
3.3.1 4D images	58
3.3.2 Modified 4D images.....	58
3.3.3 Mouse breathing patterns.....	59
3.3.4 Qualitative comparison of respiratory signal extraction methods	59
3.3.5 Error in projection sorting	61
3.3.6 Effect of error on detected tumor motion	63
3.3.7 Dependence on ROI size.....	65
3.4 Discussion	68
3.5 Conclusion	73
Chapter 4: Target volume and artifact evaluation of a new data-driven 4D CT	75
4.1 Introduction.....	75
4.2 Methods	76
4.2.1 Patient selection.....	76
4.2.2 4D CT images	78
4.2.3 Comparison of MIP contours.....	79
4.2.4 Comparison of phase images	81
4.2.5 Reproducibility	82
4.3 Results	83
4.3.1 Maximum intensity projection contours:.....	83
4.3.2 Phase image comparison:.....	85
4.3.3 Reproducibility	88
4.4 Discussion	88
4.5 Conclusion	92
Chapter 5: Iterative volume of interest based 4D cone-beam CT.....	93
5.1 Introduction.....	93
5.2 Methods	96

5.2.1 Data acquisition	96
5.2.1.1 CBCT scan	96
5.2.1.2 RPM respiratory signal	97
5.2.1.3 Projection reduction method and gold standard	97
5.2.2 Reconstructions	98
5.2.2.1 I4D VOI reconstruction	98
5.2.2.2 FDK reconstruction	102
5.2.2.3 FDK VOI reconstruction	102
5.2.2.4 Unconstrained TV minimization reconstruction	102
5.2.3 Registration technique	104
5.2.4 One minute scan time reconstructions	107
5.3 Results	107
5.3.1 Image quality	107
5.3.2 Trajectory errors	111
5.3.3 One minute scan time	113
5.3.4 Computation time	117
5.4 Discussion	119
5.5 Conclusion	122
Chapter 6: Discussion	123
Bibliography	130
Vita	142

List of Figures

Figure 1: Schematic illustrating the difference between fan beam (left) and cone beam (right) geometry in CT imaging.....	3
Figure 2: Mass attenuation curves for water and Iodine illustrating the different energy dependencies of the attenuation coefficients. This difference allows the materials to be separated using dual energy scanning	5
Figure 3: Comparison of dual energy with a small (a) and large (b) energy separation. As in Figure 2, water attenuation curves are shown in blue and Iodine in red. Dotted lines indicate the mean energies of the low and high energy scans used in each situation. Vertical arrows show the difference in attenuation for each material between the low and high energy scans. As visualized by the relative heights of these arrows, there is a larger difference in the ratio of low to high energy attenuation between water and Iodine when the energy separation is larger.....	8
Figure 4: Iodine material image of a Water (left) and 10mg/mL Iodine (right). An artifact of Iodine along the edge of the water insert is shown due to slight motion of the water insert between scans.	9
Figure 5: Axial (top), coronal (middle), and sagittal (bottom) slices of a mouse at peak inhale (left) and exhale (right) using a 4D VOI reconstruction. The volume of interest contains a tumor and is outlined in dashed yellow lines.	13
Figure 6: Sagittal slice of 4D CT scan where artifacts at bed transition boundaries are evident (black arrows).....	15

Figure 7: Comparison of 3D (a) and 4D phase (b) CBCT axial image. Prominent streak artifacts are present in the phase image due to under-sampling and uneven projection spacing.....	17
Figure 8: Average difference in angle for matching projections in repeated scan for varying frame rate, pixel binning and rotation rate.	26
Figure 9: Average difference in angle for matching projections in repeated scan for varying frame rate, pixel binning and rotation rate once the starting angles were matched and other projection angles shifted accordingly.	27
Figure 10: Schematic of solid water calibration phantom with water 25 mg I/mL (a, d), 5 mg I/mL (b, e), and water (c, f) inserts is shown on the left. A photo of the imaging and calibration setup is shown at right including the x-ray tube and detector of the X-RAD and the phantom.....	29
Figure 11: The energy dependence of dose with data points from manufacturer supplied data scaled to the same mA. The linear fit to this data was used to dose match each of the high and each of the low energy scans.	31
Figure 12: Percent difference in iodine concentration between known and measured concentration for the 20 mgI/ml (a) and 10 mgI/ml (b) inserts in the ray-tracing based simulations. Changes in the high energy of the energy pair are shown along the x-axis and changes in low energy are shown as different curves.	33
Figure 13: Contrast to noise ratio for 25 mgI/ml (a) and 5 mgI/ml (b) inserts compared to background in the ray-tracing based simulations. Changes in the high energy of the energy pair are shown along the x-axis and changes in low energy are shown as different curves.....	34

Figure 14: Simulation generated Iodine images demonstrating the effect of increasing the energy of the high energy scan (top row increasing from left to right) and increasing the energy of the low energy scan (bottom row increasing from left to right). As seen in these images, particularly for the 1 mg I/ml insert (white arrow), contrast to noise increases with increasing high energy kVp and decreasing low energy kVp..... 35

Figure 15: Percent difference in iodine concentration between known and measured concentration for the 30 mgI/ml (a) and 20 mgI/ml (b) inserts of the iodine phantom scanned on the X-RAD. Changes in the high energy of the energy pair are shown along the x-axis and changes in low energy are shown as different curves. 40

Figure 16: Contrast to noise ratio for 5 mgI/ml (a) and 3 mgI/ml (b) inserts compared to background the iodine phantom scanned on the X-RAD. Changes in the high energy of the energy pair are shown along the x-axis and changes in low energy are shown as different curves. 41

Figure 17: Noise levels in high (a) and low (b) energy images. Noise is taken as the standard deviation in a centrally located ROI in the solid water portion of the phantom. Variations in noise are primarily due to slight variations in dose due to mA rounding. With actual mA used (High dose in Table 2) the dose for high (c) and low (d) energy scans is as shown. 41

Figure 18: Iodine images demonstrating the effect of increasing the energy of the high energy scan (top row increasing from left to right) and increasing the energy of the low energy scan (bottom row increasing from left to right). An increase in CNR with increasing high energy kVp is easily seen in these images, with a less noticeable difference with changing low energy kVp. 42

Figure 19: Comparison of Iodine images for the standard 80/140 kVp pair (a) and optimized 60/200 kVp pair (b). Improvements in CNR are visualized in the optimized image. 43

Figure 20: Dependence of Iodine error on changing the high energy dose with a constant low energy dose of 14 mGy (a) and on changing low energy dose with a constant high energy dose of 6.5 mGy (b). Only 50 kVp energy pairs are included in (b), but similar trends were observed with other low energy kVp..... 44

Figure 21: Dependence of CNR on changing the high energy dose with a constant low energy dose of 14 mGy (a) and on changing low energy dose with a constant high energy dose of 6.5 mGy (b). Only 50 kVp energy pairs are included in (b), but similar trends were observed with other low energy kVp. 44

Figure 22: Diagram of the modified Amsterdam Shroud method showing from left to right the region of interest in the original projection, edge enhanced ROI, horizontal sum, Amsterdam shroud, edge enhanced shroud, and signal..... 53

Figure 23: Sections of respiratory signals obtained using the mAS (top left), FT-p (top right), COM (bottom left), and Intensity (bottom right) methods. The direction of inspiration and expiration is indicated next to the figures (peak inspiration for the mAS method is a valley between two positively oriented peaks)..... 54

Figure 24: Peak expiration images obtained as part of an 8 phase 4D image (a) and a 4 phase modified 4D image (b) are compared against a full 3D reconstruction (c). The only difference observed between (a) and (b) is that there is noticeably less noise and streak artifacts in the modified 4D image. We do not observe differences in motion blurring between the (b) and (c) even though the projections where the diaphragm are moving have been removed from (b)..... 59

Figure 25: Coronal slices at peak inspiration (a-e) and peak expiration (f-j) for the manual (a,f), mAS (b,g), FT-p (c,h), Int (d,i), and COM (e,j) methods of respiratory signal extraction. Horizontal lines are

added to emphasize the difference between inspiration and expiration and to make any differences in diaphragm position between the methods more obvious. No observable differences are noted between images produced by the different methods. 60

Figure 26: Axial slices at peak inspiration (a-e) and peak expiration (f-j) for the manual (a,f), mAS (b,g), FT-p (c,h), Int (d,i), and COM (e,j) methods of respiratory signal extraction. Minor differences are observed between the COM and manual methods and to a lesser extent the FT and manual methods in the peak inspiration images (ex. white arrows). No observable differences are noted between images produced by the different methods for the peak expiration images or between the mAS and Int and manual images. 60

Figure 27: Visual effect of the error in projection sorting on coronal images of the peak inspiration phase. The manual method displayed in (a) is considered ground truth, arrows point to areas where differences were observed in some images, and the horizontal line indicates the top of the diaphragm for the manual method. The effect of increasing the error is shown in the remaining images (errors of 2.5% (b), 6.3% (c), and 13.8% (d)). 63

Figure 28: Graph of tumor position (a) for images with associated sorting errors of 0 (manual), 1.3% (small error), 6.3% (phase shift), and 13.8% (large error). Images at peak inspiration (left) and expiration (right) of the tumor are shown for the manual method (b), phase shift (c), and large error (d). 64

Figure 29: Dependence of the error in projection sorting on ROI height (left) and width (right) for two mice (top and bottom). Error is defined as the average across the projections of the absolute value of the difference between phase bins for the method in question and the manual method. It is expressed as a percentage of the breathing cycle. For width dependence, error is displayed relative

to the error for the full width of a well performing ROI height such that an error of 1 means there is no change in error between that width and the full width. It is observed that while the error for the mAS decreases gradually with ROI height and the error for the Intensity method remains essentially constant, the error for the FT-p and COM methods have relatively high error for small ROIs.

Additionally the mAS and COM show no dependence on width while the error of the FT-p method decreases with decreasing width and the Intensity method shows some dependency on width. 67

Figure 30: Dependence of the standard deviation in projection sorting on ROI height (left) and width (right) for two mice (top and bottom). Standard deviation was calculated by finding the difference in phase bin number between the method in question and the manual method and finding the standard deviation of this quantity for all projections. It is expressed as a percentage of the breathing cycle. The height and width dependence of the standard deviation is similar to that of the error in Figure 29..... 68

Figure 31: Sections of COM method respiratory signals for different height ROIs: 10 (0.7 mm) (a), 20 (1.4 mm) (b) and 50 (3.7 mm) (c) pixels. The black arrows indicate the location of the first peak inspiration which switches from a peak (a) to valleys (b,c) as the ROI size increases. In the transition (b) some peaks become lost to background noise (e.g. white arrow)..... 70

Figure 32: Comparison of IGTVs for standard and data driven method including (a) percent volume differences (negative means data driven is smaller), (b) volumes, (c) Dice Similarity coefficients, and (d) mean surface separation and Hausdorff distance (max separation)..... 84

Figure 33: Axial, sagittal, and coronal (left to right) slices of standard (above) and data driven (below) MIP images for a case (patient 11) with large percent volume difference (-12.1%). The standard contour is shown in red and data driven contour in yellow, both copied to the opposite image for

direct comparison. In this patient, the differences in the contours reflect the visible differences in the tumor shape. 85

Figure 34: Artifact scores for all patients. Positive values indicate the data driven algorithm produced phase images with fewer and/or less severe artifacts, while negative values indicate the standard method is better. 86

Figure 35: Data driven (a, c, and e and g) and standard (b, d, and f and h) phase images for patients (#8, #26, and #6) with artifact scores of +1, -1, and 0.6, respectively. Reduced artifacts are observed in the abdomen and diaphragm/tumor in patients 8 and 6, respectively. In patient 29, the difference in artifacts is not as visible but some improvement in artifacts with the standard method is observed in the circled region. 87

Figure 36: (a) Phase images for standard (upper rows) and data driven (bottom rows) methods for patient 16. Dotted lines show couch position transitions. Artifacts (arrows) in 10%-30% phases for the standard method contribute to a wider center region of the IGTV as shown in (b). (b) shows axial, sagittal, and coronal (left to right) slices of standard (above) and data driven (below) MIP for the same patient. The standard contour is shown in red and data driven contour in yellow, both copied to the opposite image for direct comparison. 90

Figure 37: Iterative 4D volume of interest (I4D VOI) images of peak inhale (a and b) and exhale (c and d) for a patient discontinuities at the edges are obvious without correction (a and c). These discontinuities become less noticeable by removing two voxels isotropically around the border (after reconstructing with a VOI expanded by two voxels) and smoothing the border voxels (b and d). Note that the bright area in the center of the VOI is present in fully sampled images and not an artifact of the I4D VOI reconstruction. 101

Figure 38: Axial, coronal, and sagittal (top, middle, bottom) slices of TV minimization reconstructions for varying values of λ : (a) 0, (b) 2, (c) 5, (d) 10, and (e) 20. 104

Figure 39: Superior-Inferior (a), lateral (b), and Anterior-Posterior (c) tumor trajectories for a patient (P100) with moderate agreement between the gold standard fully sampled FDK and other reconstruction methods. Tumor position for each phase is measured relative to peak exhale (phase angle = π) using rigid registration within the VOI. 106

Figure 40: Axial (a, b), coronal (c, d), and sagittal (e, f) slices of peak inhale (a, c, e) and exhale (b, d, f) for each of the reconstructions (left to right): fully sampled FDK, FDK, Smooth FDK, FDK VOI, Smooth FDK VOI, I4D VOI, TV min ($\lambda=2$), and TV min ($\lambda=10$). Red arrows highlight differences in bony anatomy visualization among various reconstructions. P105 pictured here represents a difficult case of a small mobile tumor. 109

Figure 41: Axial (a, b), coronal (c, d), and sagittal (e, f) slices of peak inhale (a, c, e) and exhale (b, d, f) for each of the reconstructions (left to right): fully sampled FDK, FDK, Smooth FDK, FDK VOI, Smooth FDK VOI, I4D VOI, TV min ($\lambda=2$), and TV min ($\lambda=10$). Red arrows highlight differences in bony anatomy visualization among various reconstructions. Yellow arrows indicate differences between Smooth FDK VOI and I4D VOI. P107 pictured here represents a patient with a relatively large tumor with moderate motion. 110

Figure 42: Tumor trajectories for a patient with good agreement between the gold standard fully sampled FDK and other reconstruction methods (a) and a patient where the registration failed to detect motion in the I4D VOI reconstruction (b). Tumor position for each phase is measured relative to peak exhale (phase angle = π) using rigid registration within the VOI. RMS errors for each

reconstruction and each patient except those two where the registration failed with two or more registration types are shown in (c)..... 112

Figure 43: Axial (a, b), coronal (c, d), and sagittal (e, f) slices of peak inhale (a, c, e) and exhale (b, d, f) for 2 and 1 minute VOI reconstructions from left to right: fully sampled FDK, I4D VOI 2 minutes, Smooth FDK 2 minutes, I4D VOI 1 minute, Smooth FDK VOI 1 minute. P105 pictured here represents a difficult case of a small mobile tumor. Differences between the Smooth FDK VOI and I4D VOI become more apparent for 1 minute scan times (especially seen near yellow arrows). 115

Figure 44: Axial (a, b), coronal (c, d), and sagittal (e, f) slices of peak inhale (a, c, e) and exhale (b, d, f) for 2 and 1 minute VOI reconstructions from left to right: fully sampled FDK, I4D VOI 2 minutes, Smooth FDK 2 minutes, I4D VOI 1 minute, Smooth FDK VOI 1 minute. P108 pictured here represents a difficult case of a small tumor and irregular and long breath cycles. Differences between the Smooth FDK VOI and I4D VOI become more apparent for 1 minute scan times (especially seen near yellow arrows). 116

Figure 45: RMS errors for 1 and 2 minute scan time Smooth FDK VOI and I4D VOI reconstructions. Errors for each patient except P110 and P115 are shown in (a) and average (standard error) RMS errors are shown in (b). 117

List of Tables

Table 1: mA for calibration scans	29
Table 2: The mA for each scan used for DECT at listed high (H), medium (M), and low (L) doses.	32
Table 3: Iodine errors for day 1 calibration coefficients for low energy of 60 kVp applied to the same phantom with different Iodine concentrations and to the Gammex phantom inserts. High (H), medium (M), and low (L) mA are as specified in Table 2.	36
Table 4: Iodine errors for day 1 calibration coefficients for low energy of 80 kVp applied to the same phantom with different Iodine concentrations and to the Gammex phantom inserts. High (H), medium (M), and low (L) mA are as specified in Table 2.	37
Table 5: Averaged percent difference in Iodine error for each calibration day, separated by use of both or one identical concentration calibration sets for the first day and old (same mixture as first day) or new mixtures for subsequent days.	38
Table 6: Averaged standard deviations of Iodine error for 3 repetitions of the calibration using the same mixture and 3 repetitions using different mixtures (of nominally the same concentration).	38
Table 7: Peak number errors (Difference in the number of peaks detected between each tested method and the manual method for each of the 8 mice used in analysis.)	62
Table 8: Height dependence of the number of detected peaks (Difference in the number of peaks detected between each tested method and the manual method)	66
Table 9: Width dependence of the number of detected peaks (Difference in the number of peaks detected between each tested method and the manual method).....	66

Table 10: Patient disease and tumor data	77
Table 11: Contour comparison metrics	84
Table 12: Patient demographic information (*measured from fully sampled FDK)	97
Table 13: RMS error comparison p-values	113
Table 14: Average reconstruction computation time (minutes) for each reconstruction type.....	118

Chapter 1: Introduction

The purpose of this dissertation is to explore several possible improvements in small animal dual energy and 4D CT imaging. These improvements were made on a small animal image guided radiation therapy system known as the X-RAD 225Cx (Precision X-Ray, Inc. North Branford, CT), but the concepts could be applied to other small animal imaging platforms. Additionally, this dissertation aims to test similar techniques to improve 4D imaging in humans for applications in radiation therapy. Improvements made fall broadly into the categories of improving image quality and quantitative accuracy and minimizing time and complexity of the imaging procedures. The purposes and background for each type of small animal and human imaging included in this dissertation will be discussed, along with the specific areas of potential improvement that will be addressed.

Small animal imaging plays an important role in preclinical and basic science research¹, such as non-invasively determining response to experimental treatments, developing new clinical imaging modalities, and image guided radiation treatments. Sometimes imaging modalities, such as bioluminescence imaging, arise from preclinical research and may or may not be translated into clinical practice. Other times clinical imaging modalities are redesigned for use on small animals. Differences between humans and small animals and the goals of imaging require different design focuses for these devices. The small size of these animals requires improvements in spatial resolution over clinical imaging, and their fast cardiac and respiration motion require additional consideration where time is a variable in the image acquisition.

One imaging modality adapted from clinical imaging is small animal computed tomography (CT)²⁻⁴. In CT, x-ray projections through the patient are measured at about 1000 equally spaced angles around the patient. These radiographic projections are then reconstructed into a 3D image. CT projection geometry can either be cone beam or fan beam (Figure 1), indicating the shape of the x-ray beam. Typically in cone-beam CT, one 2D projection is collected at each angle during a single gantry rotation. In fan beam, or multislice CT, the gantry rotates multiple times as the patient couch moves through it (continuously as in helical CT or in a step-and-shoot manner). 2D images are reconstructed at each location along the patient and combined to form a 3D image. Compared to human CT, small animal CT has smaller detector elements and focal spots to get the needed spatial resolution (on the order of 100 μm) and generally slower gantry rotations are used to maintain the needed signal to noise ratio for this spatial resolution²⁻⁴. One small animal CT scanner is the previously mentioned X-RAD 225Cx (X-RAD). The X-RAD is a small animal image guided radiation therapy (IGRT) system that includes cone-beam CT as one form of image guidance. While not optimized for general imaging purposes, the X-RAD offers several advantages to studying small animal imaging including a large x-ray tube energy range and integration with small animal radiation therapy treatments.

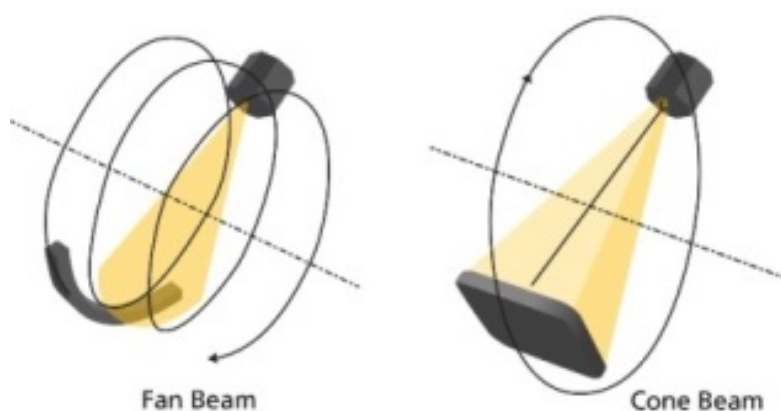


Figure 1: Schematic illustrating the difference between fan beam (left) and cone beam (right) geometry in CT imaging.

Contrast agents are often used in imaging to improve visualization of structures such as blood vessels and tumors as well as visualizing physiological processes. Iodine is a common contrast agent in CT, as its high atomic number leads to high x-ray attenuation compared to surrounding tissue. The fast heartbeat of mice combined with relatively long imaging times, results in traditional iodine contrast agents being mostly cleared before images can be created. Researchers have addressed this problem by enclosing the iodine in liposomes or using other similar techniques resulting in blood pool contrast agents with a long biological half-life⁵. These types of contrast agents have been used for a number of purposes in mice including imaging tumor angiogenesis⁶, and imaging liver^{7,8} and lung tumors⁹. However, with this configuration, injected volumes near the maximum that can safely be injected into mice are required¹⁰. For this reason and due to the high cost of such contrast agents, imaging techniques that minimize the concentration of iodine needed are of interest. One advantage of these contrast agents over traditional iodine contrast agents is that the surface of the liposomes provides allows for the attachment of ligands which can be used as active targeting in addition to the passive targeting by the enhanced permeability and retention effect. Additionally, other molecules, such as drugs, can be enclosed in the liposomes along with the iodine, allowing for the study of pharmacokinetics of such liposome encapsulated drugs. For use as a

targeted contrast agent and in studying pharmacokinetics, a reproducible way of measuring the amount of contrast agent in the area of interest is needed.

Dual energy imaging is one way of improving the visibility of low concentrations of Iodine and of quantifying the Iodine concentration. Dual energy CT was proposed in the early days of CT imaging and relies on the differing energy dependence of different types of x-ray attenuation^{11, 12}. At the energies of x-ray imaging, the two main types of attenuation are through the photoelectric effect and Compton scattering. The photoelectric effect, where the energy of an x-ray is fully transferred to an electron and that atom is then ionized, has a strong dependence on atomic number and strong inverse dependence on the x-ray energy ($\sim Z^3 / E^3$). Therefore, atoms with high atomic number will have a rapid decrease in their attenuation coefficient with increasing energy, as demonstrated by the Iodine attenuation curve in Figure 2. In Compton scattering some of the energy of an x-ray is transferred to an electron, scattering both the electron and now lower energy x-ray. Compton scattering does not have a strong dependence on atomic number or energy, but is instead more directly related to the electron density. Atoms with low atomic numbers will therefore have attenuation properties that are more influenced by Compton scattering and have attenuation coefficients with less dependence on energy than those with high atomic number. The attenuation curve for water, for example, has relatively little change above 50 keV. Another important feature to point out in this graph is the so-called “k-edge” seen in the Iodine curve which is the sudden increase in the attenuation coefficient at the energy that is just enough to ionize inner shell (k-shell) electrons from that atom.

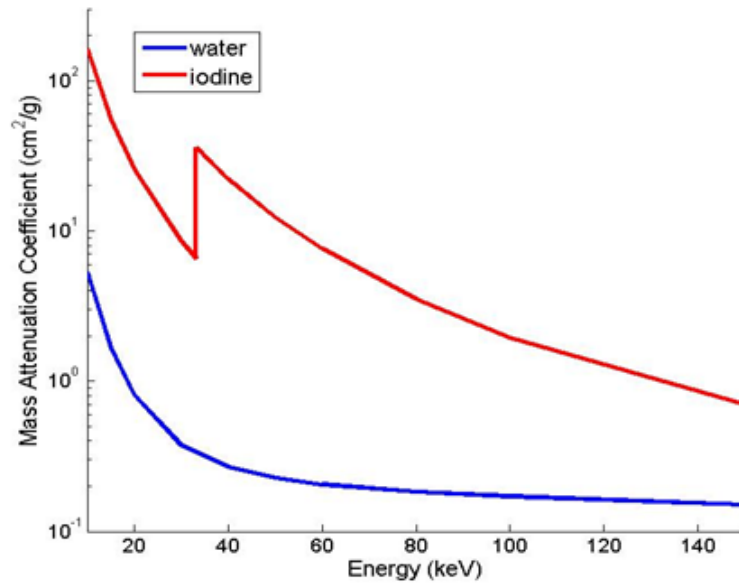


Figure 2: Mass attenuation curves for water and Iodine illustrating the different energy dependencies of the attenuation coefficients. This difference allows the materials to be separated using dual energy scanning

Dual energy CT collects attenuation data using two different energy spectra to take advantage of this difference between different material types. This data can be collected in a number of different ways including sequential scanning at two different kVp, rapidly switching the x-ray tube potential between two different kVp, using two separate x-ray tubes and detectors, using layered detectors that detect different energy ranges, and with photon counting detectors. On the X-RAD system used in this work, only sequential scanning is possible. With appropriate calibration, the data collected from the two scans can be used to create a set of basis images. These basis images can either be the amount of Compton and photoelectric attenuation or the amounts of two materials that have different enough attenuation curves. Using water and Iodine as basis material images, Iodine contrast material can be isolated and quantified in an image. In addition to being able to quantify the Iodine concentration and thereby quantify the contrast agent uptake, with

appropriate noise reduction techniques, lower concentrations of Iodine may be better visualized with dual energy CT than with standard CT imaging. As suggested previously, dual energy therefore has the potential to improve contrast enhanced imaging in small animals.

Dual energy CT in small animals has been applied to a number of applications including three material lung imaging^{9, 13, 14}, observing vascular changes⁶, ex vivo lead based contrast agent imaging¹⁵, bone and iodine separation¹⁶, and measuring effective atomic number and electron density¹⁷. However, it is less well developed or widely used as dual energy CT in humans. In order to create improved dual energy imaging for small animals several factors should be taken into account. One important aspect of dual energy imaging is the peak energy of the energy spectra used. Larger energy spectra separation is expected to improve material image noise levels, and therefore improve low contrast detectability and precision in quantitative measurements¹⁸⁻²⁰. Figure 3 demonstrates the intuitive reasoning behind these expected improvements. Dual energy CT with low spectra separation is demonstrated in (a) and high spectra separation in (b). For each material (water and Iodine) the difference in attenuation coefficient values between the low and high energy mean energy (dotted lines) is shown as a vertical arrow. The calculation of the material images is essentially based upon this difference in attenuation values. When these arrows are close to the same height for different materials, as in (a), distinguishing between the materials in the presence of image noise becomes difficult. A larger separation in mean energy, as in (b), leads to a larger difference in these arrows, making distinguishing between the two materials easier. With improved ability to distinguish between the two materials, noise in the low and high energy image will have less impact on the calculation of the amounts of each material, and therefore to the noise in the material images. The large energy range of the x-ray tube used for the XRAD allows for the possibility of improving small animal dual energy CT by utilizing the higher energies available to increase the energy separation. We aim to optimize the energy pair selection in dual energy CT on

the X-RAD for improved quantitative accuracy and precision in Iodine measurements and low contrast detectability in small animal contrast enhanced imaging.

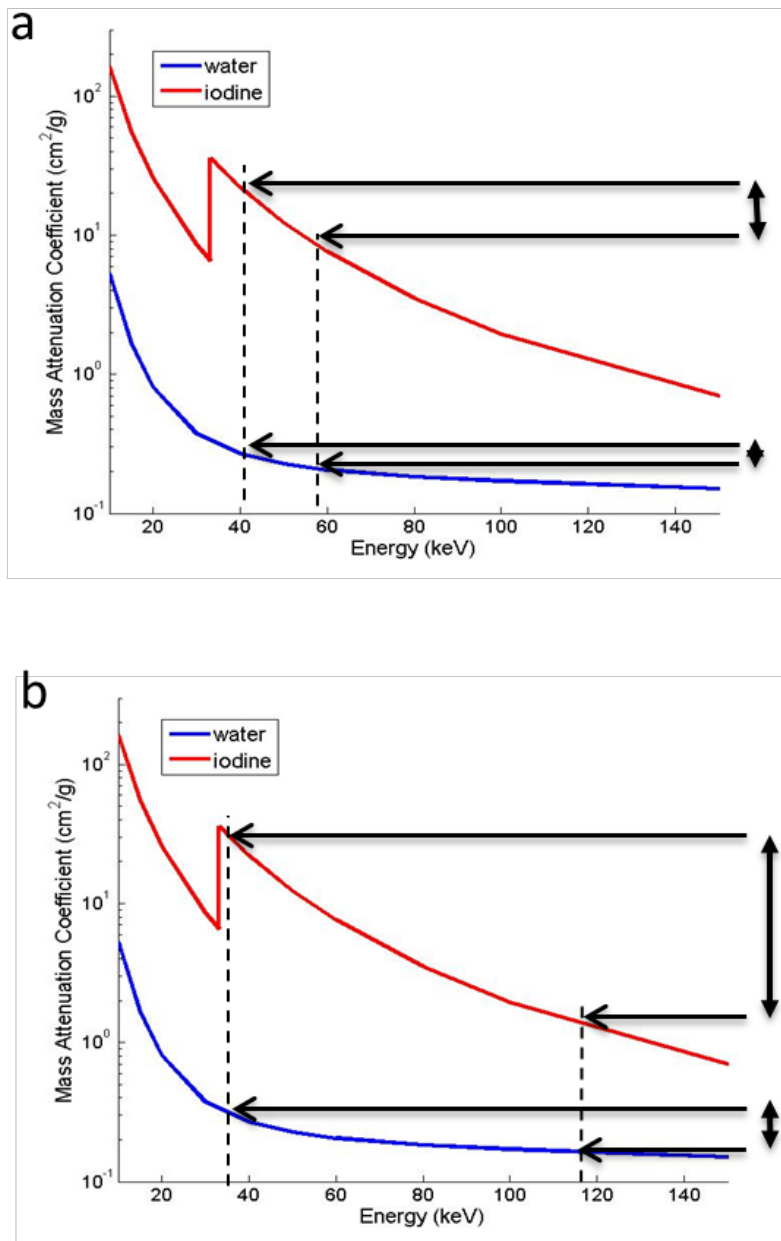


Figure 3: Comparison of dual energy with a small (a) and large (b) energy separation. As in Figure 2, water attenuation curves are shown in blue and iodine in red. Dotted lines indicate the mean energies of the low and high energy scans used in each situation. Vertical arrows show the difference in attenuation for each material between the low and high energy scans. As visualized by the relative heights of these arrows, there is a larger difference in the ratio of low to high energy attenuation between water and iodine when the energy separation is larger.

In order to perform dual energy on a living animal, the motion of that animal should be taken into account. In sequential scanning motion between scans can cause artifacts in the material images, since the dual energy processing assumes that any difference in the attenuation between the two scans is due to changes in the attenuation of the material at different energies and not due to movement. Figure 4 shows an example of this type of artifact in an Iodine material image. Slight motion of a solid water phantom insert between scans resulted in a bright band (showing high Iodine concentration) along the edge of the insert. Motion can be present within each scan, especially in the form of breathing motion. This type of motion will blur each of the scans and the resulting material images. The slow gantry rotation of the X-RAD and other small animal CT systems combined with the rapid breathing of mice leads to more blurring than might be present in a human CT scan. While this blurring does minimize the type of artifacts seen with between-scan motion, it can lead to errors in the quantification and localization of Iodine in moving regions. For this reason, motion management strategies should be employed for dual energy CT imaging of small animals.

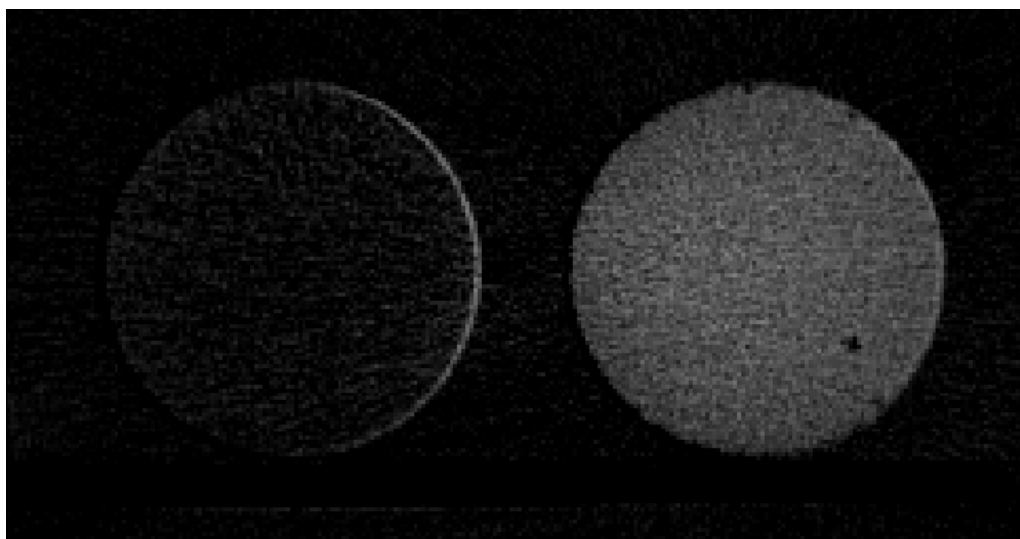


Figure 4: Iodine material image of a Water (left) and 10mg/mL Iodine (right). An artifact of Iodine along the edge of the water insert is shown due to slight motion of the water insert between scans.

There are a number of different strategies for dealing with breathing motion in cone-beam CT imaging. One is through gating, where only images from a portion of the breathing cycle are used. For example, images only from peak exhale may be used in the reconstruction. Gating can be done prospectively, where images are only acquired during a specified portion of the breathing cycle, or retrospectively, where only images from a specified portion of the breathing cycle are used in the reconstruction. Another approach to managing breathing motion is to reconstruct images for each portion of the breathing cycle. When these images are shown sequentially, the motion associated with a representative breathing cycle can be observed. In each of these strategies, a respiratory signal is generally required to correlate the projection data with the phase or amplitude within the respiratory cycle. In prospective gating, a portion of the respiratory cycle is selected for imaging, and whenever the respiratory signal enters into that portion of the cycle, the x-ray tube is turned on and data is acquired, and whenever it leaves that portion of the cycle, the x-ray tube is turned off. This strategy relies on a regular respiratory signal to be able to determine in real time when the signal is entering the desired respiratory phase. Retrospective gating selects only image data associated with a specific portion of the respiratory signal and only uses this data in the reconstruction. In 4D imaging each breathing cycle is divided into sections based on phase or amplitude and the associated projection data is accordingly sorted into bins to be reconstructed. In cone-beam CT systems like the X-RAD, a single slow rotation of the gantry is performed allowing for multiple breath cycles, and the 2D radiographic projections are the image data that is divided into bins. In standard CT imaging, data is collected at each axial position long enough to cover at least one respiratory cycle. Each of these motion management strategies would be effective in reducing motion artifacts in dual energy CBCT and the associated errors in Iodine localization and quantification. Since only projection images associated with a specific portion of the breathing cycle are used for each image, little motion blurring is present within each image.

As suggested above, obtaining a respiratory signal is a critical step in 4D or gated imaging. Some researchers have obtained this signal through a pneumatic cushioning device placed under the mouse.²¹ However, these devices are costly and complicate the setup of the mouse. Another way of obtaining the respiratory signal is by using the projection data itself (data driven 4D imaging) to get the respiratory signal. With this approach, no additional cost or equipment setup is required. Another advantage of data driven imaging is that it is more likely to be correlated to internal motion than an external surrogate, giving images that are more closely tied to the respiratory phase of interest within the lungs and abdomen of the mice. A number of methods have been successfully employed to perform data driven 4D CBCT in human patients²²⁻²⁷; however, these methods have not been previously used in mice. Most data driven 4D CBCT research in mice has focused on step-and-shoot style imaging^{28, 29}, where the gantry is left at each location long enough to get at least one respiratory signal before moving. To our knowledge, only one previous data driven 4D CBCT method³⁰⁻³² has been attempted in mice using a continuously rotating gantry. We aim look for improvements in the accuracy of phase bin sorting over this method by translating several of the data driven methods used in humans into mice.

Thus far we have been discussing 4D CBCT imaging in mice with the intended purpose of improving motion artifacts in dual energy CBCT. However, 4D CBCT imaging can be used for other purposes as well. An important application of 4D imaging in humans is in motion management in radiation therapy. Since the X-RAD is an image guided radiation therapy platform, 4D CBCT imaging on the X-RAD can be used for similar purposes. Motion management in small animal radiation treatments has not been used extensively. This limited use is partly the result of the limited capabilities for targeted radiation treatments in previous small animal irradiators. More recently, several high precision radiation treatment platforms have become available for mice³³. The X-RAD is among this group, with targeting accuracy of $200\ \mu\text{m}$ ³⁴. These platforms allow for the study of the

effects of radiation on tumors and normal tissues in circumstances more closely mimicking human treatments. With precise targeting of the tumor comes the need to account for its movement due to respiration. Forced breathhold of the mouse is one strategy to address the problem of motion, effectively freezing the motion. However, the specialized equipment needed to perform the breathhold may not be available or needed if motion is small. 4D CBCT can be used for the purpose of evaluating the motion of the tumor prior to treatment to decide if a breathhold treatment strategy is necessary. If the motion is small enough, 4D CBCT can be used to plan a treatment area that includes the full motion path of the tumor, similar to what is done for many human treatments. Furthermore, for treatments that are divided into multiple days, 4D CBCT can be used to determine if the motion of the tumor still lies within the target area on subsequent treatment days. Generally, in each of these applications, only the motion near the tumor is of interest. Applying a strategy proposed by Ahmad et al³⁵, reconstruction time can be saved by only performing the 4D reconstruction within a volume of interest. Outside the volume of interest, a 3D reconstruction is performed, allowing for better image quality in this region to allow for better alignment of the image to previous days' images. This strategy was applied to several mice as shown in Figure 5. However, not enough small animal data was available to test this technique quantitatively in mice. We will conduct further testing with a human 4D CBCT data set, which will be described later in the introduction.

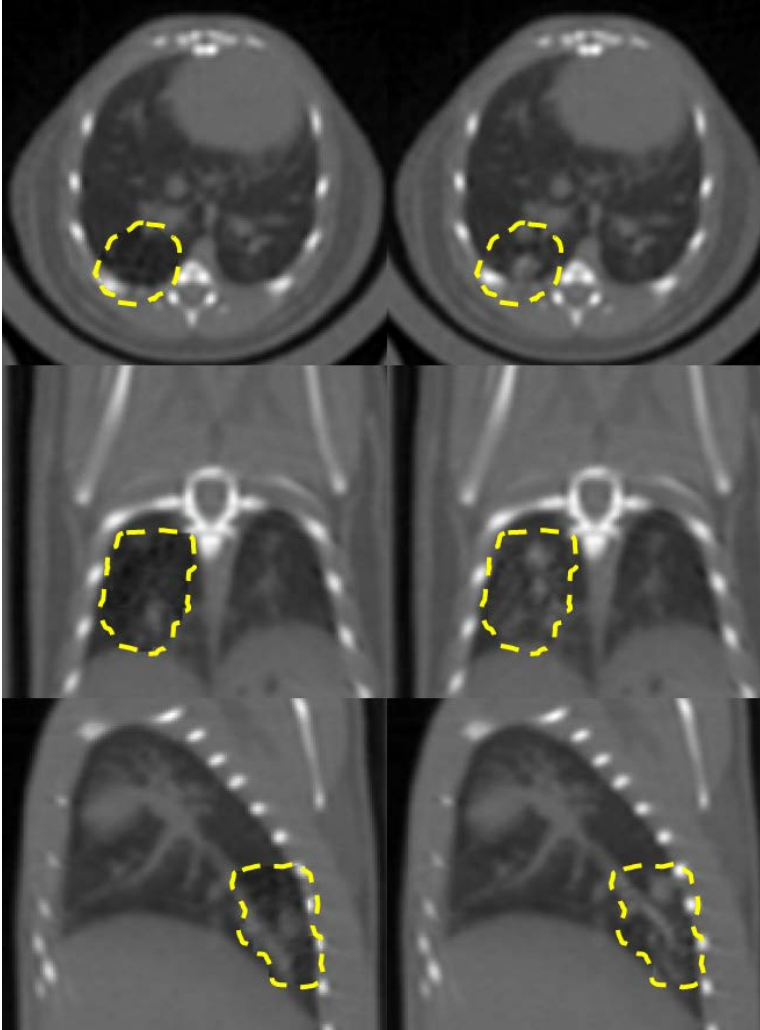


Figure 5: Axial (top), coronal (middle), and sagittal (bottom) slices of a mouse at peak inhale (left) and exhale (right) using a 4D VOI reconstruction. The volume of interest contains a tumor and is outlined in dashed yellow lines.

Much of our discussion thus far has focused on small animals. However, as suggested in the discussion of small animal volume of interest based 4D CBCT, similar techniques could be used to improve clinical imaging. Clinical CT x-ray tubes do not have the energy range of the X-RAD which was utilized to improve small animal dual energy CT. Therefore, we will focus our clinical discussion on 4D CT imaging in radiation therapy and not dual energy CT. It is noted, however, that any improvements in low contrast detectability or quantitative accuracy seen in small animal dual

energy CT may be translatable to humans if a clinical CT imaging system with a larger energy range were to be developed.

As alluded to earlier, 4D imaging plays an important role in radiation therapy. The goal of radiation therapy is to deliver a high dose of radiation to the tumor in order to kill the cancer cells, while minimizing dose outside of the tumor to lessen damage to normal tissue. This goal becomes complicated when the tumor is moving, such as a lung tumor moving with respiratory motion. There are a number of strategies aimed at managing this motion, both during the simulation and planning stages of the treatment and during the treatment itself. One such strategy is to perform a 4D CT scan³⁶⁻³⁸ during simulation, where CT images of the patient in treatment position are obtained and used for treatment planning and dose calculation. Similar to what was described for mice, 4D CT allows the motion of the tumor to be visualized, which can assist in determining the appropriate motion management strategy during treatment delivery. For relatively small motion, a common motion management strategy is to use the 4D CT images to define a target area that includes the full path of the visible tumor (Internal Gross Tumor Volume or IGTV)^{39,40}.

Like 4D CBCT in mice, 4D CT can benefit from a data driven approach to obtaining the respiratory signal. The data used in data driven 4D CT (multiple reconstructed axial images at each bed and detector position) and 4D CBCT (single 2D projection image at each angle) are different, requiring different approaches, but the concept and benefits are similar. External respiratory surrogates are more commonly used in humans than they are in mice with many clinics already having such devices and being trained in their use. However, there is a benefit from using a respiratory signal that is closer to the actual internal motion, since external surrogates have been shown to have phase shifts or other inconsistencies with internal motion⁴¹⁻⁴³. A data driven approach may also have an impact on artifacts that are present in 4D CT. In CINE 4D CT, the couch is

stationary at one position for at least one respiratory cycle, then moves on to the next position. If there is a difference in the position of internal anatomy in a particular phase between adjacent couch positions, there will likely be a discontinuity at the transition between couch positions as shown in Figure 6. While these artifacts are primarily the result of irregular breathing, using a respiratory signal that is more closely tied to internal motion may reduce these artifacts. This possible reduction is an added benefit of using a data driven approach as it improves the ability to measure the tumor motion based on the depicted internal motion from the CT images.



Figure 6: Sagittal slice of 4D CT scan where artifacts at bed transition boundaries are evident (black arrows)

Since the introduction of 4D CT a number of different data driven approaches have been proposed^{37, 44-48}, and recently some of these concepts have been included in a commercial product^{44,}

⁴⁹. Independent testing of the final commercial product or directly testing its clinical applications has not been performed previously. To be used clinically, any systematic differences in target volumes between standard 4D CT techniques and data driven 4D CT should be noted and corrected if they lead to an underestimation of the IGTV. Our aim is to compare target volumes of this technique to standard 4D CT and to look for any improvements in artifacts that it provides.

The use of targets based on 4D CT assumes that the motion of the tumor remains the same over the course of the radiation treatments. However, there may be changes in the tumor motion from one treatment day to another, especially if the tumor shrinks in response to treatment⁵⁰. As cone-beam CT image guidance is available on most linacs now, 4D CBCT immediately prior to treatment can be used to monitor changes in respiratory motion and especially to detect any substantial deviations of the tumor motion trajectory from the planned target area. Ideally, these 4D CBCT images would also allow for 3D alignment to planning images without the need for a separate reconstruction.

4D CBCT has not been used extensively, however, in part due to the problem of streak artifacts when the scan time is only 1 to 2 mins. Streak artifacts, as demonstrated in Figure 7, are the result of large angular gaps between projections from one breathing cycle to the next in phase image reconstructions. The faster the gantry rotation and the slower the breathing, the more the gantry will rotate between the start of each breathing cycle and the worse the streak artifacts will be. Due to the rapid breathing of mice, these artifacts are not a major concern in mouse 4D CBCT, but do need to be addressed in human 4D CBCT. These streak artifacts not only make it more difficult to see the tumor and determine its motion, but also make it difficult to use the image for initial 3D alignment. One approach is to increase the scan time by slowing the gantry rotation speed, but as this increases dose and the time that the patient must remain motionless on the treatment

table, it is not always feasible. A number of iterative reconstruction techniques have been proposed to limit streak artifacts, but their reconstruction times are often too lengthy to be used during the time period of a radiation treatment. A volume of interest approach, such as the one discussed for mice, would allow iterative techniques to be used while keeping the added reconstruction time at a minimum. Additionally, as all projections are used outside the volume of interest and these projections are evenly spaced, the streak artifacts in this region are kept to a minimum allowing it to be used for initial 3D bony anatomy alignment. A volume of interest approach also has an important advantage that it allows for a quick visual assessment of whether the tumor remains within the target area if the registered target area is set to be the volume of interest.

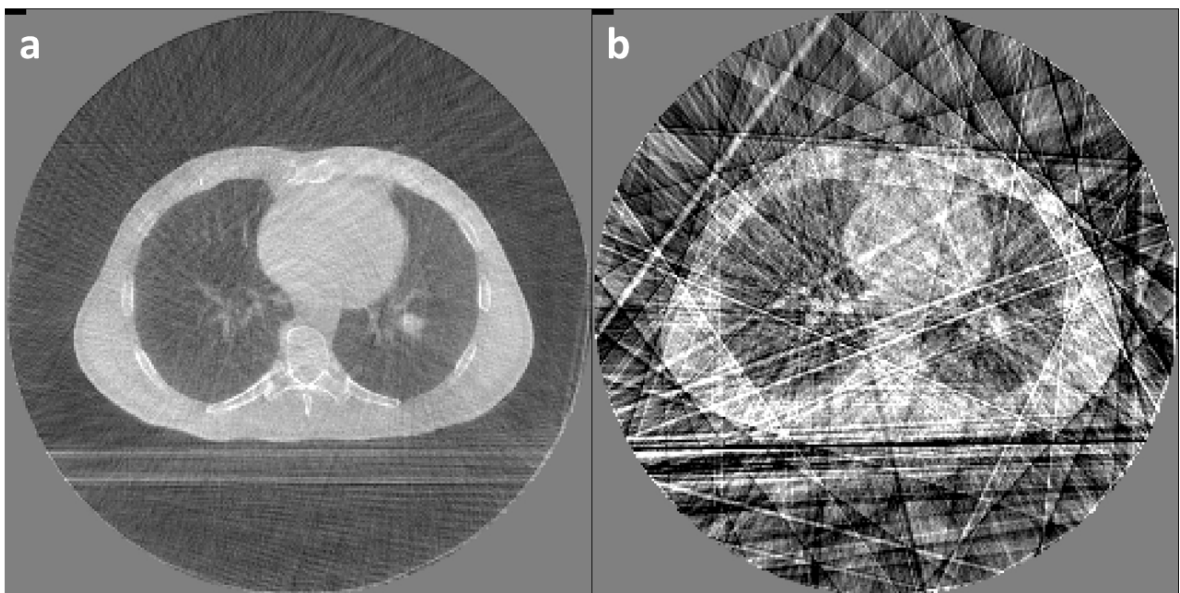


Figure 7: Comparison of 3D (a) and 4D phase (b) CBCT axial image. Prominent streak artifacts are present in the phase image due to under-sampling and uneven projection spacing.

Such an iterative volume of interest based approach was proposed by Moiz Ahmad and was part of his dissertation. However, most of the previous testing done of this reconstruction was with phantoms. Our work is to test this reconstruction in a larger number of patients to see whether the

tumor motion measurement, image quality, and reconstruction time benefits are realized in human subjects.

We have now provided background and motivation for the improvements to small animal and human CT imaging that we propose and/or test in this dissertation. The goal of the work can be summarized as addressing the following hypothesis:

Improvements can be made in image quality, quantitative accuracy, and/or workflow to small animal dual energy CT by increasing energy spectra separation and to human and small animal 4D CT imaging by using data driven techniques to obtain the respiratory signal and using a volume of interest based reconstruction.

The types of improvements made or tested for are summarized here:

For mice:

1. Improve contrast to noise ratio (image quality) and Iodine concentration accuracy and precision (quantitative accuracy) by increasing energy spectra separation in dual energy CBCT. (Specific Aim 1)
2. Reduce setup complexity (workflow improvement) and image blurring (image quality improvement) and improve projection sorting and tumor motion measurements (quantitative accuracy) in 4D CBCT by translating several human data driven 4D CBCT methods to mice. (Specific Aim 2)

For humans:

1. Test for improvements in artifact severity (image quality) and tumor target volume (quantitative accuracy) using data driven 4D CT. (Specific Aim 2)

2. Test for improvements in tumor motion measurements (quantitative accuracy), bony anatomy visualization (image quality), streak artifact severity (image quality), and reconstruction time (workflow) using an iterative volume of interest 4D CBCT reconstruction. (Specific Aim 3)

The specific aims to address these goals and their associated working hypotheses are listed below, along with the chapter numbers that will cover them.

Specific Aim 1 (Chapter 2): To determine the optimal imaging parameters for quantification of material density and low contrast detectability for contrast enhanced dual energy CT on the X-RAD system.

Working Hypothesis: The optimal energy pair for dual energy imaging on the X-RAD will have improved quantitative accuracy of more than 5% in iodine concentration error and 50% in contrast to noise ratio over the standard 80 and 140 kVp.

Specific Aim 2.1 (Chapter 3): To adapt several data driven 4D cone-beam CT methods designed for humans for mice and evaluate these methods for accuracy 4D projection sorting.

Working Hypothesis: The human data driven 4D CBCT techniques of Amsterdam Shroud, Fourier transform phase, and intensity can be translated to mice with a projection sorting error less than 5% of a breathing cycle and statistically lower projection sorting error than the previous center of mass data driven 4D CBCT method for mice.

Specific Aim 2.2 (Chapter 4): To compare a commercially available data driven 4D CT algorithm to existing standard methods in regards to severity of artifacts and internal gross tumor volume.

Working Hypothesis: Data driven 4D CT will result in a statistically significant reduction of artifacts and statistically equivalent target volumes compared to standard 4D CT.

Specific Aim 3 (Chapter 5): To compare, using a long-scan patient data set, the accuracy of tumor motion determination and bony anatomy image quality of an iterative volume of interest based reconstruction technique for 4D cone-beam CT to existing reconstructions including FDK and TV minimization and an FDK volume of interest based reconstruction.

Working Hypothesis: Iterative volume of interest 4D CBCT will improve tumor motion measurements compared to standard FDK and FDK VOI, and will improve computation time with at least as accurate tumor motion measurements as TV minimization.

Chapter 2: Optimization of Dual Energy CT for small animal contrast enhanced imaging

2.1 Introduction

DECT could benefit contrast enhanced small animal imaging since Iodine material images could improve visualization of low concentrations of Iodine allowing for lower injection volumes, and provide a means of quantifying Iodine concentration for targeted Iodine imaging. Therefore, the aim of this chapter is to determine DECT imaging parameters that provide the most accurate iodine concentrations and highest contrast to noise ratios (CNR).

Low contrast detectability and precision in Iodine concentration measurements both improve with reduced material image noise. In early dual energy CT studies, Rutherford et al showed that assuming the same noise levels in the input low and high energy images, precision in the measurement of effective atomic number improved with increased energy separation²⁰. Kelcz et al derived that noise in material images is inversely related to the difference in the ratio of the attenuation coefficients (at energy 1 to energy 2) between the different materials.¹⁸ From this relationship, we expect that increasing the energy spectra would decrease noise since the difference in attenuation properties of the different materials are more pronounced with larger separation. This relationship was confirmed in Kelcz's paper, with increased high energy kVp and decreased low energy kVp yielding lower noise. With decreased noise comes improved low contrast detectability and precision in quantitative measurements. Other studies have verified this behavior for a number of different applications. Primak et al¹⁹ looked to improve dual energy by adding filtration to the high energy x-ray tube to increase the spectra separation. They expressed the relationship derived by Kelcz in terms of the dual energy ratio

(the ratio of the slopes of CT versus density curves for the low and high scans) and showed that material image noise was inversely proportional to the difference in dual energy ratios of the two materials. These studies have primarily relied on the energy range of a standard x-ray tube, or lower energies in the case of small animals. However, some work has done exploring dual energy with megavoltage energies for the high energy scans, showing improvements in the metrics measured over kilovoltage only dual energy. Yang et al compared kV only, kV and MV, and MV only dual energy reconstructions for the calculation of proton stopping power ratios (SPR) for improved proton therapy dose calculation. They found that kV-MV dual energy CT showed improvement in the accuracy of SPRs in realistic CT noise and beam hardening conditions compared to either kV-kV or MV-MV dual energy CT.

Due to a shared x-ray tube for imaging and radiation treatments, the small animal image guided radiation therapy system X-RAD 225Cx (Precision X-Ray, Inc. North Branford, CT) has an x-ray tube energy range of 20-225 kVp. The aim of this study is to take advantage of this wide range to study dual energy CT over a larger kilovoltage energy range, to our knowledge, than has been previously studied. Simulations and phantom studies are performed to determine the ideal energy combinations to determine the optimal energy pairs for iodinated contrast agent imaging of mice in terms of iodine concentration accuracy and CNR.

2.2 Methods

2.2.1 Simulations

Simulations were used to test a large number of high and low energy combinations. A ray-tracing based simulation known as ImaSim was used. Rays are created connecting the source to each detector element and the attenuation of x-rays of energies determined by the source spectrum is determined by their path through the object. The source spectrum model is based on the work of Poludniowski et al⁵¹⁻⁵³ who utilizes probability functions of electron penetration determined through

Monte Carlo as well as physical modeling of bremsstrahlung x-ray production and filtration. This model has been shown to be at least as accurate as semiempirical and empirical methods⁵³ and allows for modeling of energies above 150 keV, making it a good candidate for this study. The user inputs the tube potential (0-300 kVp), anode angle, and filtration (W, Cu, Al, Sn, Ta, Be, air and water) and the software calculates the energy spectrum, HVLs, air kerma, and mean energy. Filtration included 0.8 mm Be, 3 mm Al filter, air gap of 300 mm, and half the thickness of the phantom in water (25 mm). Low energy spectra used in these simulations included every 10 kVp from 50 to 80 kVp. High energy spectra included every 20 kVp from 100 to 220 kVp. Every combination of low and high energy spectra was simulated. The digital phantom consisted of eight 1 cm diameter cylindrical rods embedded in a 5 cm diameter water phantom. The rods had iodine concentrations of 50, 20, 10, 5, 3, 2, 1, and 0.5 mg/mL. The detector responses included in the simulation software were determined using Monte Carlo modeling. A 20x20 cm Cesium-iodide (CsI) detector with 256x256 pixels was used in the simulation as it closest to the detector used on the XRAD. However, it should be noted that differences exist in the thickness of CsI and materials covering the detector that can have some influence on the resulting measurements. 360 evenly spaced projections were taken of the phantom placed at isocenter with 30 cm source to isocenter and 60 cm source to detector distances. Noise was included in the form of Gaussian noise added retrospectively to the projection images based on the input mAs. The mAs for each scan was selected such that the total air kerma was 10 cGy, divided between the scans such that 3 cGy went to the low energy scan and 7 cGy went to the high energy scan. This dose allocation was based on previous dual energy optimization studies that concluded roughly 30% of the dose should come from the low energy scan to reduce the noise propagation from the high energy scan^{54, 55}. This dose allocation translates to roughly a 3/2 ratio of mAs_{low}/mAs_{high} at clinical energies, which is approximately the ratio used in clinical scanners.

2.2.2 Simulation calibration

To determine the calibration equations needed to go from low and high energy attenuation to water and iodine density weighted thickness, cylinders of varying thicknesses of water and iodine were scanned using the same scan geometry and detector, but only one projection. Water thicknesses were 0, 0.6, 1.5, 2.4 and 3 cm and iodine thicknesses were 0, 0.006, 0.015, 0.024, and 0.030 cm. All combinations of these thicknesses were scanned by placing cylinders on top of each other and scanning along the vertical direction of the cylinders. No noise was added to the projection images for the calibration.

The calibration equations relating high and low projection images to projection images of each material are as follows:

$$I = \alpha_0 + \alpha_1 H + \alpha_2 L + \alpha_3 H^2 + \alpha_4 HL + \alpha_5 L^2 + \alpha_6 H^3 + \alpha_7 L^3 \quad \text{Equation 1}$$

$$W = \beta_0 + \beta_1 H + \beta_2 L + \beta_3 H^2 + \beta_4 HL + \beta_5 L^2 + \beta_6 H^3 + \beta_7 L^3 \quad \text{Equation 2}$$

where H and L are the high and low energy projection image values and I and W are the iodine and water projection image values. The values of the coefficients (α 's and β 's) of these cubic equations are the end result of the calibration process. Non-linear least squares fitting (the Levenberg-Marquardt algorithm of MATLAB's `lsqnonlin` function) using high and low energy data and known iodine and water thicknesses were used to determine the coefficients. These equations were then used to obtain material density weighted thickness projections.

2.2.3 Image reconstruction and analysis

Images were reconstructed using Feldkamp-Davis-Kress⁵⁶ (FDK) reconstructions with in-house software. After reconstruction, voxel values in the iodine images should be the same as the iodine density of the corresponding insert within the phantom. ROIs were placed at the center of each insert and in the water background region in the center axial image and the average standard deviation and

voxel value were calculated in each. From these values the contrast to noise (CNR) and percent error in iodine density were calculated.

2.2.4 Justification for image based material decomposition on the X-RAD

While projection based material decomposition is more accurate than image based material decomposition⁵⁷, it relies on the assumption that each pair of high and low energy projections is acquired from the same angle and is of the same object. With a moving object, the second part of this assumption does not hold in general for sequential scanning. For example, a mouse may be in peak exhale during the 90 degree projection of the low energy scan and in peak inhale during the 90 degree projection of the high energy scan. Since projection based material decomposition relies on the difference between high and low projection images at each angle, the difference in position of the diaphragm in this case is especially problematic. If the scanner does not acquire images at the same angles for repeated scans, the first part of the assumption would not hold either. Initial testing revealed angle differences of up to 50 degrees for the same projection number in repeated scans (15 fps, 3 rpm, no binning). To determine a more suitable dual energy imaging protocol, imaging parameters that could potentially have an impact on angle repetition accuracy were varied. Frame rate (5 fps and 15 fps), pixel binning (1x1 binning and 2x2 binning) and rotation rate (0.5 rpm and 1 rpm) were independently varied to create 5 protocols and each protocol was scanned 4 times in a row. The average angular difference between matching projections from different scans was calculated and are shown in Figure 8. Within the parameter ranges tested, statistical differences were not observed.

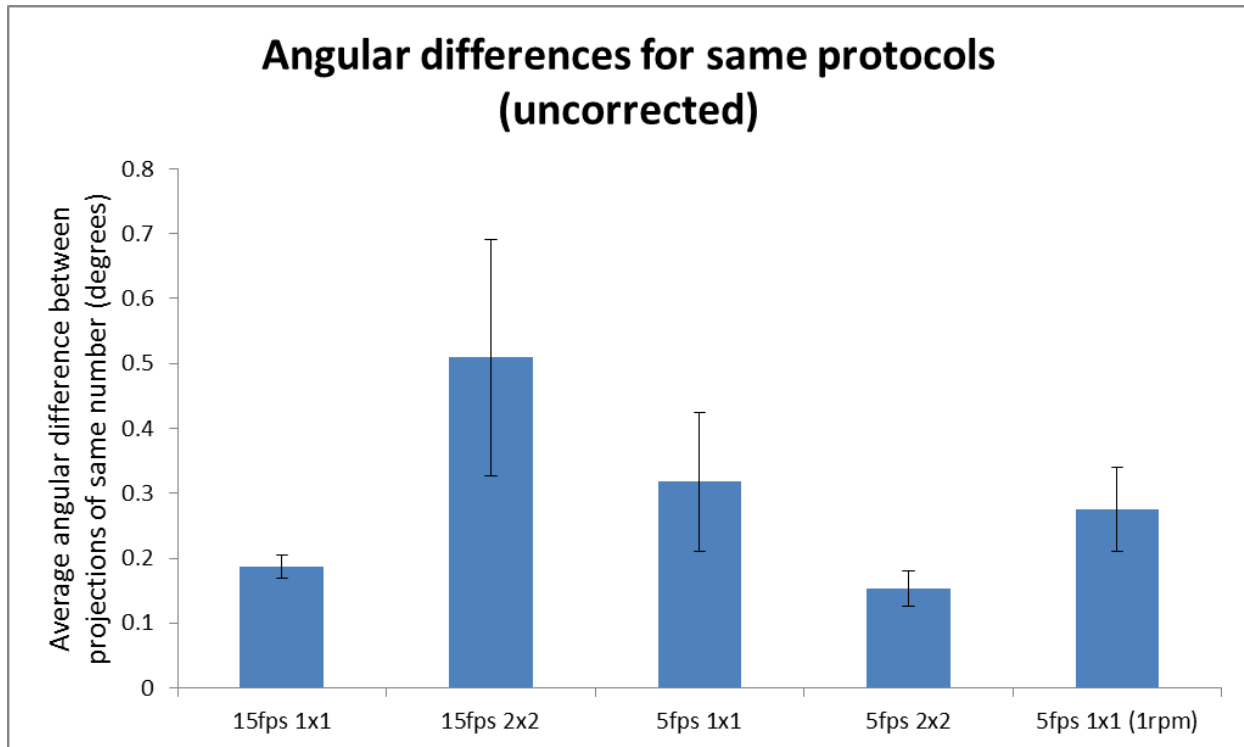


Figure 8: Average difference in angle for matching projections in repeated scan for varying frame rate, pixel binning and rotation rate.

To determine how much of a role differences in start location had on the average angular difference, projection angles were retrospectively shifted such that the angle of the first projection was the same in all repeated scans. Projection angle differences were again compared and shown in Figure 9. Once starting angle differences were removed, lower frame rates and less binning were shown to have less angular differences.

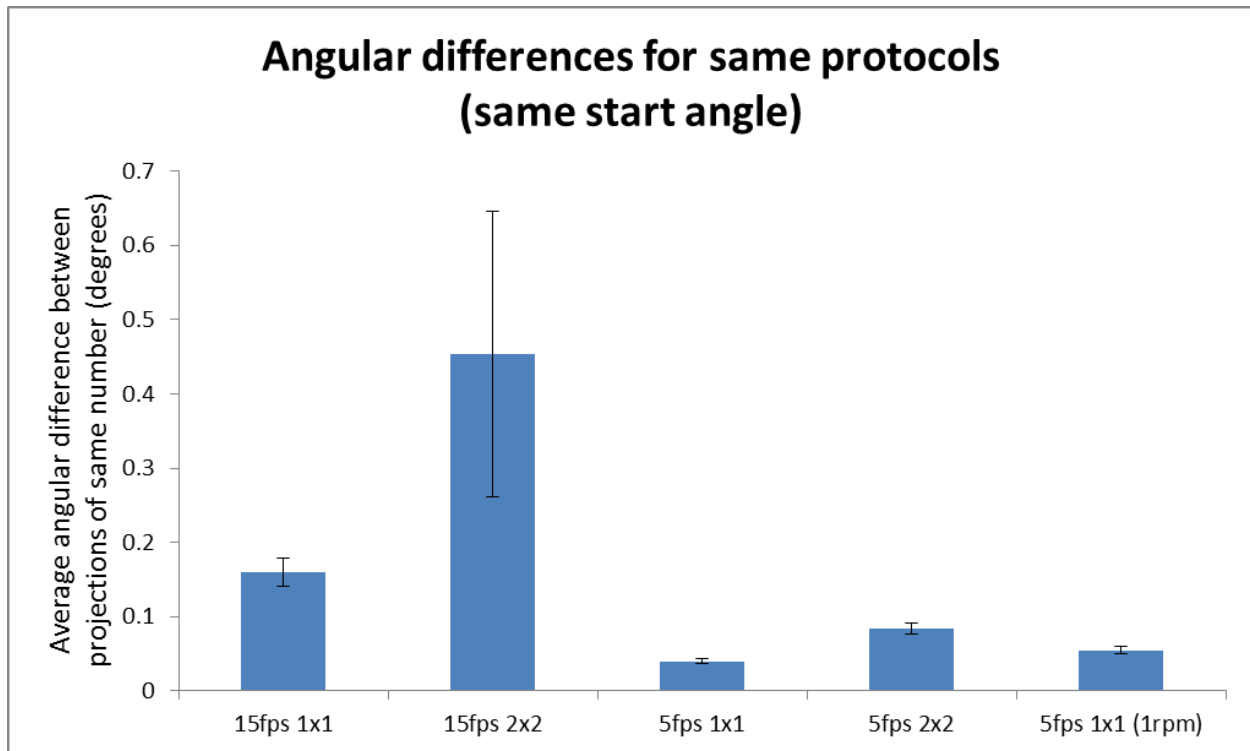


Figure 9: Average difference in angle for matching projections in repeated scan for varying frame rate, pixel binning and rotation rate once the starting angles were matched and other projection angles shifted accordingly.

While these results are informative, and suggest the differences are dominated by the starting angle, the angle the projection was actually scanned at cannot be retrospectively changed. One solution to these differences is to interpolate projections to obtain simulated projections at desired angles that can be matched between sequential scans. However, this interpolation comes at the cost of some spatial resolution.

As a result of the problem of motion during sequential scanning and differences in projection angles of repeated scans, an image based material decomposition was chosen for this project.

Additionally, an image based approach is more easily translated to other small animal CT scanners.

2.2.5 Image based calibration for Dual Energy CBCT on the X-RAD

Image based calibrations were conducted using a cylindrical solid water phantom with two sets of 3 Iodine mixtures (water, 5 mgI/mL and 25 mgI/mL) in 1mm syringes inserted into it as shown in Figure 10. Mixtures were made by diluting a 350 mgI/mL Omnipaque injection (GE Healthcare, Waukesha, WI). Calibrations were originally tested with two low energy (60kVp and 80kVp) and two high energy (140kVp and 200kVp) scans. For each energy, up to three mA were selected to test the effect of mA on calibration accuracy. The highest mA used was just under the limit of detector saturation with no object in the field, medium mA was half of the highest, and low mA was a quarter of the highest. For the high energies, low (and in the case of 200kVp, medium) mA were not achievable due to insufficient stability of the output. The energies and mA used are included in Table 1. Calibration scans were performed with a frame rate of 15 fps, rotation rate of 1 rpm, no pixel binning and medium detector gain. HU values of the measured concentrations were determined from averaging voxels across the middle 20 slices within ROIs placed at the center of the inserts and across the two different inserts for each iodine concentration. These measured values and known true concentrations were used to determine the coefficients of the linear relationship between material concentrations and high and low energy HU values. As with the simulations coefficients were determined through a non-linear least squares fit to the following linear equations.

$$I = \alpha_0 + \alpha_1 H + \alpha_2 L \quad \text{Equation 3}$$

$$W = \beta_0 + \beta_1 H + \beta_2 L \quad \text{Equation 4}$$

Where H and L are the high and low energy image values, I and W are the Iodine and water image values, and α 's and β 's are the coefficients. Linear equations were used here as these are commonly used for image based calibration when using beam hardening corrected images⁵⁷.

Table 1: mA for calibration scans

	50	60	70	80	100	120	140	160	180	200	220
	kVp	kVp	kVp	kVp	kVp	kVp	kVp	kVp	kVp	kVp	kVp
High	9.0	5.0	3.0	2.0	1.0	0.6	0.5	0.4	0.3	0.3	0.3
Medium	4.5	2.5	1.5	1.0	0.5	0.3	0.3	0.3	0.2	----	----
Low	2.3	1.3	0.8	0.5	0.3	0.2	----	----	----	----	----

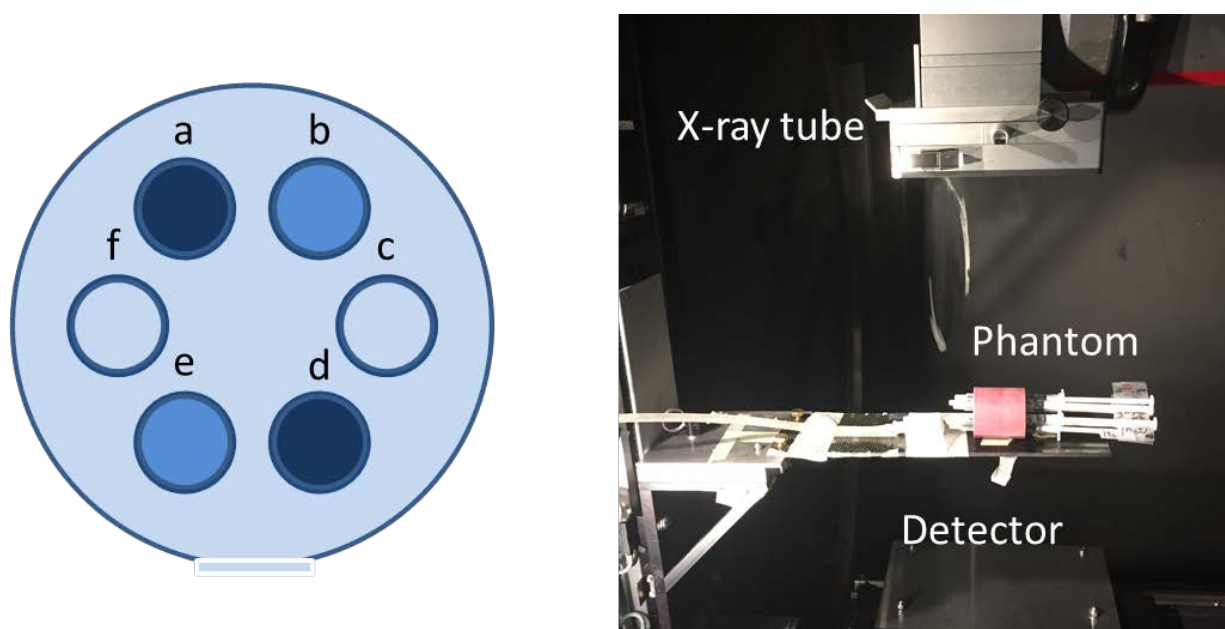


Figure 10: Schematic of solid water calibration phantom with water 25 mg I/mL (a, d), 5 mg I/mL (b, e), and water (c, f) inserts is shown on the left. A photo of the imaging and calibration setup is shown at right including the x-ray tube and detector of the X-RAD and the phantom.

To test the calibration procedure 5 new iodine concentrations (1, 3, 10, 20, and 30 mgI/mL) were inserted into the same phantom along with water and the phantom was scanned with the same kVp and mA combinations used in calibrations. The percent error in iodine concentration was determined for each test insert and energy and mA combination. Additionally, to test the calibration procedure's accuracy when applied to an object of a different size and geometry to the calibration

phantom, three Gammex 472 DECT phantom inserts (Sun Nuclear) were scanned with the same kVp and mA combinations. The inserts were approximately 3 cm in diameter and included solid water, 5 mgI/ml, and 20 mgI/ml.

The calibration procedure was repeated twice for a total of 3 calibrations to test the repeatability of the calibration procedure. One set of the syringes was kept the same throughout the different calibrations and used to compare the accuracy of the repeated calibrations using the test phantom and coefficients derived from only these syringes. New mixtures of the same concentrations were created for each new calibration and used to compare HU differences and differences in calibration results due to variations in making the mixtures.

2.2.6 Determining optimal energy pairs

To determine the optimal energy pair for contrast enhanced DECT on the X-RAD, dual energy CT scans and calibrations were done for low energies of 50 – 80 kVp in increments of 10 kVp and high energies of 100 – 220 kVp in increments of 20 kVp. The calibration scans were performed once for each energy tested in the same manner as was used during the calibration testing and with the same method of determining mA. The mA used in the calibrations for each kVp is shown in Table 1. Next scans at each energy tested were performed of the same phantom used in calibration with water and 1, 3, 5, 20, and 30 mgI/mL inserts. As with the calibrations, low, medium and high mA were scanned at each energy when possible. In this case, the dose for each low energy scan and high energy scan was matched as much as possible for each category. To determine the appropriate mA for dose matching, the manufacturer specified doses for various imaging scans (30 – 100 kVp) were used to determine a linear kVp to dose relationship for equal mA and extrapolated to higher energies. The mA to dose relationship at each kVp was assumed to be linear, so the mA for a specified dose at each kVp could be determined.

The relationship between kVp and dose is shown in Figure 11 and the mA and doses for each scan are included in Table 2. Iodine and water images were obtained for each energy pair at each combination of high and low energy dose. The percent error in Iodine concentration was determined for the 20 and 30 mgI/mL inserts, and the contrast to noise ratio was determined for the 5, 3, and 1 mgI/mL inserts (with background and noise determined in an ROI placed in the periphery of the solid water portion of the phantom).

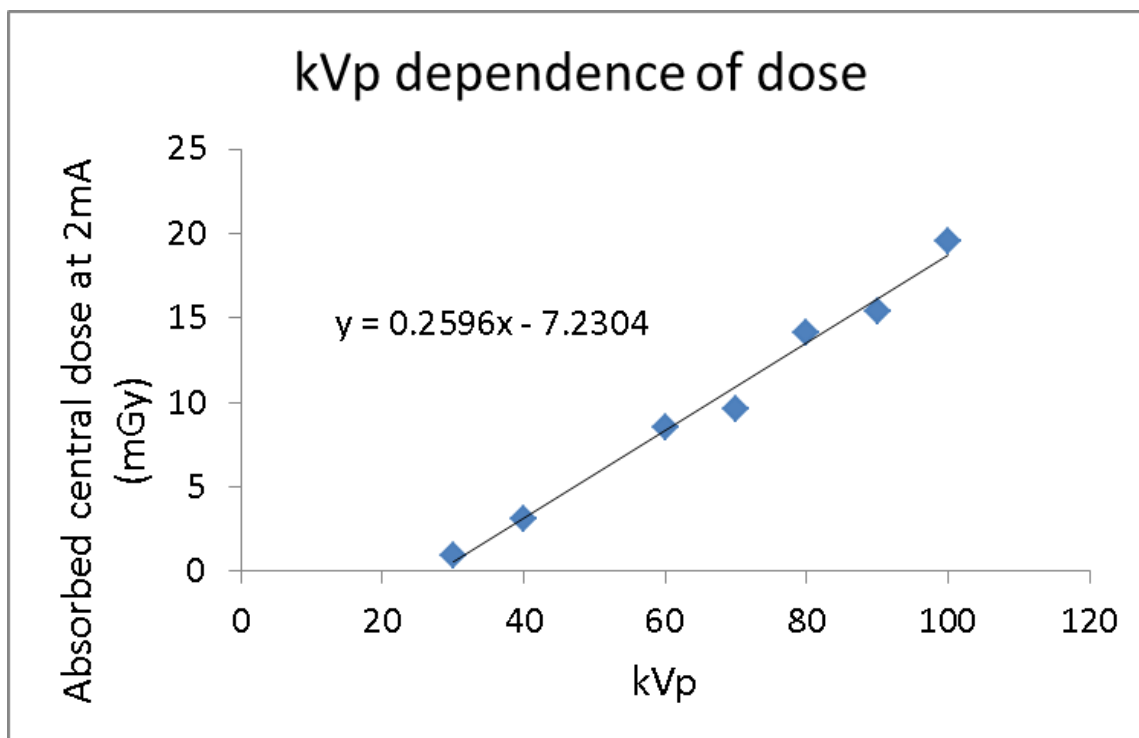


Figure 11: The energy dependence of dose with data points from manufacturer supplied data scaled to the same mA. The linear fit to this data was used to dose match each of the high and each of the low energy scans.

Table 2: The mA for each scan used for DECT at listed high (H), medium (M), and low (L) doses.

mA for low energy scans of energy:					mA for high energy scans of energy:							
Dose (mGy)	50 kVp	60 kVp	70 kVp	80 kVp	Dose (mGy)	100 kVp	120 kVp	140 kVp	160 kVp	180 kVp	200 kVp	220 kVp
14 (H)	4.9	3.4	2.6	2.1	6.5(H)	0.7	0.5	0.4	0.4	0.3	0.3	0.3
7 (M)	2.4	1.7	1.3	1.0	4 (M)	0.4	0.3	0.3	0.2	0.2	----	----
3 (L)	1.0	0.7	0.5	0.4	2 (L)	0.2	0.2	----	----	----	----	----

2.3 Results

2.3.1 Simulations

The percent error in iodine density accuracy in the 10 and 20 mgI/mL inserts for each energy combination tested is shown in Figure 12. Each data point represents a different energy combination, with the kVp of the high energy scan is shown along the x-axis and the kVp of the low energy scan shown as different curves. Some decrease in error is observed with increasing energy, especially going from 100 kVp to 140 kVp, with some leveling off. A more dramatic decrease is observed in the 50 kVp, although the error is higher overall for this low energy. The low energy of 60 kVp also had somewhat larger errors than 70 and 80 kVp. The likely reason for this increased error despite the increased spectra separation is the proximity of the mean energy of these low energy spectra to iodine's k-edge (33 keV), which is not modeled in the calibration process. While the peak in error at 120 kVp for the 50 kVp curve is not fully understood, it is likely a byproduct of the detector response not being entirely linear with energy. Note that while the detector used in the simulation is made of the same material as the detector in the X-RAD, it is not necessarily the same thickness (X-RAD: unknown thickness, simulation: 3cm of 0.21 g/cm² CsI) or include the same surface materials (X-RAD: 0.5mm graphite/molybdenum,

unknown thickness of Al, simulation: 50 μ m Al) which may have some impact on the shape of these curves.

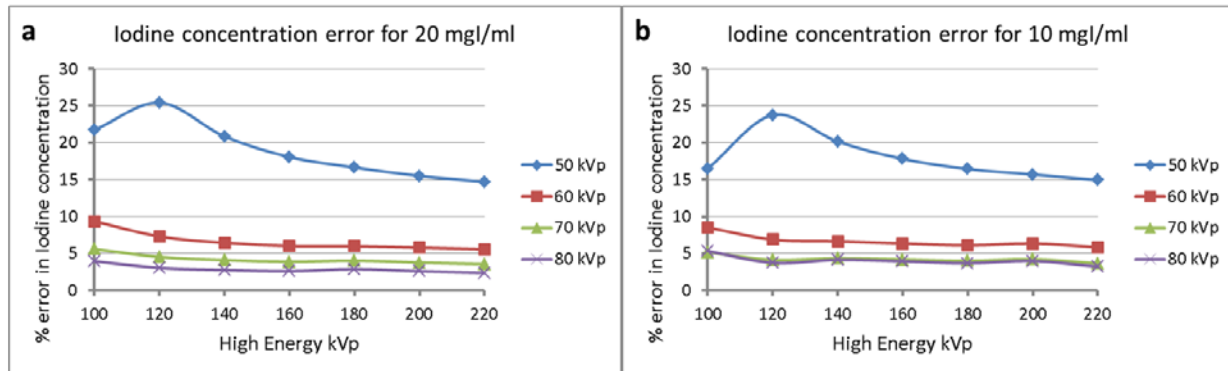


Figure 12: Percent difference in iodine concentration between known and measured concentration for the 20 mgI/ml (a) and 10 mgI/ml (b) inserts in the ray-tracing based simulations. Changes in the high energy of the energy pair are shown along the x-axis and changes in low energy are shown as different curves.

The contrast to noise ratio (CNR) for each energy pair is similarly shown in Figure 13 for the 5 mgI/mL and 3mgI/mL inserts. In the case of CNR, a clear trend of increasing CNR with increasing high energy and decreasing low energy (increased energy separation) is seen, including an almost 4-fold increase from the closest energy pair (80kVp/100kVp) to the most separated energy pair (50kVp/220kVp) for the 5mgI/mL insert. Simulation generated images displaying this relationship between low and high kVp and CNR is shown in Figure 14.

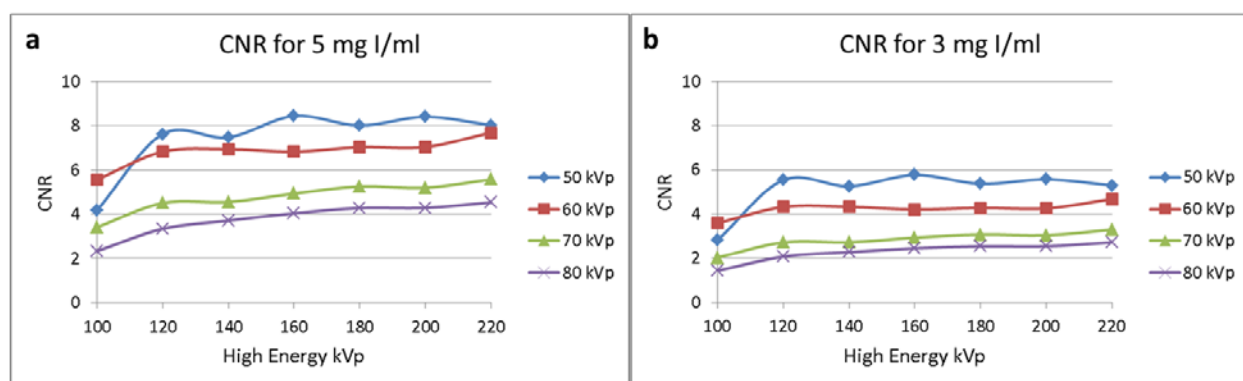


Figure 13: Contrast to noise ratio for 25 mgI/ml (a) and 5 mgI/ml (b) inserts compared to background in the ray-tracing based simulations. Changes in the high energy of the energy pair are shown along the x-axis and changes in low energy are shown as different curves.

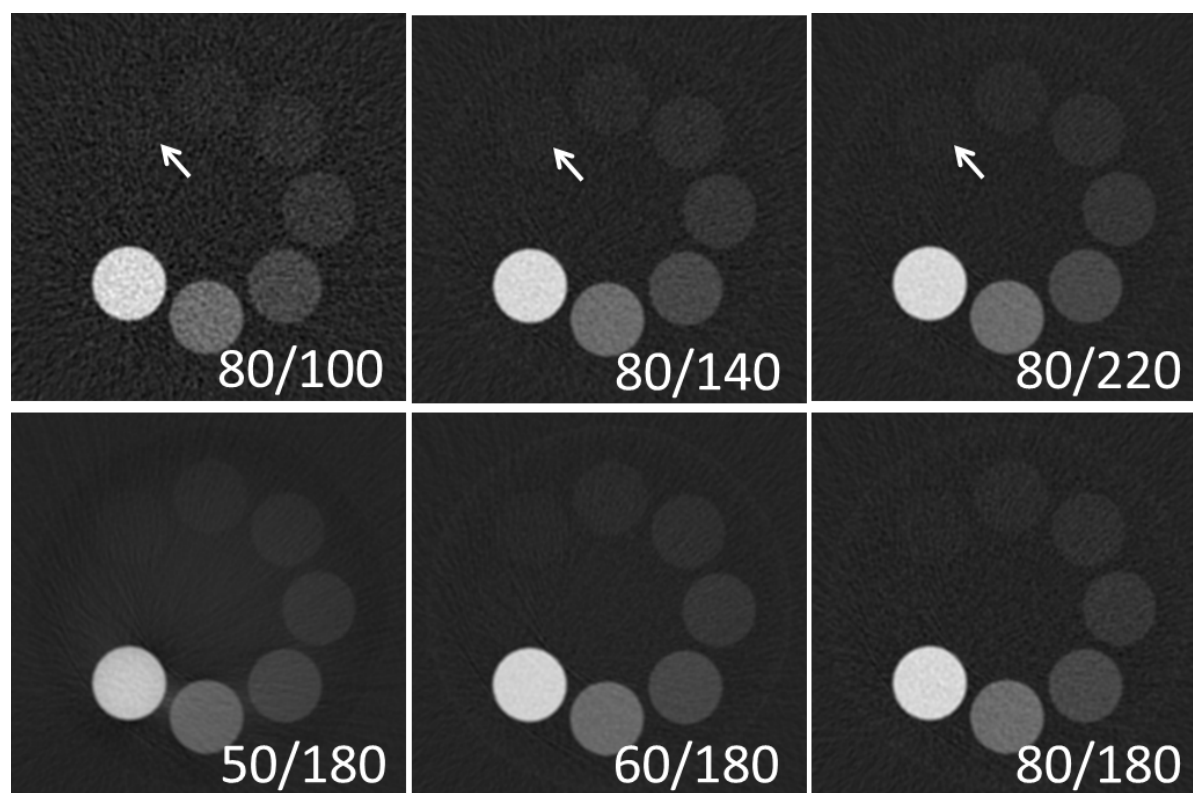


Figure 14: Simulation generated Iodine images demonstrating the effect of increasing the energy of the high energy scan (top row increasing from left to right) and increasing the energy of the low energy scan (bottom row increasing from left to right). As seen in these images, particularly for the 1 mg I/ml insert (white arrow), contrast to noise increases with increasing high energy kVp and decreasing low energy kVp.

2.3.2 Physical calibrations

Iodine error quantified as the percent difference between measured and known Iodine concentrations are shown in Table 3 and Table 4 for the first calibration attempt. Percent differences were generally under 10% for Iodine concentrations 10 mg/ml or greater. Similar percent errors are seen in clinical dual energy CT scanners. Larger percent errors are observed for lower concentrations where small absolute errors in concentration result in large percent errors. No clear relationship between mA and Iodine error was seen in this or the other calibration days' data, suggesting it does not have a strong impact on the calibration accuracy (likely due to the amount of voxel averaging that was

done within the inserts to minimize the influence of noise). Errors were similar with the Gammex inserts compared with the liquid Iodine inserts in the solid water phantom, suggesting the calibration accuracy is relatively insensitive to the imaged object's size, geometry, or composition (solid inserts versus liquid Iodine mixtures).

Table 3: Iodine errors for day 1 calibration coefficients for low energy of 60 kVp applied to the same phantom with different Iodine concentrations and to the Gammex phantom inserts. High (H), medium (M), and low (L) mA are as specified in Table 2.

actual Iodine concentration (mg/ml)	percent difference from actual								
	60H			60M			60L		
	140H	140M	200H	140H	140M	200H	140H	140M	200H
<i>small animal Iodine phantom</i>									
30	8.5	3.5	5.8	4.3	0.9	2.2	8.1	2.8	5.3
20	7.9	1.1	4.1	4.2	5.1	0.9	6.1	3.2	2.5
10	10.0	3.3	3.8	5.1	18.8	8.9	5.2	8.6	0.3
3	34.9	17.6	5.2	1.4	19.1	25.8	22.1	4.2	6.4
1	19.0	1.2	37.4	34.7	52.8	6.4	27.9	9.3	45.4
averaged	16.0	5.3	11.3	9.9	19.3	8.8	13.9	5.6	12.0
10-30mg/ml concentrations	8.8	2.6	4.6	4.5	8.3	4.0	6.5	4.8	2.7
<i>Gammex inserts phantom</i>									
20	2.8	1.8	6.1	3.1	2.1	6.5	3.0	2.0	6.3
5	5.4	3.3	12.5	7.3	5.1	14.3	5.3	3.2	12.7
averaged	4.1	2.6	9.3	5.2	3.6	10.4	4.2	2.6	9.5

Table 4: Iodine errors for day 1 calibration coefficients for low energy of 80 kVp applied to the same phantom with different Iodine concentrations and to the Gammex phantom inserts. High (H), medium (M), and low (L) mA are as specified in Table 2.

actual iodine concentration (mg/ml)	percent difference from actual								
	80 H			80M			80L		
	140H	140M	200H	140H	140M	200H	140H	140M	200H
<i>small animal iodine phantom</i>									
30	10.8	2.8	6.3	12.5	4.0	7.4	6.0	2.5	2.5
20	10.8	3.4	4.7	8.8	6.1	2.9	3.9	11.3	0.9
10	11.6	9.5	2.3	12.2	10.0	2.4	3.1	19.4	4.6
3	33.7	6.3	9.0	32.9	4.1	11.3	16.5	12.6	24.1
1	48.0	19.3	67.6	4.7	34.1	29.0	1.2	31.2	32.1
averaged	23.0	8.2	18.0	14.2	11.6	10.6	6.1	15.4	12.8
10-30mg/ml concentrations	11.1	5.2	4.4	11.2	6.7	4.2	4.3	11.1	2.6
<i>Gammex inserts phantom</i>									
20	4.4	2.8	8.7	6.5	4.8	10.5	6.2	4.5	10.3
5	6.1	2.7	16.2	9.6	6.1	19.2	10.2	6.6	19.8
averaged	5.2	2.8	12.5	8.0	5.5	14.9	8.2	5.6	15.1

To compare repeated calibrations, Iodine errors for each day were averaged across all energies and mA's and are displayed in Table 5. For the first day of calibration, where inserts of the same concentration were drawn from the same mixture, results using both sets of inserts and a single set of inserts are included. For the other two calibration days, where one of the insert sets was the same as day one ("old") and the second set was from of new mixture ("new") of nominally the same concentration, results for each of these insert sets were included. The single set from the first day and the old sets from subsequent calibrations were compared to determine the variation in Iodine concentration error from repeating the calibration procedure with an identical phantom. The single set from the first day and the new sets from subsequent calibrations were compared to also include differences rising from the mixture process in the variations. Standard deviations in Iodine error for each Iodine concentration are included in Table 6.

Table 5: Averaged percent difference in Iodine error for each calibration day, separated by use of both or one identical concentration calibration sets for the first day and old (same mixture as first day) or new mixtures for subsequent days.

Iodine concentrations (mg/ml)	day 1 (both)	day 1 (single)	day 2 (old)	day 2 (new)	day 3 (old)	day 3 (new)
<i>small animal Iodine phantom</i>						
30	5.3	5.4	4.8	3.7	6.8	3.7
20	4.9	5.2	4.2	4.4	4.3	3.3
10	7.7	8.0	7.2	8.1	6.4	7.1
3	16.0	16.8	20.7	18.8	17.7	17.0
1	27.8	29.4	24.7	29.0	37.9	39.9
averaged	12.3	12.9	12.3	12.8	14.6	14.2
10-30mg/ml concentrations	6.0	6.2	5.4	5.4	5.8	4.7
<i>Gammex inserts phantom</i>						
20	5.1	5.1	4.7	3.5	7.1	4.4
5	9.2	9.7	10.8	6.2	12.9	11.6
averaged	7.2	7.4	7.7	4.8	10.0	8.0

Table 6: Averaged standard deviations of Iodine error for 3 repetitions of the calibration using the same mixture and 3 repetitions using different mixtures (of nominally the same concentration).

actual Iodine concentration (mg/ml)	average standard deviations (% Iodine error)	
	same mixture	different mixtures
<i>small animal Iodine phantom</i>		
30	1.7	1.8
20	1.8	1.7
10	2.6	2.7
3	8.0	8.8
1	20.7	17.0
averaged	5.4	4.6
10-30mg/ml concentrations	1.4	1.4
<i>Gammex inserts phantom</i>		
20	2.0	1.6
5	5.4	4.2
averaged	3.6	2.8

2.3.3 Optimal energy pairs

The percent error in Iodine concentration for the 20 and 30 mgI/mL inserts are shown Figure 15 and the CNR for the 5 and 3 mgI/mL inserts are shown in Figure 16. Both these figures show graphs for the highest dose in both the low and high energy images, but similar trends were observed in other dose allocations. As with the simulation graphs, variations in the high energy kVp are shown along the x-axis and variations in low energy are shown as different curves. The Iodine error graphs include error bars indicating the standard deviation expected under ideal conditions (from the “same mixture” column of Table 6). The Iodine error graphs show little variation in the percent error with changing energy, especially for low energy. The non-linear variations in energy for changing high energy appear to be influenced by other factors such as image noise or variations arising from the calibration procedure (Table 6). The error bars in Figure 15 are on the order of the variations observed, suggesting that variation from the calibration is responsible for much of the non-linear behavior observed. Noise levels (standard deviation in a centrally placed ROI) for each energy scan are shown in Figure 17. While dose matching was performed to minimize these differences, mA on the X-RAD could only be specified to one decimal point, which required rounding. At the low mA of the high energy scans, this rounding had a noticeable effect on the noise of the images (for example the mA for the 140 and 180 energies was rounded down, leading to an actual dose that was lower than specified). The calculated doses once the mA is rounded are shown in Figure 17 for the highest dose level for each kVp (assumed doses of 14mGy and 6.5mGy for low and high kVp, respectively).

The dependence of the precision in Iodine concentration measurements on kVp pair is also shown in Figure 15. To obtain a metric for precision, the percent Iodine error was calculated for each axial slice, and the standard deviation of these values was determined. Unlike the error itself, the precision in the Iodine measurements showed some improvement with increasing high energy kVp (especially for low energy of 80 kVp) and to a lesser extent with decreasing low energy kVp. A 42% and

44% (30 and 20 mg I/mL inserts, respectively) reduction in the between slice standard deviation of iodine error was observed between the most (50/220 kVp) and least (80/100 kVp) separated energy pair.

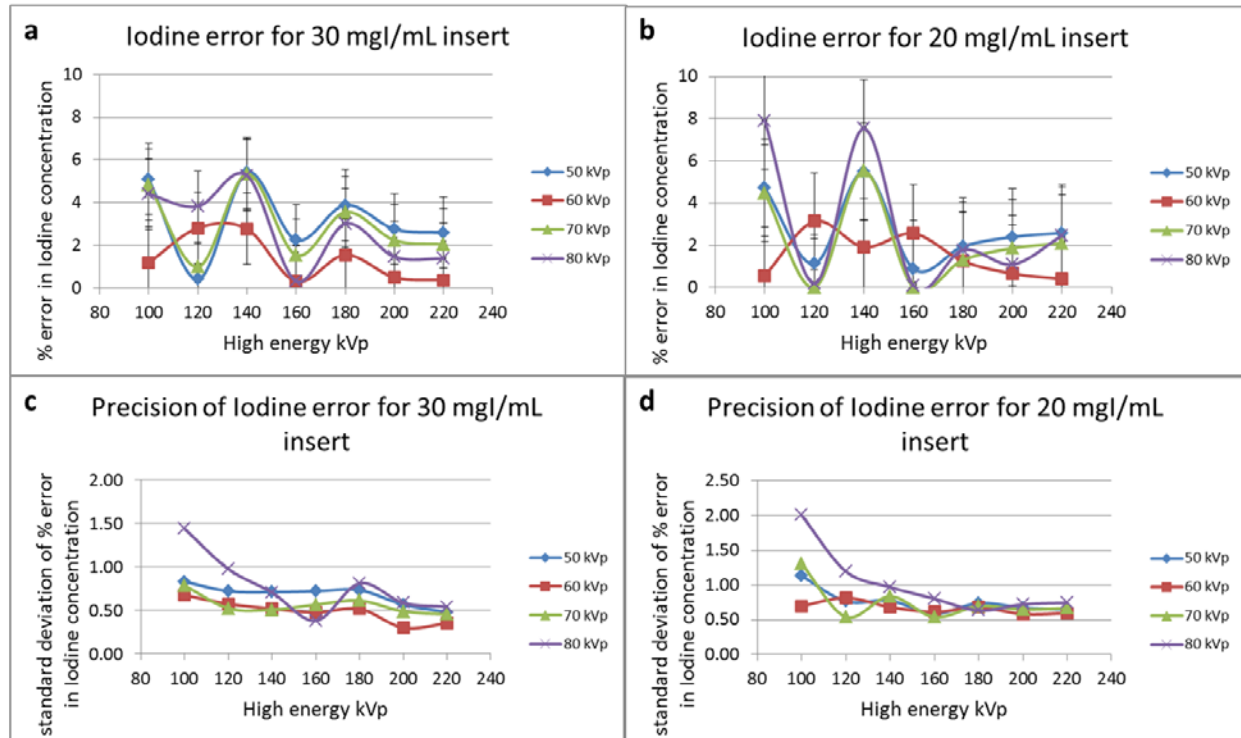


Figure 15: Percent difference in iodine concentration between known and measured concentration for the 30 mgI/ml (a) and 20 mgI/ml (b) inserts of the iodine phantom scanned on the X-RAD. Changes in the high energy of the energy pair are shown along the x-axis and changes in low energy are shown as different curves.

Like in the simulations, the CNR graphs (Figure 16) reveal a noticeable increase in CNR with increasing high energy. Some improvement is also seen with decreasing the low energy (increasing the separation) with the exception of 50 kVp. The lower performance of 50 kVp is likely related to the higher noise in the low energy image (see Figure 17). The difference in CNR between the most (50/220 kVp) and least (80/100 kVp) separated energy pairs is a factor of 2.7 for the 5 mg/ml insert and 2.5 for the 3 mg/ml insert. Images demonstrating the described behavior of CNR with changing low and high energy kVp is shown in Figure 18.

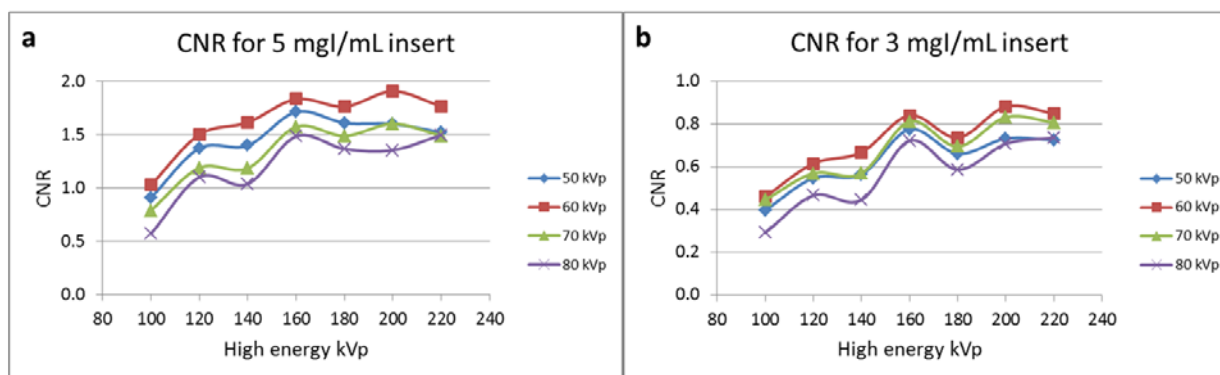


Figure 16: Contrast to noise ratio for 5 mgI/ml (a) and 3 mgI/ml (b) inserts compared to background the iodine phantom scanned on the X-RAD. Changes in the high energy of the energy pair are shown along the x-axis and changes in low energy are shown as different curves.

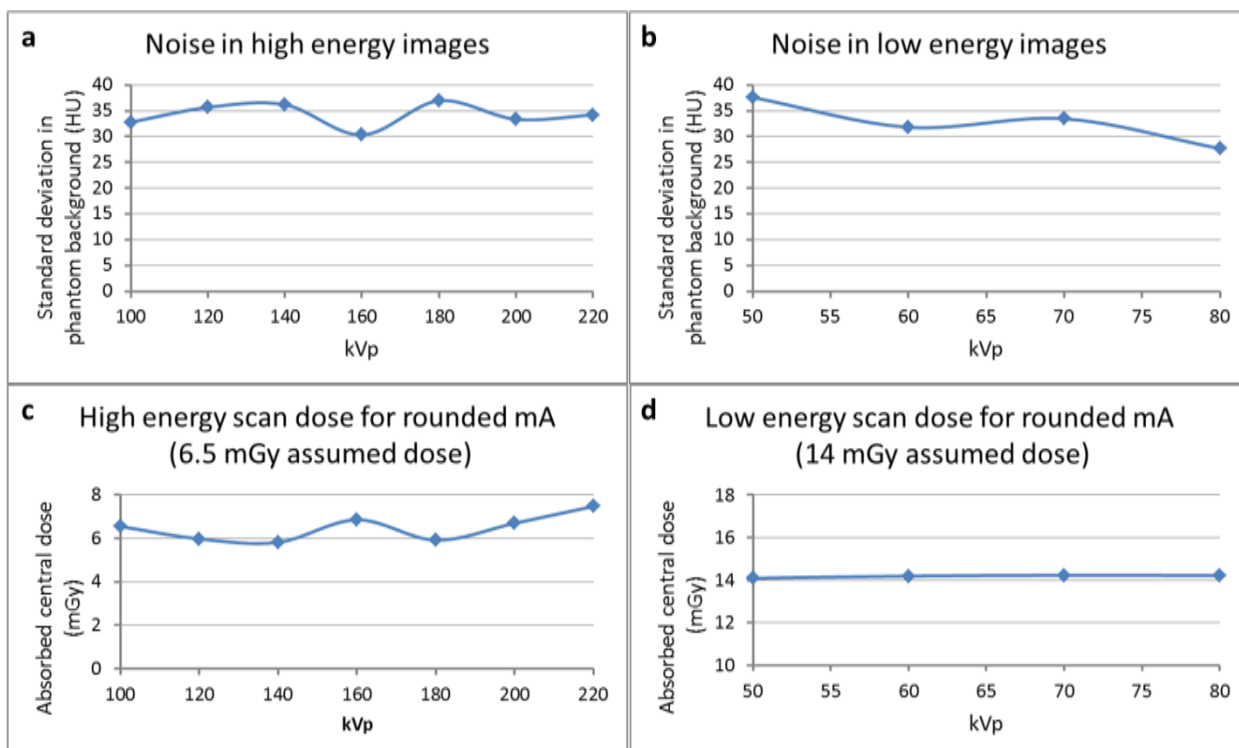


Figure 17: Noise levels in high (a) and low (b) energy images. Noise is taken as the standard deviation in a centrally located ROI in the solid water portion of the phantom. Variations in noise are primarily due to slight variations in dose due to mA rounding. With actual mA used (High dose in Table 2) the dose for high (c) and low (d) energy scans is as shown.

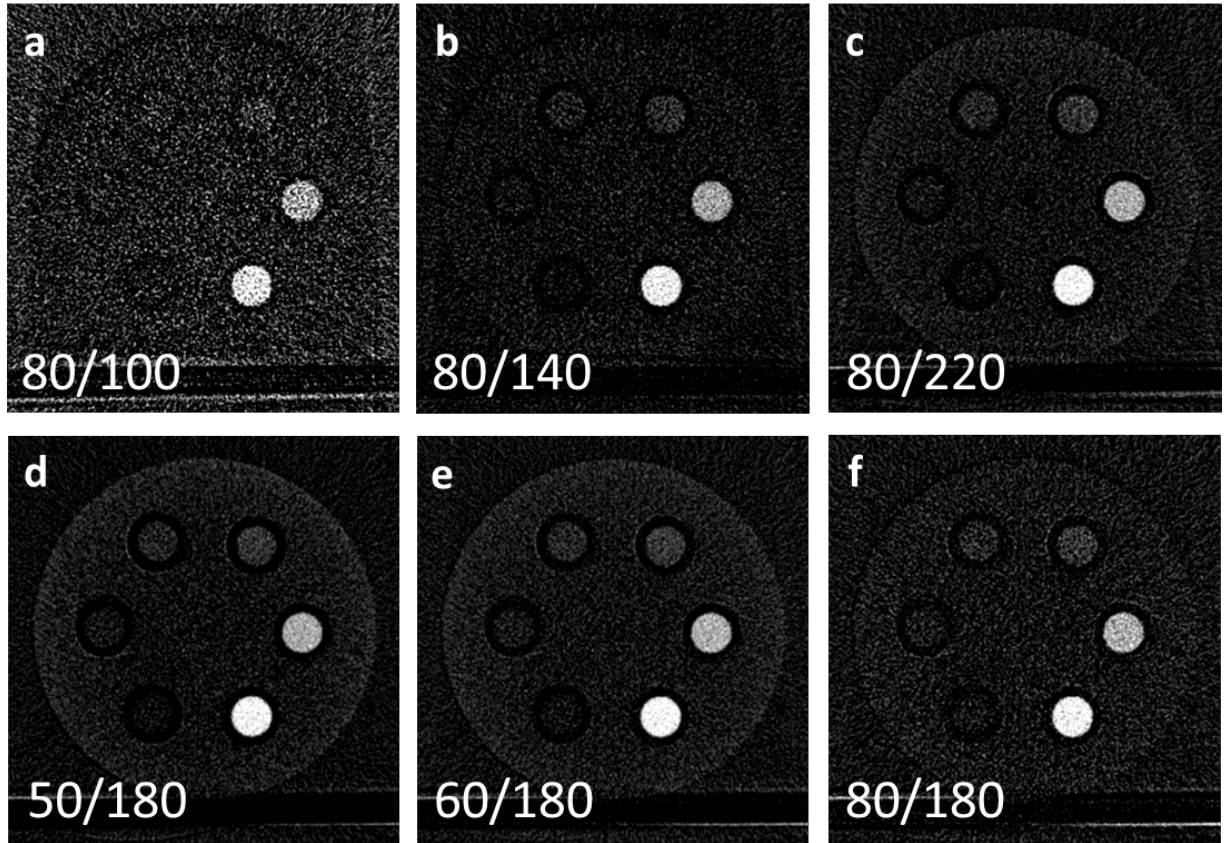


Figure 18: Iodine images demonstrating the effect of increasing the energy of the high energy scan (top row increasing from left to right) and increasing the energy of the low energy scan (bottom row increasing from left to right). An increase in CNR with increasing high energy kVp is easily seen in these images, with a less noticeable difference with changing low energy kVp.

An optimal kVp pair of 60 kVp and 200 kVp was selected as it had both the lowest between slice standard deviation in Iodine concentration error and CNR. Figure 19 shows Iodine images for this kVp pair alongside the kVp pair of 80 kVp and 140 kVp. This energy pair is used for comparison since it is a commonly used clinical kVp pair, and there is yet to be an accepted standard kVp pair for small animal dual energy CT. A 1.8 and 2.0 (5 and 3 mg I/mL, respectively) factor improvement in CNR and a 58% and 40% (30 and 20 mg I/mL, respectively) reduction in between slice standard deviation in Iodine concentration error was observed when using this optimal pair instead of the standard pair.

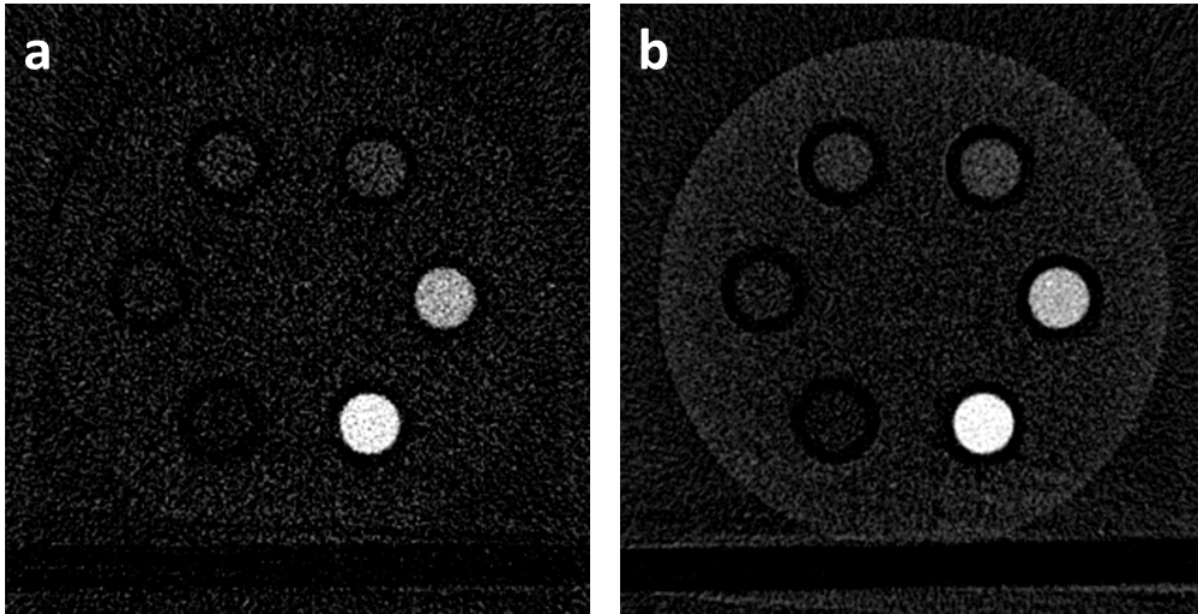


Figure 19: Comparison of iodine images for the standard 80/140 kVp pair (a) and optimized 60/200 kVp pair (b). Improvements in CNR are visualized in the optimized image.

2.3.4 Dose dependence

The dose dependence of the iodine error and contrast to noise ratio was also studied to understand the most appropriate ratio of low to high scan dose for different imaging goals. The dependence of iodine error on total dose is shown in Figure 20. The effect of changing the dose of the high energy scan while keeping the low energy scan dose at 14 mGy is shown in (a). As with similar graphs for different low energy doses, no clear pattern in how the iodine error changes with increasing high energy dose. Figure 20 (b) shows the effect of changing the dose of the low energy scan while keeping the dose of the high energy scan at 6.5 mGy. A clear decrease in iodine error is observed for increasing dose. While only scans with 50 kVp as the low energy are shown, similar trends were observed at other low energy kVp and for other high energy scan doses. Taken together, the graphs in Figure 20 suggest that to improve quantitative accuracy without increasing total dose, more of the dose should be allocated to the low energy scan.

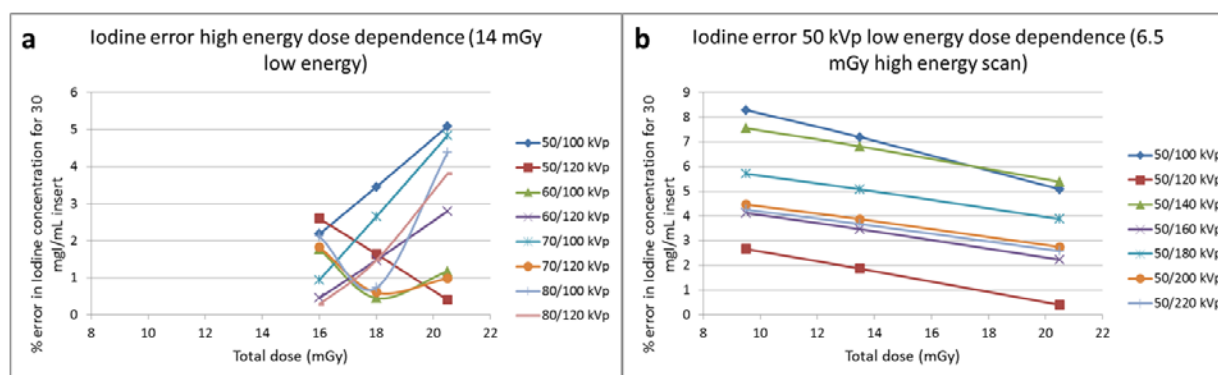


Figure 20: Dependence of Iodine error on changing the high energy dose with a constant low energy dose of 14 mGy (a) and on changing low energy dose with a constant high energy dose of 6.5 mGy (b). Only 50 kVp energy pairs are included in (b), but similar trends were observed with other low energy kVp.

Figure 21 shows similar graphs for the dose dependence of the contrast to noise ratio with high energy dose dependence in (a) and low energy dose dependence in (b). Since CNR is directly inversely proportional to noise, it is no surprise that the CNR increases with increasing dose. What is interesting to note is that the CNR increases more rapidly with increasing total dose when the high energy dose is varied. This difference suggests that to improve CNR with constant total dose, more of the dose should be allocated to the high energy scan.

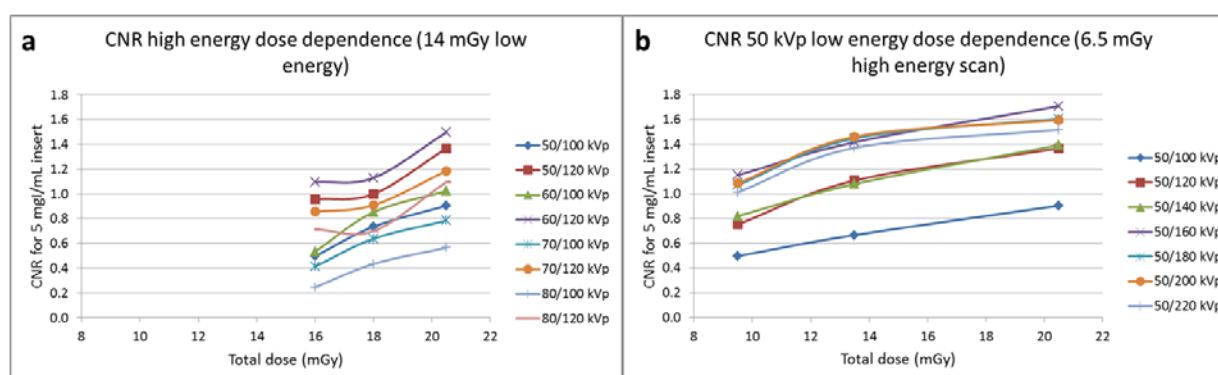


Figure 21: Dependence of CNR on changing the high energy dose with a constant low energy dose of 14 mGy (a) and on changing low energy dose with a constant high energy dose of 6.5 mGy (b). Only 50 kVp energy pairs are included in (b), but similar trends were observed with other low energy kVp.

From the dose dependence of both the Iodine error and CNR we observe that the ideal dose allocation between low and high energy scans depends on the application. For applications where quantitative accuracy of the Iodine concentration is important, more of the dose should be allocated to the low energy scan, whereas for applications where visualizing low concentrations of Iodine is important, more dose should be allocated to the high energy scan.

2.4 Discussion

Results from both simulations and scans on the X-RAD suggest that while increasing the kVp separation between the low and high energy scans has little impact on the accuracy of Iodine concentration measurements, it does improve both the precision in Iodine measurements and visibility of low concentrations of Iodine. These improvements are both directly tied to a reduction in noise with increasing kVp separation. This noise reduction is predicted and demonstrated in a number of studies¹⁸⁻²⁰, but this study is the first to our knowledge to demonstrate this behavior with a range of high energy kVp's above 140 kVp to show the continued improvement with increasing high energy kVp. The roughly factor of 2 increase in CNR for the best-measured CNR (60 kVp and 200 kVp) over the CNR for a common kVp combination (80 kVp and 140 kVp) represent a substantial improvement justifying the use of such kVp combinations.

Results of this study lend support to the other studies suggesting a larger dose allocation to the high energy scan improves noise behavior. They also suggest that Iodine accuracy is more sensitive to the dose in the low energy scan than the high energy scan. However, the extent of doses used in this study was not enough to determine the specific dose allocation that would best balance these dose dependencies for specific tasks. This lack of data was in part due to limitations in the mA that could be used for high kVp. The mA that could be used was confined from both sides, with too low mA not being

stable enough and too high mA saturating the detector. As a result, sometimes only one dose level was possible for the high energy scan, limiting the dose allocations that could be studied.

Since the X-RAD was designed for image guided therapy and not for general imaging purposes, several limitations of the system prevent optimal dual energy imaging especially at the high kVp. One limitation is that it is limited to sequential scanning dual energy CT, where the high and low energy scans are done one after the other. This configuration is not ideal, since motion can occur between scans, causing differences between the high and low energy images that are not due to attenuation differences. Additionally, the Iodine distribution may change between scans. Care should be taken, therefore, to immobilize the mouse properly to limit between scan motion, and to ensure that the Iodine distribution of the contrast agent used is stable at the time of image acquisition. Additionally, the detector was not designed for high kVp imaging, causing it to become saturated at low mA for the high energy kVp's used in this study. With only low mA available for the high energy scan, either the total dose or the dose allocation to the high energy scan was limited, adding to the image noise. Using a lower gain mode for the detector may mitigate this problem by allowing for higher mA before detector saturation. If designing a small animal dual energy system from scratch, these limitations can be addressed, while still utilizing an x-ray source capable of producing the high energy kVp's used in this study. For example, a dual source system with one x-ray/detector system optimized for low energy scans and the other for high energy scans would address these shortcomings.

There are several limitations of this study beyond the limitations of the XRAD that were just discussed. While the dose used for the high or low energy scans was matched as closely as possible, the X-RAD system requirement that mA to be rounded to the nearest 10th combined with the low mA used prevented exact dose matching. Some of the observed deviations from linear in the CNR and Iodine accuracy graphs are likely a result of this approximation in dose matching. Furthermore, dose was

assumed to vary linearly with kVp and was extrapolated from manufacturer supplied dose as a function of kVp up to 100 kVp. Ideally, the dose should be measured for different kVp up to 220 kVp to ensure this linear relationship continues to hold past 100 kVp. These dose measurements represent future work, and may necessitate repeating energy pair comparisons if large deviations in dose are observed. Additionally, only phantom measurements were used in this study. Few studies that include Iodine contrast agents in mice have reported on the actual concentration of Iodine seen in mice. The concentrations used in the phantoms for this study were based on figure legends of maximum intensity projection images from a paper by Moding et al using dual energy to study tumor vasculature⁶. If Iodine concentrations in mice differ substantially from what was used in this study, the concentrations of Iodine used for calibrations in this study may not be appropriate. As the concentration of Iodine in mice injected with available contrast agents becomes better understood, the calibration concentrations should be adjusted appropriately. Finally, no noise suppression was used in this work. Various dual energy studies have suggested and tested utilizing the “anticorrelated” nature of dual energy noise (a voxel in a uniform area that is above the mean in one material image will be below the mean in the other) to reduce material image noise⁵⁸⁻⁶². Such techniques cannot completely get rid of noise, so using an image with less noise to begin with would still be beneficial. However, the improvements seen in CNR by increasing the spectra separation may be less than what is reported here once noise reduction techniques have been applied.

As discussed in the overall introduction, breathing motion represents a challenge for dual energy CT of small animals. The next chapter discusses a strategy for obtaining a respiratory signal in mice that can be used for respiratory gating in dual energy. If only images taken during peak exhale (the most stable breathing phase) are reconstructed, the influence of motion could be reduced. Future work includes applying the strategies covered in the coming chapter to dual energy images in mice.

2.5 Conclusion

The aim of this chapter was to determine the optimal imaging parameters for quantification of material density and low contrast detectability for contrast enhanced dual energy CT on the X-RAD system. The working hypothesis for this specific aim was that the optimal energy pair for dual energy imaging on the X-RAD will have improved quantitative accuracy of more than 5% in iodine concentration error and 50% in contrast to noise ratio over the standard 80 and 140 kVp. We have found an optimal kVp pair for these purposes. This optimal kVp pair (60kVp/200kVp) had a greater than 50% increase in CNR, however, an increase in iodine concentration accuracy was not confirmed due to inherent variation in iodine measurements being larger than differences based on kVp pair. Instead low overall error in iodine measurements was observed for all kVp pairs.

Chapter 3: Translation of several data driven 4D CBCT techniques to mice

The Methods, Results, figures and tables and portions of the Introduction and Discussion of this chapter were reprinted from the following⁶³ with permission:

R. Martin, A. Rubinstein, M. Ahmad, L. Court and T. Pan, "Evaluation of intrinsic respiratory signal determination methods for 4D CBCT adapted for mice", *Medical Physics* **42** (1) (2015).

3.1 Introduction

For the purpose of improving quantification and localization of Iodine in moving structures for dual energy CT, 4D imaging and retrospective gating are developed on the X-RAD small animal irradiator. These types of images are also important in small animal radiotherapy as they allow tumor motion to be accounted for in the planning of the treatment. The focus of this chapter is placed on the respiratory signal, as errors in the identification of respiration peaks can lead to image blurring and misrepresentation of the tumor motion (See Section 3.3.6). Specifically, as mentioned in the introduction, we aim to obtain the respiratory signal directly from the cone beam projections, as this minimizes setup cost and complexity and represents a signal more closely related to internal motion.

Several groups have used cone beam projections to obtain a respiratory signal for mice on other systems. Using a system with a step-and-shoot image acquisition, Chavarrias et al. subtracted images at each angle from an average image at that angle to enhance areas of motion²⁸. They then summed the pixel intensities in the image to get a respiratory signal for each angle. This method was a modification from a previous method by Hu et al. in which the pixel intensity values within a ROI

were used to find a respiratory signal for each angle ²⁹. However, the Chavarrias method cannot be applied as is to systems, like the X-RAD, which do not have the option to acquire data in a step-and-shoot fashion. Bartling and Dinkel et al. tracked the center of mass (COM) in an ROI on a system that could achieve frame rates of up to 100 fps with a limited FOV ³⁰ and Kuntz automated this method on the same system ³¹. Ertel et al. modified the COM method in a system with a slower, 25 fps, frame rate ³².

In addition to the methods mentioned that have been applied in mice, some methods have been tested in human CBCT imaging that may potentially be applicable to small animal imaging as well and provide improvement over existing methods used in mice. Kavanagh, like Hu, used the sum of pixel values within an ROI as the respiratory signal ²². In what has become known as the Amsterdam Shroud (AS) method^{23, 24} one-dimensional projections of edge-enhanced projection images are used to extract the respiratory signal. While this method was shown to work well in situations where the diaphragm is clearly visible in all of the projection images, the signal becomes difficult to pick out when the diaphragm is not included^{22, 23, 25}. Vergalaso et al. used a method that relied on the Fourier shift theorem ^{26, 27} to find the respiratory signal. Spatial shifts were monitored by tracking changes in the phase of the Fourier transform. This method showed some improvement over the AS method when the diaphragm was not visible, but showed dependence on the size of the region of interest ²⁵. They also used the amplitude of the Fourier transform to obtain a respiratory signal. However, this method is effectively the same as the intensity based method of Kavanagh. More recently Yan et al. used feature extraction and principal component analysis on AS images ²⁵. This method improves upon the AS method by removing background information through the feature extraction and isolating oscillations caused by respirations from those caused by the rotation of the gantry through the principle component analysis.

These methods can potentially be applied to small animal imaging for respiratory signal extraction that does not rely on step-and-shoot image acquisition. Of the methods tested in small animals, currently only the COM method can be used without modification in systems without a step-and-shoot acquisition option. Methods, such as the AS and Fourier transform, that perform well in humans with the right regions scanned and selected for analysis can be expected to also perform well in mice since the entire mouse is in the scan field of view. Direct application of human techniques of respiratory signal extraction in mice is not guaranteed, however, due to the higher frequency of breathing and different breathing patterns. When mice are anesthetized, which is typically done for imaging, they tend to spend much of the breathing cycle in a nearly motionless exhalation, which is followed by an abrupt inhalation⁶⁴ (as an example, the mice in this study spent approximately 60% of the time with no diaphragm motion and only 15% of the time in inspiration). The purpose of this work is to compare several of these methods for their applicability in small animal 4D CBCT with modifications being made as necessary to tailor the methods to mouse as opposed to human imaging. The Amsterdam shroud, intensity based, and Fourier transform methods were chosen for their effectiveness in humans. The method used by Yan et al. was excluded from this study since it requires an Amsterdam Shroud image which was found to be qualitatively different in mice and humans. These were compared to the existing method, center of mass, for non-step-and-shoot small animal systems to look for significant improvements in accuracy that can be gained by adapting established human methods to mice.

3.2 Methods

3.2.1 CBCT scanning protocol

As part of a separate study, 9 mice cone beam CT scans at 60 kVp and 4 mA were obtained on the X-RAD 225Cx (Precision x-ray, North Branford, CT). The five mice used in this study had a

strong predisposition to lung cancer and tumors were visible in several of the scans. The mice were anesthetized with 1.5-3% isoflurane and allowed to breathe freely during image acquisition. A sampling rate of 15 frames per second and a single gantry rotation at 0.5 rotations per minute were chosen in order to adequately sample the respiratory signal. In total, roughly 1800 projections were obtained for each scan with about 100 breath periods for each scan. No pixel binning was performed giving a useable projection size of 975x975 pixels of size 0.2 mm.

3.2.2 Respiratory signal determination

The respiratory signal necessary for 4D and retrospective gating reconstruction was obtained using five different methods as outlined below.

3.2.2.1 Modified Amsterdam shroud method

The first method used was modeled after the so-called Amsterdam Shroud method proposed by Zijp et al. for respiratory signal determination from human cone beam CT projections²⁴ and will be referred to as the modified Amsterdam Shroud method (mAS). Briefly, a region of interest was manually placed on the first projection such that it enclosed the entire diaphragm and width of the mouse in each of the projections. After log normalization, a sobel filter (a derivative filter which enhances edges in a specific orientation) was used to enhance edges along the direction of the diaphragm. For each projection image, pixel intensities were summed to create a projection along the cranial-caudal axis, and these one-dimensional projections were combined into a two-dimensional “shroud” image. Previous implementations of this method in humans focused on extracting the sinusoidal variations in the shroud to get the respiratory signal. However, due to the difference in anesthetized mouse breathing, the mice shrouds contained essentially vertical lines over a slowly varying background as shown in Figure 22. The following modifications were made to the Amsterdam Shroud method as part of this work so that it could be used in mice. An additional

sobel filter was used to enhance the vertical lines in the shroud, as opposed to horizontal enhancement in the original method, giving a set of high contrast lines for each peak inspiration and suppressing the background variations between the peaks. It is not necessary in this case to register each of the columns as was done in the original method. Instead, the columns were summed to give a signal such as the one shown in Figure 23. This signal is not strictly speaking a respiratory signal since the peak inspirations are not peaks in the signal but a valley between the two peaks associated with the two high contrast lines after edge enhancement. However, these valleys can be automatically picked out of the signal as described in Section 3.2.3, allowing the peak inspirations to be found from this signal.

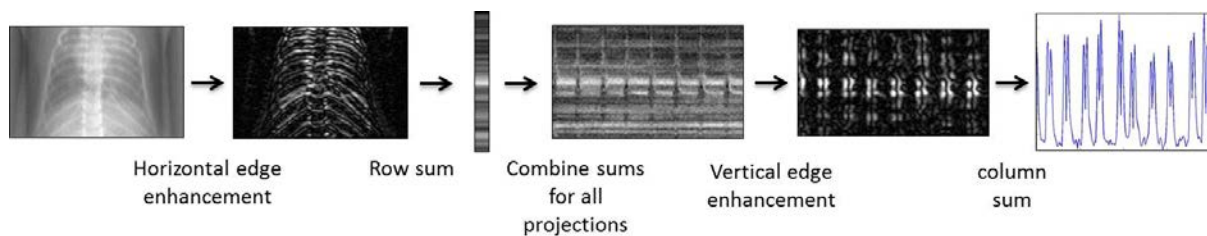


Figure 22: Diagram of the modified Amsterdam Shroud method showing from left to right the region of interest in the original projection, edge enhanced ROI, horizontal sum, Amsterdam shroud, edge enhanced shroud, and signal.

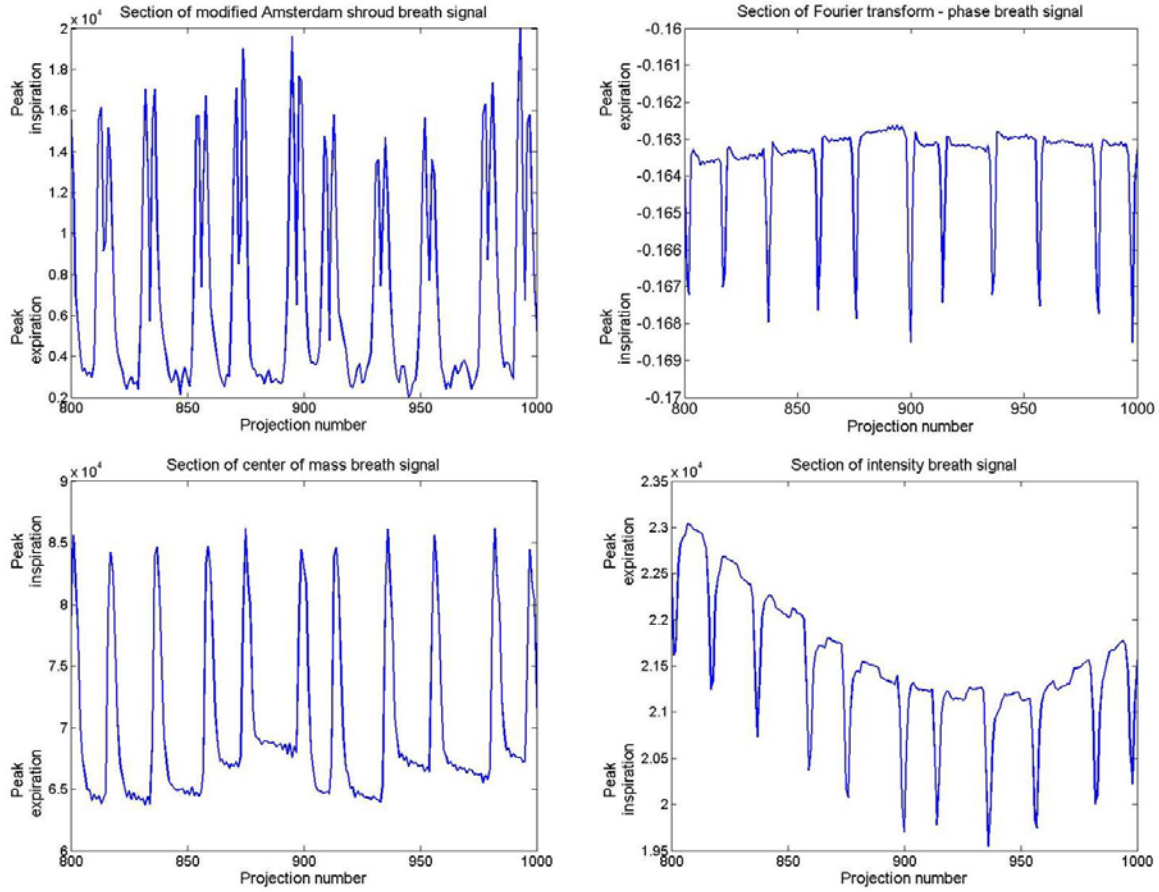


Figure 23: Sections of respiratory signals obtained using the mAS (top left), FT-p (top right), COM (bottom left), and Intensity (bottom right) methods. The direction of inspiration and expiration is indicated next to the figures (peak inspiration for the mAS method is a valley between two positively oriented peaks).

3.2.2.2 Fourier Transform phase method

Following the method of Vergalasova et al., the Fourier shift theorem, which states that a spatial shift in a function manifests as a phase shift in the Fourier transform, was utilized to find the respiratory signal^{26, 27}. This method will be referred to as the Fourier transform-phase method (FT-p). Pixels outside of the ROI described above were set to zero and a two-dimensional Fourier transform and its corresponding phase component were calculated. As in Vergalasova the value of the pixel corresponding to the DC component in the left-right direction and lowest non-DC

frequency in the cranial-caudal direction was tracked to obtain the respiratory signal like the one shown in Figure 23. The zero-padding was done so that looking at the same pixel location gives the same frequency component regardless of ROI size²⁷. Without the zero-padding this method would be more heavily influenced by higher frequencies, such as noise and cardiac motion, for small ROIs since the lowest non-DC frequency division includes a larger range of frequencies.

3.2.2.3 Intensity method

Based on the method of Kavanagh²², pixel intensity values were summed within a region of interest for each projection and used as the respiratory signal as shown in Figure 23. We chose not to use a high pass filter to remove the slowly varying component of the signal from the gantry rotation since the algorithm we used to find the peaks in the signal was generally able to locate all the peaks.

3.2.2.4 Center of mass method

The existing center of mass method (COM) tracks the location of the center of mass along the direction of motion of the diaphragm (the z axis). Pixel values in an ROI were projected onto the z axis, and a weighted sum based on the z position ($z = 0$ defined as the center of the ROI) of the pixels was performed³⁰. Mathematically this process is expressed as

$$COM = \frac{1}{M} \sum_z m_z Z, \text{ with } M = \sum_z m_z \quad \text{Equation 5}$$

where m_z is the sum of pixels at a particular Z location. A representative signal is shown in Figure 23.

3.2.2.5 Manual method

Since an external monitoring device was not available for the study, a manual method was used to determine the true respiratory signal. The projection images were scrolled through and locations of the peak inspirations (when the dome of diaphragm was most inferior) were noted.

3.2.3 *Four dimensional image reconstruction*

For each respiratory signal, the locations of the peak inspirations were automatically picked out using an algorithm that looked at both the sharpness (first derivative) and value at each point in the signal. Points that had derivatives above a specified sharpness threshold (predetermined fraction of highest first derivative present in the signal) were selected and the difference in projection number of each of these points to the next was determined. Selected points that were within a specified maximum distance from surrounding selected points were grouped together along with a specified number of points to each side of the region. Within each group, the highest valued point was considered a peak assuming that it had a value that surpassed the value threshold (determined in a similar manner as the sharpness threshold). Prior to peak extraction it was assured that the peaks had a positive polarity and that the minimum value of the signal was zero.

Modifications to this algorithm were needed to find the peak inspirations in the distinctive mAS signal. Points were grouped together based on sharpness as before. The maximum distance allowed between points within the same group was increased such that both peaks surrounding the valley of interest are considered part of the same group. Each group was divided evenly in half, and the peak for each half was found as before. The lowest point between these two peaks was considered the peak inspiration. Parameters of the algorithm were adjusted for each method but held constant for all testing for a particular method. We observed that, in general, when we were able to visually distinguish peaks from background noise, the algorithm was also able to, but it sometimes missed or added additional peaks when noise levels were high. Other peak finding algorithms can conceivably be used with similar overall results, assuming they can similarly identify peaks in the presence of background noise or slow variations in signal intensity (or these features have been reduced in the signal before peak finding). Each breathing period was evenly divided into 8 phases and the

projections were sorted into these phase bins. Each phase bin was reconstructed using an FDK algorithm and combined to form a 4D image with voxel sizes 0.1 x 0.1 x 0.3 mm.

3.2.4 Modified four dimensional imaging

Since anesthetized mice spend much of their breathing cycle in motionless expiration most of the 4D phases provide repetitive information. To better utilize the information available, we developed what is essentially a cross between 4D imaging and retrospective gating. Again each breathing period was divided evenly into 8 phases with phase 1 as peak inspiration. Phases 3 through 7 were combined before reconstruction and phases 8, 1, and 2 were reconstructed separately. We are left with an image of peak inspiration, two images showing the transition into and out of peak inspiration, and a high quality image showing peak expiration. This method requires prior knowledge of the approximate proportion of time the diaphragm of the mouse moves. We measured the fraction of time the diaphragm moved and how much of that movement was due to the process of inspiration rather than expiration. We looked at the first 200 projections of each mouse and determined the fraction of projections where any movement and movement due specifically to inspiration were observed.

3.2.5 Region of interest size variation

In order to test the sensitivity of the respiratory signal extraction methods to the size and shape of the ROI, the height and width were varied for two mice for each of the methods. The width was varied from the full width to fully within the mouse (widths: 975, 775, 575, 475, 375, 275, 175, 125, and 75 pixels). For the height variations, the center of the ROI was fixed at the superior end of the dome of the diaphragm at peak expiration and the height increased from 10 to 120 pixels in increments of 10 pixels (5 on either side of the diaphragm). For each ROI the FT-p, mAS, Intensity,

and COM methods were used to find the respiratory signal and the projections were sorted based on these signals.

3.3 Results

3.3.1 4D images

Four-dimensional images which demonstrated the expected breathing pattern were successfully created for each of the scans. Streak artifacts were observed, particularly in the axial and sagittal views, but did not prevent the study of lung motion in an in house study using these images⁶⁵. Peak inspiration phase images showed blurring of the diaphragm due to the large amount of motion within a short period of time during inspiration.

3.3.2 Modified 4D images

Modified 4D images were successfully created for each of the mice. As shown in Figure 24 the expiration image of the modified 4D image shows the same information as the peak expiration phase of the 4D image but with less noise and fewer streak artifacts. Additionally, there is little difference between the modified 4D peak expiration image and the full 3D image.

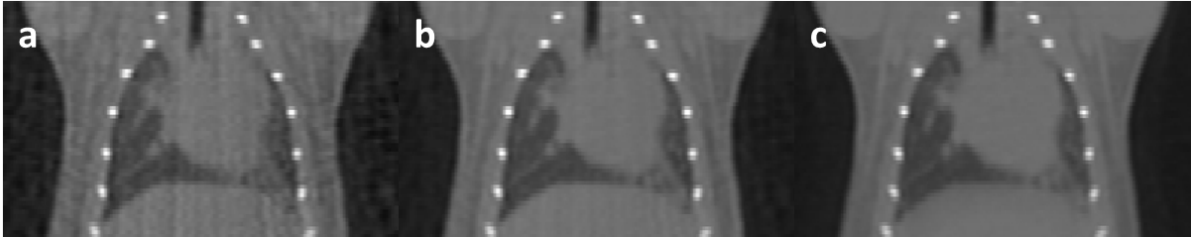


Figure 24: Peak expiration images obtained as part of an 8 phase 4D image (a) and a 4 phase modified 4D image (b) are compared against a full 3D reconstruction (c). The only difference observed between (a) and (b) is that there is noticeably less noise and streak artifacts in the modified 4D image. We do not observe differences in motion blurring between the (b) and (c) even though the projections where the diaphragm are moving have been removed from (b).

3.3.3 Mouse breathing patterns

We found an average of 39.4 % with standard deviation 10.0 % of projections had noticeable diaphragm movement and 16.6 ± 4.4 % of projections showed movement associated with the act of inspiration. We noticed there was little variation in the number of projections (3.3 ± 0.5 projections) involved in inspiration even when the breathing period showed large variation. This suggests that the mice take a roughly fixed amount of time, approximately 0.2 seconds, to inhale regardless of their rate of breathing.

3.3.4 Qualitative comparison of respiratory signal extraction methods

4D images created using the mAS, FT-p, and COM methods were compared qualitatively to images created using the manual method. As demonstrated in Figure 25 and Figure 26 only very small differences are observed between the images created with each of the methods. From difference images it was noted that except in a few isolated locations and phases, the difference between the tested methods and the manual method was in the location of the streak artifacts.

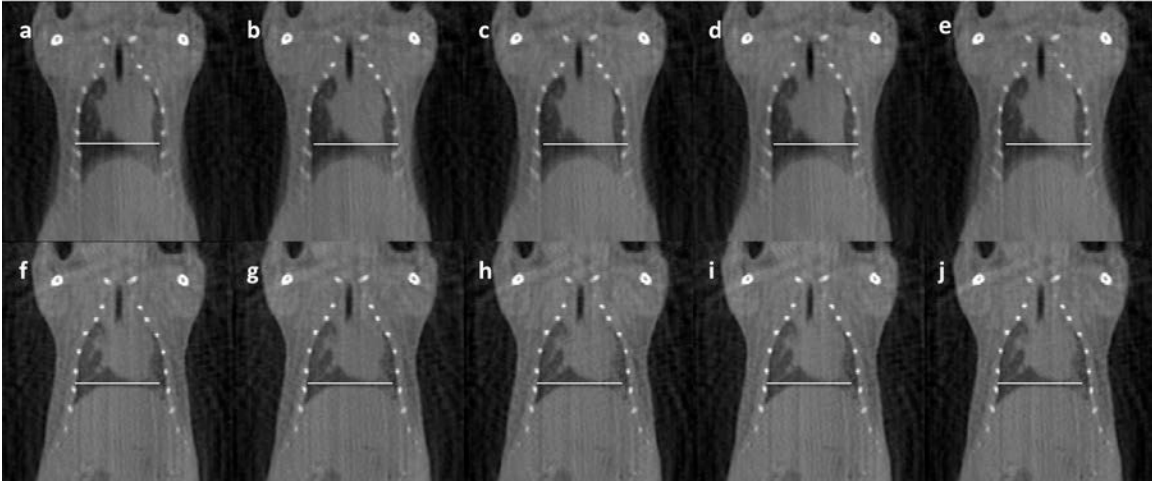


Figure 25: Coronal slices at peak inspiration (a-e) and peak expiration (f-j) for the manual (a,f), mAS (b,g), FT-p (c,h), Int (d,i), and COM (e,j) methods of respiratory signal extraction. Horizontal lines are added to emphasize the difference between inspiration and expiration and to make any differences in diaphragm position between the methods more obvious. No observable differences are noted between images produced by the different methods.

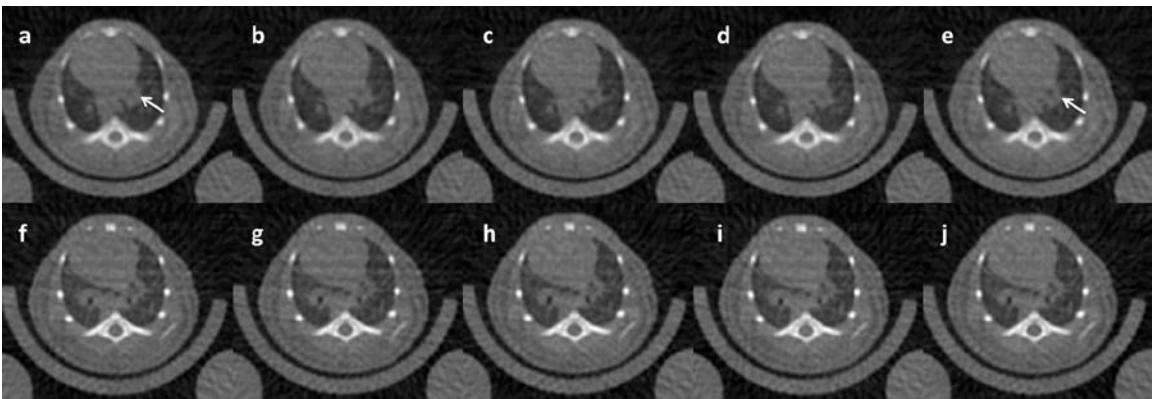


Figure 26: Axial slices at peak inspiration (a-e) and peak expiration (f-j) for the manual (a,f), mAS (b,g), FT-p (c,h), Int (d,i), and COM (e,j) methods of respiratory signal extraction. Minor differences are observed between the COM and manual methods and to a lesser extent the FT and manual methods in the peak inspiration images (ex. white arrows). No observable differences are noted between images produced by the different methods for the peak expiration images or between the mAS and Int and manual images.

3.3.5 Error in projection sorting

The sorting of projections into phase bins done by the manual method was considered ground truth. The projection sorting for each scan was compared to the ground truth to determine an error associated with each method. For each projection, the absolute value of the difference between the phase bins (numbered 1-8) of the method in question and the manual method was calculated, with wrap-around included such that phase 1 and 8 differed by one. These differences were averaged across the projections and expressed as a percentage of the breathing cycle (one phase is 12.5% of the breathing cycle). This metric was chosen over one comparing the location of the peaks since it more directly relates to the error in the images and includes the case of a missing or additional peak in a straightforward manner since there are large phase differences in these regions. However, this measurement does face the limitation that a phase shift can show up as having a high error despite the possibility of it only differing in the numbering of the phase bins. Therefore a second metric was used. The difference between the manual and tested method's bin assignment for each projection was again calculated, this time without taking an absolute value. A standard deviation (expressed as a percentage of the breathing cycle) of this quantity was taken and used as a metric to evaluate performance. Small standard deviation values would suggest that any errors in projection sorting are due to a phase shift, whereas larger values suggest errors that are more likely to result in errors in the images. However, note that a phase shift of a fraction of a phase bin can limit the ability to fully detect motion (see Section 3.3.6). In addition to these metrics, the difference in the number of peaks detected between the tested and manual method was quantified and reported in Table 7. Figure 27 demonstrates the effect of the error metric on the images by showing images at peak inspiration of selected results which had a range of errors. With an error of 2.5% only minor differences are seen. Differences in the shape and size of structures and a noticeable increase in the blurring of the diaphragm are observed with an error of 6.3%, which may

have an impact on applications that use these images. Increased blurring of the diaphragm and the structures visible is seen with an error of 13.8%. These differences are expected to be less in other phases where there is little difference between adjacent phases due to little motion. Across the 8 scans considered, the average error was $3.1 \pm 1.1\%$ for the FT-p method, $1.1 \pm 0.4\%$ for the mAS method, $1.2 \pm 0.2\%$ for the Intensity method, and $4.7 \pm 1.2\%$ for the COM method (one mouse was removed from quantitative analysis since it was substantially off centered in the projections). The average standard deviation was $6.2 \pm 1.3\%$ for FT-p, $3.9 \pm 1.0\%$ for mAS, $4.2 \pm 0.9\%$ for Intensity, and $7.2 \pm 1.0\%$ for COM. The relatively high standard deviation values compared to the mean errors suggest that errors were not generally due to an overall phase shift, although a few isolated cases of phase shifts were observed. The FT-p, mAS, and Intensity methods all showed a statistically significant decrease in sorting error and standard deviation over the existing COM method ($p < 0.05$) and mAS and Intensity methods showed a statistically significant improvement over the FT-p method ($p < 0.005$). The mAS and Intensity methods showed no statistically significant difference in performance ($p = 0.8$ for mean and $p = 0.06$ for standard deviation).

Table 7: Peak number errors (Difference in the number of peaks detected between each tested method and the manual method for each of the 8 mice used in analysis.)

mAS	FT-p	COM	Int
0	0	0	1
-1	1	1	1
0	0	0	0
0	0	-1	0
0	0	0	0
0	0	0	2
1	0	0	0
1	0	0	0

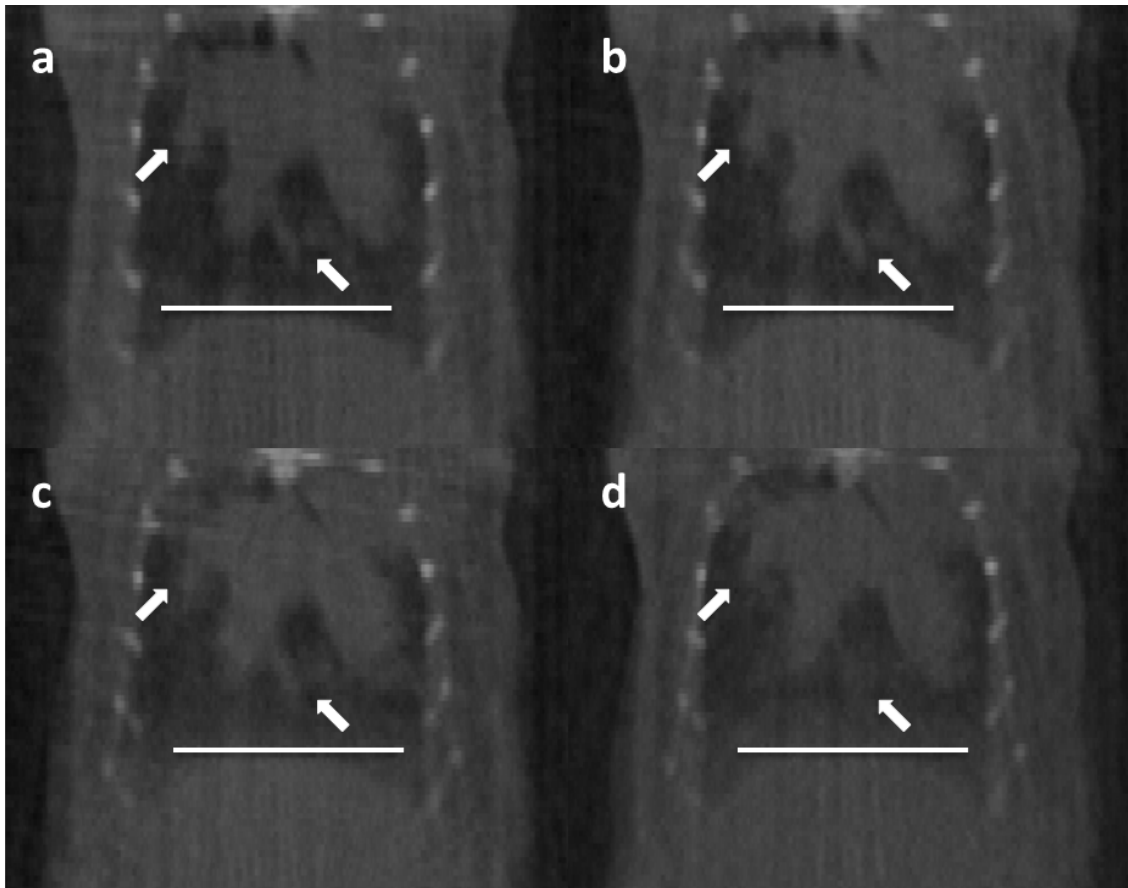


Figure 27: Visual effect of the error in projection sorting on coronal images of the peak inspiration phase. The manual method displayed in (a) is considered ground truth, arrows point to areas where differences were observed in some images, and the horizontal line indicates the top of the diaphragm for the manual method. The effect of increasing the error is shown in the remaining images (errors of 2.5% (b), 6.3% (c), and 13.8% (d)).

3.3.6 Effect of error on detected tumor motion

Since these methods may be used to evaluate tumor motion in mice, the effect on such a measurement was evaluated for a tumor in one of the mice (mouse 2 from the following section). Rigid registration of each phase to the peak inspiration phase in an ROI surrounding the tumor was done for images obtained using a subset of respiratory signals with a variety of errors. The signals used to create these images include a manual one, one with low error (1.3%), one with high error (13.8%) but no observed phase shift in the 4D image, and one with medium error (6.3%) and an

observed phase shift in the 4D image of a partial phase bin. Tracking of the tumor in the image with low error nearly matched that observed in the manual method image (Figure 28). However, both the phase shifted and high error images underestimated the total tumor motion. This underestimation was primarily due to a blurring of the tumor at peak inspiration with data that was not at peak inspiration.

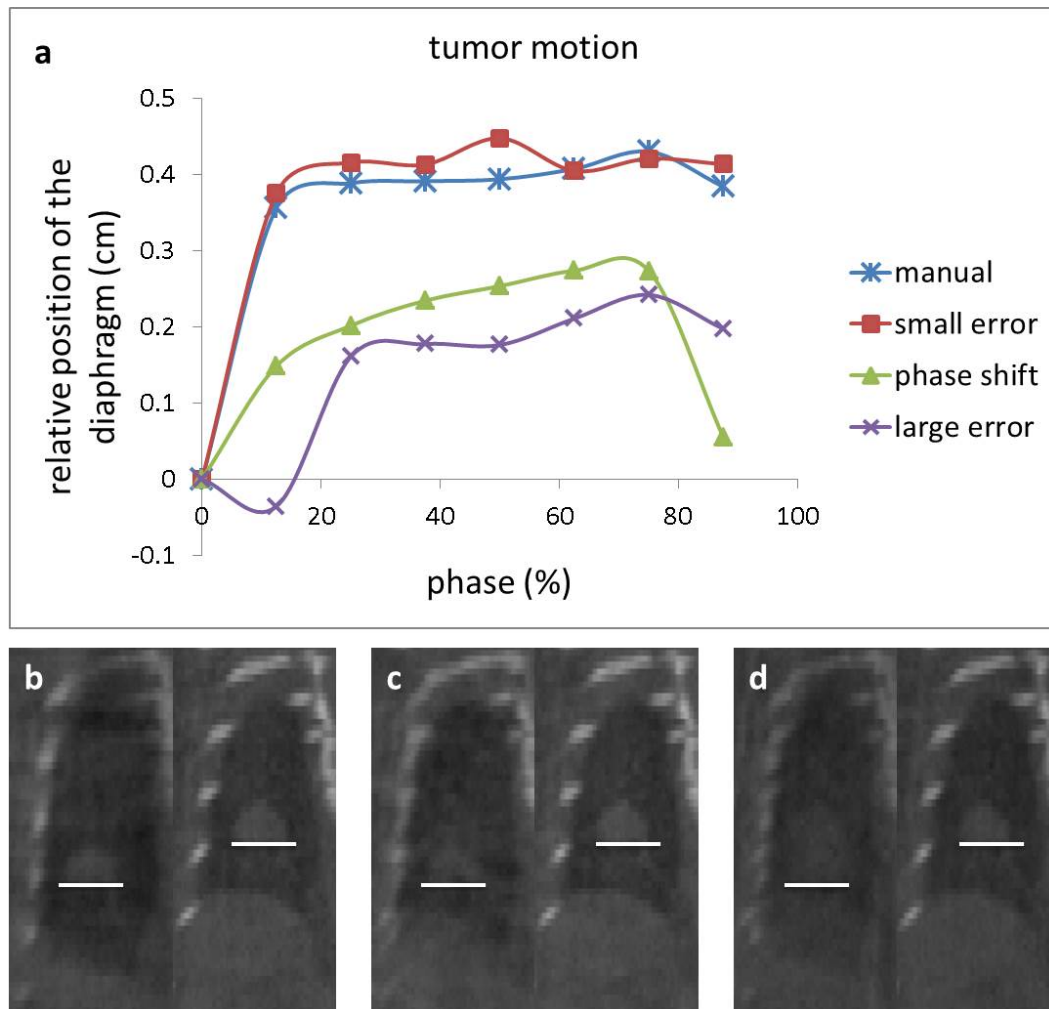


Figure 28: Graph of tumor position (a) for images with associated sorting errors of 0 (manual), 1.3% (small error), 6.3% (phase shift), and 13.8% (large error). Images at peak inspiration (left) and expiration (right) of the tumor are shown for the manual method (b), phase shift (c), and large error (d).

3.3.7 Dependence on ROI size

The error and standard deviation in projection sorting as a function of region of interest height is shown in Figure 29 and Figure 30 and the difference in number of detected peaks is shown in Table 8 and Table 9. The error and standard deviation have essentially the same height dependence. The Intensity method shows the least dependence on ROI height, essentially remaining flat as the height is increased. The mAS method shows a gradual decrease in the error and standard deviation as the ROI height increases. This decrease is more prominent in the second mouse than in the first. Large errors for small ROIs are observed for the FT-p and COM methods, with the FT-p method only noticeably showing this behavior for one mouse and the COM method having low error for the smallest ROI before peaking. It was observed that this peak was associated with a reversal of the polarity of the peak inspirations. With the same height, the projection sorting error relative to the full width remains essentially constant for the mAS and COM methods. However, for the FT-p method the error decreases by about 60-80 % from the full width to fully within the mouse. The intensity method shows some width dependence (up to a 45% change from highest to lowest error was observed). However, no clear pattern in this dependence was noted other than that the error was near its maximum for the full width and for ROIs that do not include the full width of the mouse.

Table 8: Height dependence of the number of detected peaks (Difference in the number of peaks detected between each tested method and the manual method)

height	mouse 1				mouse 2			
	mAS	FT-p	COM	Int	mAS	FT-p	COM	Int
10	0	3	0	0	4	37	0	0
20	0	0	5	0	0	17	0	0
30	0	0	3	0	0	6	0	0
40	0	0	0	0	0	2	4	0
50	0	0	0	0	0	-1	-1	-1
60	0	0	0	0	0	-1	-1	-1
70	0	0	0	0	0	-1	-1	-1
80	0	0	0	0	0	-1	-1	-1
90	0	0	0	0	0	-1	-1	-1
100	0	0	0	0	0	-1	-1	-1
110	0	0	0	0	0	-1	-1	-1
120	0	0	0	0	0	-1	-1	-1

Table 9: Width dependence of the number of detected peaks (Difference in the number of peaks detected between each tested method and the manual method)

width	mouse 1				mouse 2			
	mAS	FT-p	COM	Int	mAS	FT-p	COM	Int
75	0	0	0	1	0	0	0	-1
125	0	0	0	1	0	0	0	0
175	0	0	0	1	0	0	0	0
275	0	0	0	1	0	0	0	0
375	0	0	0	0	0	0	0	0
475	0	0	0	0	0	0	0	0
575	0	0	0	0	0	0	0	0
775	0	0	0	0	0	0	0	0
975	0	0	0	1	0	0	0	0

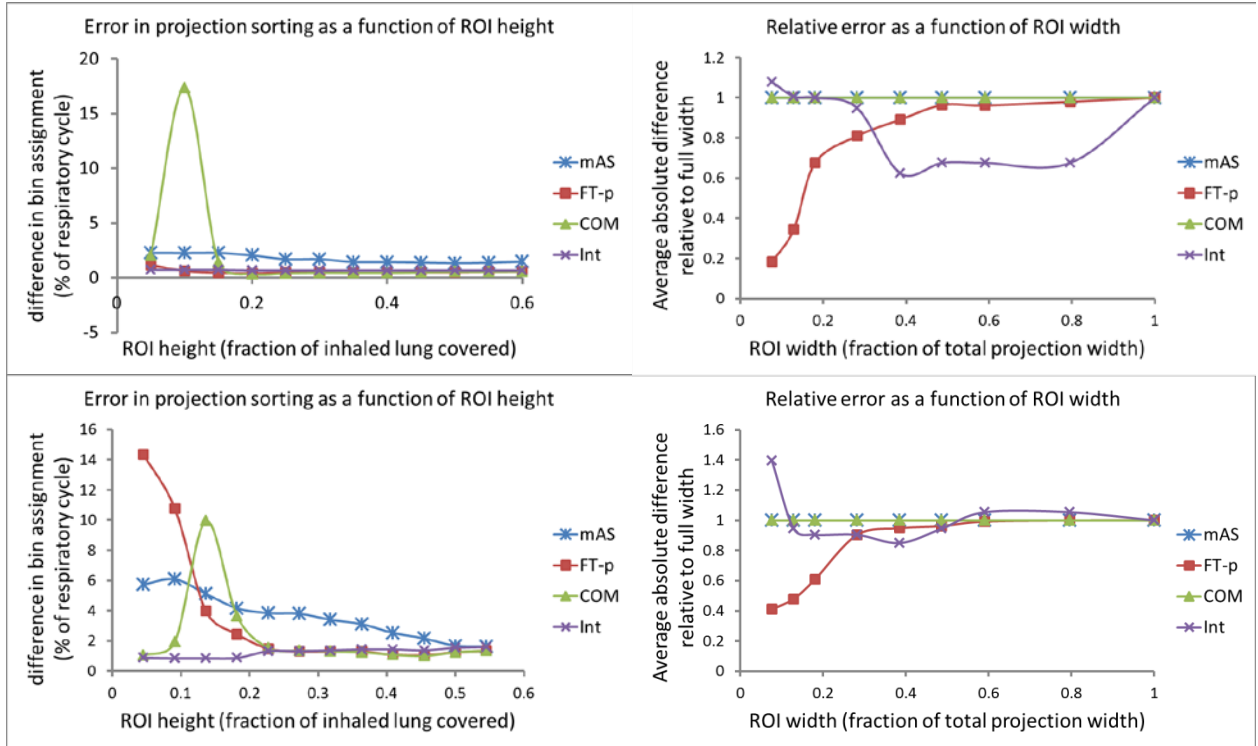


Figure 29: Dependence of the error in projection sorting on ROI height (left) and width (right) for two mice (top and bottom). Error is defined as the average across the projections of the absolute value of the difference between phase bins for the method in question and the manual method. It is expressed as a percentage of the breathing cycle. For width dependence, error is displayed relative to the error for the full width of a well performing ROI height such that an error of 1 means there is no change in error between that width and the full width. It is observed that while the error for the mAS decreases gradually with ROI height and the error for the Intensity method remains essentially constant, the error for the FT-p and COM methods have relatively high error for small ROIs. Additionally the mAS and COM show no dependence on width while the error of the FT-p method decreases with decreasing width and the Intensity method shows some dependency on width.

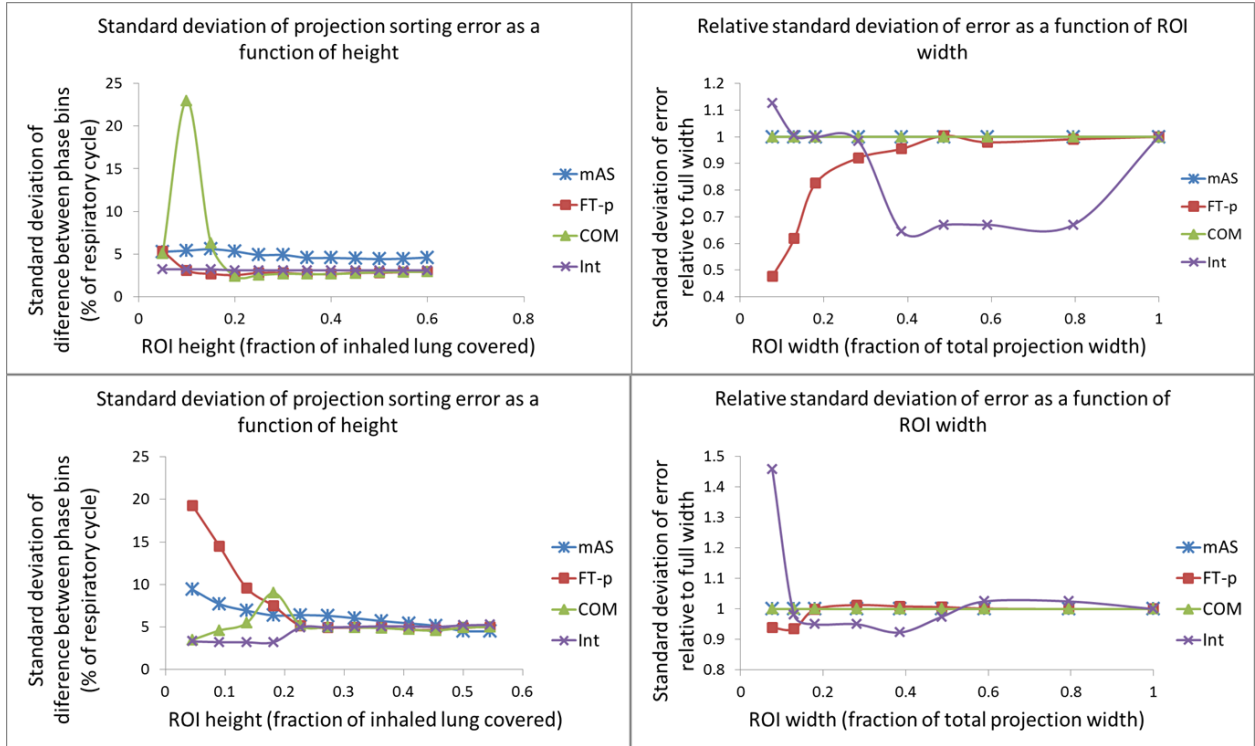


Figure 30: Dependence of the standard deviation in projection sorting on ROI height (left) and width (right) for two mice (top and bottom). Standard deviation was calculated by finding the difference in phase bin number between the method in question and the manual method and finding the standard deviation of this quantity for all projections. It is expressed as a percentage of the breathing cycle. The height and width dependence of the standard deviation is similar to that of the error in Figure 29.

3.4 Discussion

Each of the methods for respiratory signal extraction, the Fourier transform, modified Amsterdam Shroud, Intensity, and center of mass methods, were able to be used to create 4D images that had only minor differences from those created using the standard manual method. However, differences were observed in the error and standard deviation in projection sorting and in the sensitivity of these metrics to the ROI size. The mAS method showed little dependence on the ROI size or shape, only a gradual decrease in error as the amount of lung coverage was increased. This method largely picks up on the movement of the diaphragm, so as long as it is fully included,

adding extra moving tissue does little to improve the signal. While increasing the ROI beyond the useful area adds extra background, the signal is strong enough after edge enhancements to still be observed and the background usually does not change the location of the peak. This relative insensitivity is useful in attempts to automate the entire process, including ROI selection, as slight errors in ROI selection are not expected to have a noticeable impact on the resulting signal. If careful selection of an ROI is feasible, however, it is recommended for best results to include the most inferior portion of the lungs up to mid-lung or higher and extend from just to the left of the mouse to just to the right.

The COM method similarly showed no dependence on the width of the ROI. Like the mAS method, increasing the width of the ROI increases the amount of background averaged into the pixel sum, and with a strong enough signal does not affect the location of the peaks. The COM method did however show a greater sensitivity to the ROI height. An interesting feature of the height dependence is a prominent peak in the error as the height increases for small ROI heights. This peak corresponds to a change of the peak inspirations being at the valleys of the respiratory signal to them being at the peaks as demonstrated in Figure 31 (a change in polarity). In the regions of transition of polarity the height of the peaks decreased making them difficult to distinguish from background noise. In addition to the possibility of peaks becoming lost in the background, the unknown polarity of the signal makes a fully automated peak inspiration determination with this method difficult. To use this method, careful manual selection of the ROI, or sufficiently sophisticated automatic ROI selection algorithm, should be used to ensure the polarity of the signal is known and not in the transitional region. The ideal ROI should reach from the most inferior portion of the lung to near the most superior portion and from just to the left of the mouse to just to the right.

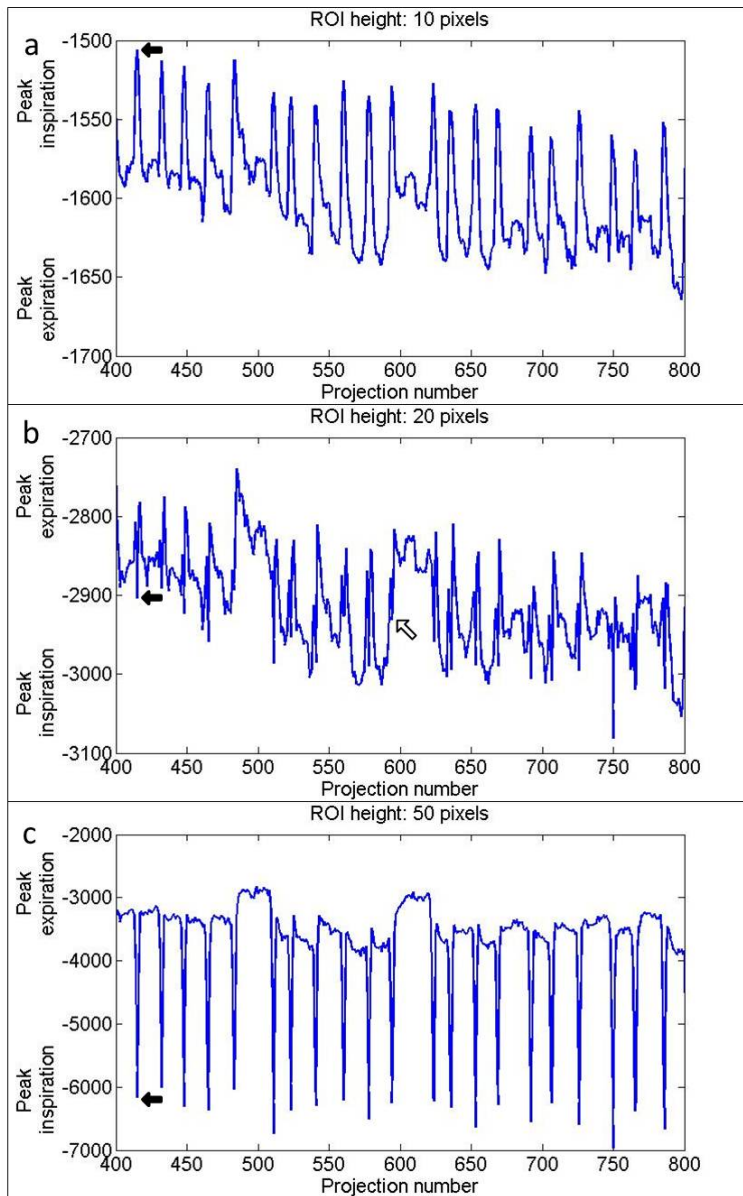


Figure 31: Sections of COM method respiratory signals for different height ROIs: 10 (0.7 mm) (a), 20 (1.4 mm) (b) and 50 (3.7 mm) (c) pixels. The black arrows indicate the location of the first peak inspiration which switches from a peak (a) to valleys (b,c) as the ROI size increases. In the transition (b) some peaks become lost to background noise (e.g. white arrow).

The FT-p method shows sensitivity to both ROI height and width. This observation is consistent with the assessments of Yan in human patients as well as Vergalasova's own observations²⁵⁻²⁷. The more dramatic observations in this case compared to human cases are likely the result of the inclusion in the projections of the whole mouse and large margins around the mouse in the projection data. This difference makes for more ways for ROIs to include different sections of lung and background. The FT-p method shows a similar increase in error with changes in height due to a change in polarity as the COM method (although we do not observe the opposite polarity before the transition in this case). The similarity in behavior is expected when we consider that changes in the phase of the Fourier transform are related to the shift in the center of mass of the image by the Fourier shift theorem. However, the FT-p method does not give us exactly the center of mass change, as it only tracks one pixel in the phase image, corresponding to one frequency component of the image. The lower error of the FT-p method may be explained when we consider that the FT-p method is only tracking center of mass shifts of low frequency components of the image while the center of mass method tracks shifts from all frequency components, leading to a noisier signal. The ideal ROI method is the same as that for the COM method, with care being required to avoid large margins to the side of the mouse or small ROIs in the height direction.

The Intensity method shows the least dependence on ROI height. However, it shows somewhat unpredictable dependence on the width of the ROI. While the ROI width analysis did not give a clear ideal ROI width, it is recommended to extend the ROI to include small margins to the sides of the mouse. This configuration was used for the overall accuracy measurements and showed relatively little variation. ROIs with widths that are smaller than the mouse or are much larger than it result in the highest errors for this method. When the full width of the mouse is not included in the ROI we can expect some degradation of accuracy since the volume and density of tissue being imaged (and therefore intensity values) changes for different projection angles independent of any

respiratory motion²². In human imaging the whole width of the patient is not generally included in the scan, reducing the accuracy of the intensity method relative to other methods in human cases²⁵ compared to in mice. If too wide or narrow ROIs can be reliably avoided, the use of either the Intensity or mAS method is recommended over other methods. However, when large margins to the sides of the mouse are included in the ROI, the use of the modified Amsterdam shroud method is recommended. One potential issue with the Intensity method is the dependence of the pixel values on the position of the gantry, which introduces a slowly varying component to the signal (Figure 23). The effect of gantry position is less than in humans due to the inclusion of the full width of the mouse. However, there is still a positional dependence due to different scattering properties at different angles²². A high pass filter can be used to lessen this component of the signal. However, with a sophisticated enough algorithm for automatically finding the peaks in the signal this step may not be necessary.

The respiratory signals obtained from these methods can be used for a number of imaging tasks including 4D imaging, retrospective gating, and the modified 4D imaging proposed here. Retrospective gating can be used to obtain a motionless image that can be used in dual energy CT imaging as described in Chapter 2. Peak expiration images are recommended for this purpose as little motion occurs near this phase. Minimal motion blurring around this phase would improve the visualization of contrast agents within the lungs or abdomen. Additionally, it would lessen the likelihood that the concentration of Iodine would be artificially lowered due to it being spread out over a wider area in the image.

4D imaging can also be used to assess respiratory motion for radiation treatment planning or other basic science applications, and does not require prior knowledge of the proportion of time spent in each phase. The modified 4D imaging improves the quality of the peak expiration image

without sacrificing motion information. The peak expiration image can be used to more accurately identify tumors without having to separately reconstruct a three dimensional image. Like retrospective gating, this image also removes motion blurring, theoretically improving the ability to identify tumors and other structures over three dimensional imaging. However, the effect of the reduction in motion blurring was observed to be minimal in this study. As mentioned in the methods section, the modified 4D imaging requires some prior knowledge about the fraction of time spent in motion. While variation between the mice in this study in this area was small enough not to impact these images, there may be differences between different strains of mice, the type of anesthetic used, or the health of the lungs (notably, the mice in this study had induced lung tumors which may affect their breathing patterns to some degree). Large differences in breathing patterns may also impact the respiratory signal extraction methods, particularly the modified Amsterdam shroud method, suggesting that care should be used if these methods are used for mice with qualitatively different breathing patterns to ensure they are performing as expected.

3.5 Conclusion

The aim of this chapter was to adapt several data driven 4D cone-beam CT methods designed for humans for mice and evaluate these methods for accurate 4D projection sorting. The working hypothesis of this aim was that the human data driven 4D CBCT techniques of Amsterdam Shroud, Fourier transform phase, and intensity can be translated to mice with a projection sorting error less than 5% of a breathing cycle and statistically lower projection sorting error than the previous center of mass data driven 4D CBCT method for mice. All methods tested were able to be successfully adapted to mice and had projection sorting errors of less than 5%, with modified Amsterdam Shroud and Intensity methods having the lowest errors (<2%). All newly implemented methods had statistically lower error than the previously implemented center of mass method.

Additionally, it is noted that the modified Amsterdam Shroud and Intensity methods had the least dependence on ROI size.

Chapter 4: Target volume and artifact evaluation of a new data-driven 4D CT

The Methods, Results, figures and tables and portions of the Introduction and Discussion of this chapter were reprinted from the following⁶⁶ with permission:

R. Martin and T. Pan, "Target volume and artifact evaluation of a new data-driven 4D CT", Practical Radiation Oncology (2016).

4.1 Introduction

As in small animal 4D CBCT, data driven techniques can be used to obtain the needed respiratory signal for clinical 4D CT. It was proposed in early implementations of 4D CT in the form of tracking the sum of pixels in a ROI³⁷. Later Li et al⁴⁴ proposed a method that tracked four features in the cine images whose value was expected to track with the respiratory signal: body area, lung area, air content, and lung density. As the measured respiratory signal should be the same across detectors for a given couch position, they used spatial coherence of the signals across these detectors to determine what feature was used at each couch position. Recently, Hui et al⁴⁵ expanded on this concept by adding features based on the Fourier transform of the image. As different ways of measuring the same breathing motion are expected to have similar results, they used normalized cross correlation between features to select which features are used in each location. Carnes et al maximized normalized cross correlation between images in overlapped regions of adjacent couch positions as part of their data driven algorithm⁴⁶. Xu and Zeng both utilized deformable image registration to track movement between cine images with considerable increases in the computation time^{47, 48}.

Recently the ideas of internal respiratory signals have been implemented in a product known as Smart Deviceless 4D⁴⁹ available from GE Health Care (Waukesha, WI). It uses some concepts from the Li paper including the four features they suggested and using a metric similar to spatial coherence to determine the feature or weighted combination of features to use at each couch position. They added two additional features (physical lung extent to reduce the impact of heart motion and lung body proportion to allow for more effective weighting of the other features based on anatomical position), and further post processing to minimize differences between couch positions. The purpose of this work is to compare this data driven 4D CT to an existing implementation of 4D CT in regards to the creation of internal gross tumor volumes (IGTVs), which covers all areas of the expected path of the visible tumor volume. The IGTVs are compared more directly through the contours drawn on MIP images and less directly through the evaluation of artifacts on phase images.

4.2 Methods

4.2.1 Patient selection

35 lung cancer patients who received 4D CT as part of their treatment simulation for stereotactic body radiation therapy (SBRT) were selected for this study in an approved institutional review board protocol # PA16-0500. A respiratory signal was recorded for each patient using Varian's RPM system. A variety of tumor locations and amount of tumor motion were represented while avoiding tumors that were difficult to separate from other structures on maximum intensity projection (MIP) images. Approximate tumor motion (measured distance on phase images between peak inhale and exhale), tumor location and diameter, and reported disease stage are shown in Table 10.

Table 10: Patient disease and tumor data

patient number	tumor location	reported tumor diameter (cm)	reported disease stage	approximate tumor motion (mm)
1	right lower	1.2	Ia	12
2	left lower	1.2	Ia	6
3	right lower	1.5	Ia	10
4	left lower	1.8	Ia	15
5	right middle	2	Ia	30
6	right lower	1.6	Ia	25
7	left lower	1	Ib	8
8	right upper	4	II	1
9	left lower	1.2	Ia	10
10	right upper	1.6	Ia	9
11	left upper	1.7x1.8	Ia	4
12	right upper	1	Ia	15
13	right lower	1.8	Ia	15
14	left upper	2.2	Ia	10
15	right middle	1.3x1.2	IV	4
16	right lower	1	Ia	21
17	left upper	2.3	Ia	3
18	left lower	3.6x4	IV	10
19	left lower	2.3x1.2	Ia	19
20	right upper	2.5	Ib	5
21	left upper	1.5	Ia	4
22	left lower	3x1.6	IIb	25
23	left lower	2	Ia	15
24	left lower	2.1x2.2	colon met.	25
25	left upper	3	Ib	4
26	right upper	2.4	Ia	8
27	right middle	1.4x1.9	Ia	12
28	right upper	1.1	breast met.	9
29	right upper	1.7	Ia	5
30	right lower	1.5	Ia	7
31	right upper	1.7	Ia	1
32	left lower	1.8	IV	9
33	right lower	2.8	Ia	16
34	right upper	1.9x1.5	III	1
35	let lower	1.5	IIa	5

4.2.2 4D CT images

Each patient was scanned on a GE Discovery ST with 120 kV, 100 mA, and 0.5 second rotations. In the implementation of 4D CT used in this chapter (cine 4D CT), the gantry is left at each couch position for approximately one respiration cycle plus one second (the couch position scan time is adjusted for each patient based on their breathing rate). An infrared reflector box was placed on the patient's abdomen and the vertical position of the box on the abdomen was recorded to obtain the respiratory signal. End-inspiration peaks were identified and used to assign phases to each of the cine images through linear interpolation between peaks. The cine image whose phase most closely matched each of the desired evenly spaced 10 phases was assigned to the appropriate bin. Usually, in CINE 4D CT not all cine images at each couch position are used in the final 4D CT images because there are typically more images than phases at each couch position. This condition was true for all patients in this study as the number of cine images per couch position ranged from 13 to 32 (average 22). In addition to the above RPM based image processing (which was considered "standard"), the image data was processed with the data driven 4D CT, which is summarized below.

First for each CINE image, 6 features are extracted through image processing. Body and lung contours obtained through thresholding and erosion and dilation are used as a starting point for these features. The first four of these features were proposed by Li and are as follows: the body area (number of pixels in the body contour), lung area (number of pixels in the lung contour), air content (sum of CT numbers in lung contour), and lung density (average CT number in the lung contour). Two additional features were added including the physical extent of the lung contour ("lung extension"), and the ratio of the lung area to the body area ("lung body proportion"). The lung body proportion is used to determine the approximate anatomical location of the current couch position. Each of these features, except lung body proportion, is used to make a respiratory signal at each detector row and couch position. The next step is to arrive at a single signal for each couch position.

For each feature and couch position, the correlation coefficient of comparing the signal at each detector row to the center detector row is calculated to see which features are the most stable and therefore most reliable. A subset of these features is selected and a weighted average is calculated based on the correlation coefficient and the lung body proportion resulting in a single signal for each couch position. Key aspects of the signal including the period and peak and valley locations are then extracted in the frequency domain since the internal signal is inherently noisier than an external signal. Post processing steps are performed that minimize phase differences between couch positions. Phase binning similar to standard phase binning is then applied, with some amplitude based binning adjustments made in regions with fast respiratory motion where small changes in phase lead to large amplitude changes⁶⁷. In this case, an image whose amplitude is closest to the desired amplitude is selected regardless of phase.

4.2.3 Comparison of MIP contours

To avoid contouring on each phase image, maximum intensity projection (MIP) images (3D images containing the highest voxel value across a series of images) are often used as a starting point for contouring the IGTV as they allow the physician to visualize anywhere the tumor has been over the breathing cycle^{39, 40, 68, 69}. Adjustments to the contour can be made using the individual phase images, especially when the tumor is near another structure such as the diaphragm⁴⁰. In this study, IGTV contours created on MIP images in MIM (Cleveland, OH) were used to compare the two methods of selecting images for 4D imaging. As in previous studies^{70, 71}, MIP images were used due to their importance in creating contours and to avoid the additional complexity of contouring each phase. To reduce intra-observer variation and bias in the contouring process it was made as automatic as possible. The region-growing tool available in MIM was used as a starting point. Adjustable algorithm parameters were kept the same between the data driven and standard images for each patient, but were occasionally adjusted between patients to adequately cover the tumor

and avoid other structures. Region-growing parameters and the values used for most of the patients included: upper threshold (200 HU), lower threshold (-424 HU), tendril diameter (7), amount of hole filling (medium), smoothing (smooth after finish option selected), and seed location (near the center of the tumor).

For tumors that touched the chest wall or mediastinum, these structures were manually trimmed off by a single observer from the rest of the contour with care taken to remove these structures in as similar a way as possible between the data driven and standard 4D CT images. First, contours were drawn on the standard and data driven MIP images with both MIP images visible. Both MIP images were made visible so that the same strategy for removing a particular blood vessel or other structure (e.g. what angle a cut should be made when it wasn't obvious where the tumor ended and other structure began) could be used in each image. Next the MIP images were fused, showing both contours on each image. Sections of the contour that were manually adjusted were evaluated. When the contours did not agree in these sections and the location that the cut should be made was not obvious in either image, the contours were adjusted so they matched in these sections. Taking these steps minimized the differences between the contours that arise from potentially biased manual contouring, making most of the differences be due to actual differences in the images detected by unbiased automatic contouring. As is clinically done for SBRT, IGTV contours were uniformly expanded by 5 mm to create planning target volume (PTV) contours.

The percent volume difference between the data driven 4D CT contours and standard 4D CT contours was calculated with the standard contours as the reference. The Dice similarity coefficient (DSC) was used to measure the similarity between the two volumes, the reference volume A (in this case the standard contour) and second volume B . It is defined as^{72, 73}

$$DSC(A, B) = \frac{2 \times |A \cap B|}{|A| + |B|}$$

Equation 6

A value of 1 for this metric signifies that the contours match perfectly and a value of 0.7 is generally considered good⁷⁴. Additionally, the mean surface separation and Hausdorff distance (the maximum surface separation) were calculated to relate the differences in terms more relevant to radiation treatment planning and delivery.

4.2.4 Comparison of phase images

The artifacts present in data driven and standard 4D CT were compared using a normalized cross correlation (NCC) method proposed by Cui et al⁷⁵. The method is described in detail in their paper, but will be summarized here. The basic concept of this method is that artifacts typically show up as discontinuities at couch position transitions, which decrease the cross correlation between images on either side of the couch transition. At each bed transition, the NCC is calculated between the 8th image (on an 8 x 2.5 mm detector configuration) of the previous bed position and 1st image of the next bed position and is defined as $C_{8,1}$. To minimize the effect of normal anatomical variations influencing the results, the NCC of the 7th and 8th image of the previous bed position, $C_{7,8}$, and the 1st and 2nd image of the next bed position, $C_{1,2}$ are calculated. A metric is defined that incorporates each of these correlations to compare the correlation between beds to that within beds:

$$D = \frac{1}{2}(C_{7,8} + C_{1,2}) - C_{8,1} \quad \text{Equation 7}$$

The difference of these values

$$\Delta D \equiv D_{RPM} - D_{DL} \quad \text{Equation 8}$$

is calculated at each bed transition and this difference was summed across all bed positions for each phase. Phases where the sum of ΔD is positive are assigned the value +1 (indicating data driven is “better” in regards to artifacts for that phase) and phases where the sum was negative are assigned

the value of -1 (indicating standard is “better”). For each patient, the phase scores are averaged to obtain an artifact score for that patient, with positive values favoring data driven and negative values favoring standard.

To quantify the stability in tumor size and shape during breathing, for 10 patients with auto only contouring, the tumor was contoured using the previously described region growing technique on each of the 10 phases for both methods.

While 10 CINE images are always selected for each couch position (one for each phase), it is possible to have the same CINE image be selected for multiple phases. The number of unique CINE images chosen for each couch position was therefore quantified.

4.2.5 Reproducibility

To quantify the errors introduced through the manual adjustments, the entire contouring and metric calculation process was repeated for 6 patients. The contouring was performed a total of 3 times by the same observer with at least 1 week between repetitions. Region growing parameters were kept the same for each patient, so only the manual adjustment differed.

In addition to uncertainties introduced in the manual contouring process, some variation is expected in the region growing algorithm based on the parameters selected. For 8 patients that had contours drawn automatically, each of the four parameters of interest (seed location, tendrill diameter, amount of hole filling, and lower threshold) were varied independently with at least two different values tested for each parameter per patient.

4.3 Results

4.3.1 Maximum intensity projection contours:

On average, contours drawn on MIP images derived from the data driven algorithm were $2.1 \pm 1.0\%$ smaller than contours drawn on standard MIP images. However, a non-inferiority test showed the data driven contour size was statistically at least as large as standard contours within a margin of 5% ($p=0.002$, $\delta=0.05$). A δ of 0.05 was chosen as inter-observer variations in contouring generally result in volume differences of at least 5% for lung tumors⁷⁶. Results of the percent volume difference and other metrics are summarized in Table 11. Figure 32 shows the volume differences (negative for smaller data driven contours), DSC, mean surface distance and Hausdorff distance. In most but not all cases, when differences in the shape of the contours were noticeable, there were corresponding noticeable differences in the shape of the tumor such as in Figure 33. Additionally, these observable differences in tumor shape were generally most apparent in patients with large percent volume difference. Results for the PTV and results separated into the 16 patients where only automatic contouring was used and the 19 patients that required manual adjustment are shown in Table 11. P-values reported in Table 11 are from non-inferiority tests as described above, where values less than 0.05 indicate contours for data driven 4D CT are at least as large as contours for standard 4D CT.

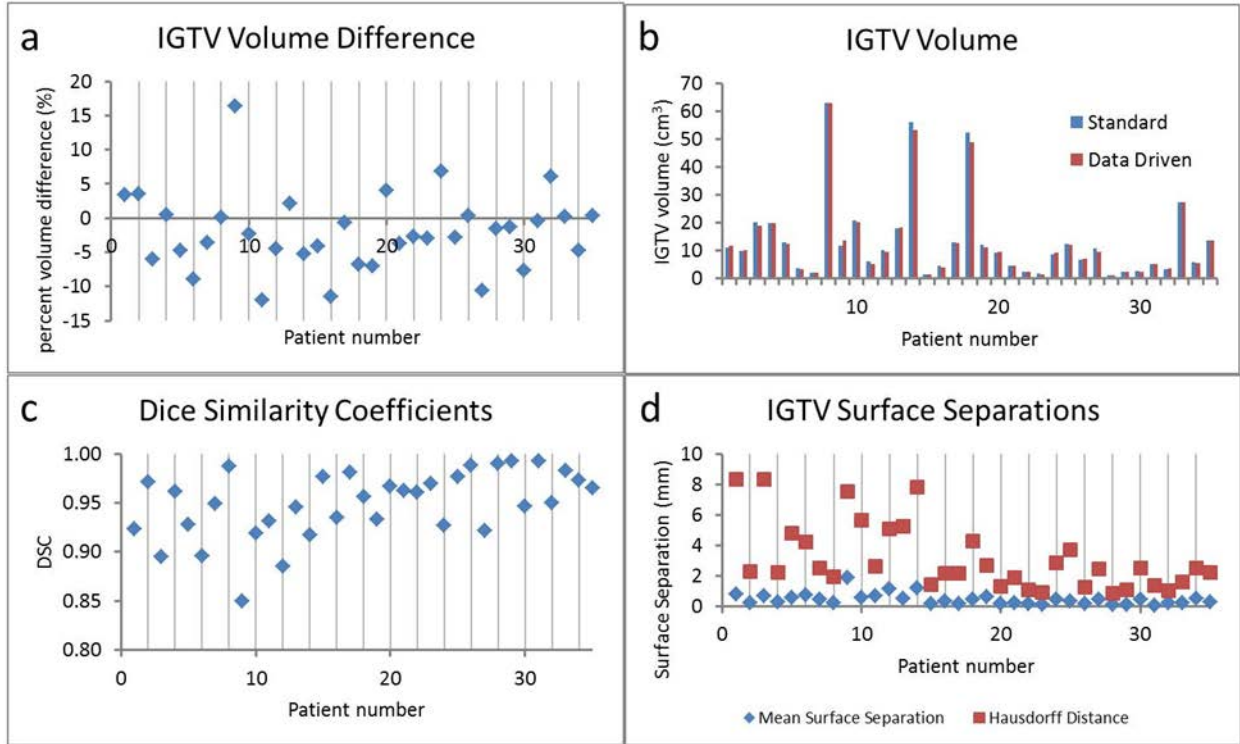


Figure 32: Comparison of IGTVs for standard and data driven method including (a) percent volume differences (negative means data driven is smaller), (b) volumes, (c) Dice Similarity coefficients, and (d) mean surface separation and Hausdorff distance (max separation)

Table 11: Contour comparison metrics

	Percent volume difference (%)	Dice Similarity Coefficient	Hausdorff Distance (mm)	Mean surface separation (mm)
All contours (IGTV)	-2.1 ± 1.0 ($p=0.002$)	0.949 ± 0.006	3.1 ± 0.4	0.44 ± 0.06
Fully automatic contours (IGTV)	-2.8 ± 1.4 ($p=2.2 \times 10^{-5}$)	0.957 ± 0.006	2.0 ± 0.3	0.31 ± 0.05
Manually adjusted contours (IGTV)	-1.4 ± 1.3 ($p=3.3 \times 10^{-5}$)	0.941 ± 0.010	4.2 ± 0.6	0.56 ± 0.11
All contours (PTV)	-1.2 ± 0.7 ($p=1.0 \times 10^{-10}$)	0.967 ± 0.004	3.0 ± 0.3	0.38 ± 0.04
Fully automatic contours (PTV)	-2.0 ± 1.0 ($p=9.8 \times 10^{-7}$)	0.973 ± 0.004	2.1 ± 0.2	0.33 ± 0.06
Manually adjusted contours (PTV)	-0.5 ± 1.1 ($p=2.1 \times 10^{-5}$)	0.961 ± 0.006	3.8 ± 0.5	0.43 ± 0.05

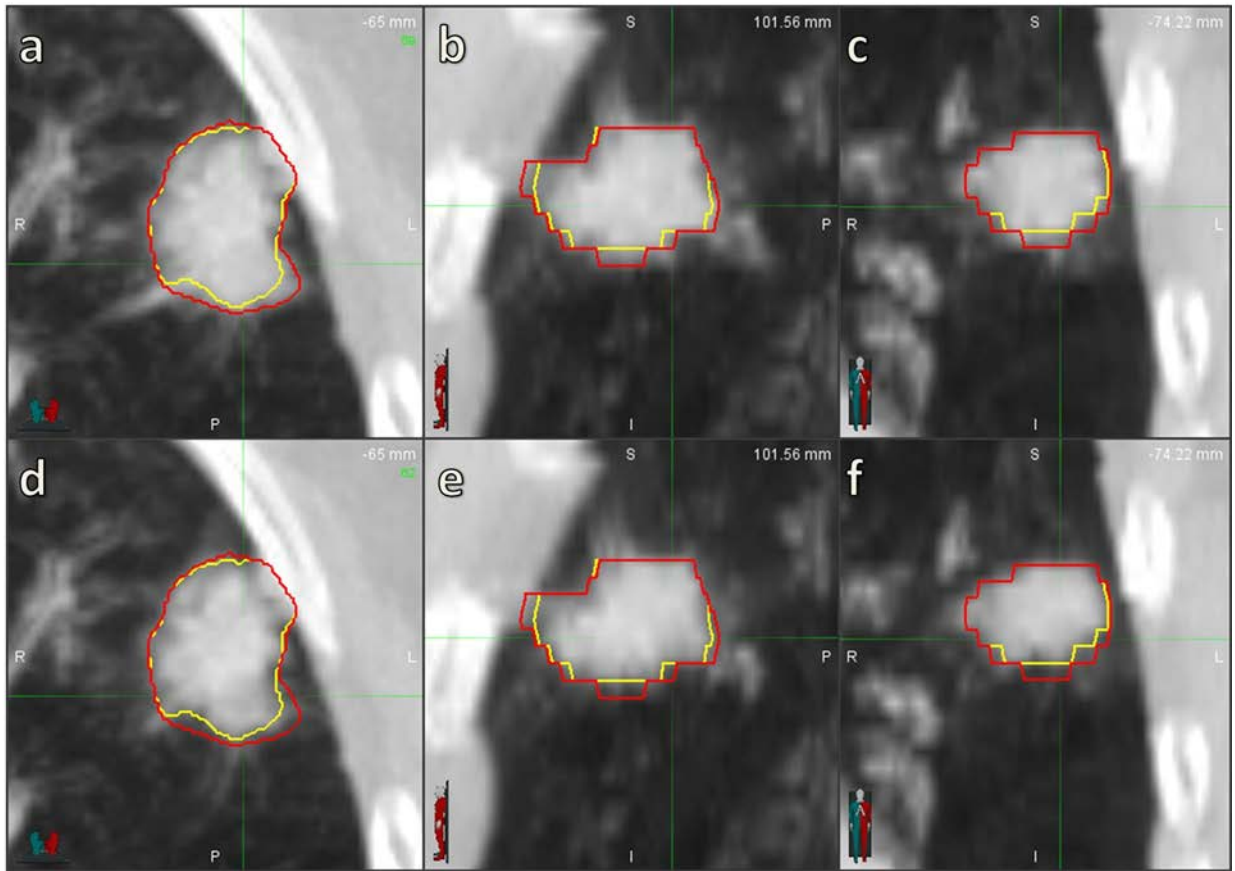


Figure 33: Axial, sagittal, and coronal (left to right) slices of standard (above) and data driven (below) MIP images for a case (patient 11) with large percent volume difference (-12.1%). The standard contour is shown in red and data driven contour in yellow, both copied to the opposite image for direct comparison. In this patient, the differences in the contours reflect the visible differences in the tumor shape.

4.3.2 Phase image comparison:

According to the automated NCC based method, most patients had fewer artifacts using the data driven method (positive artifact score) with only three patients showing better artifacts with the standard method (negative artifact score). The average patient artifact score was 0.37 which statistically differed from zero, which would indicate no difference ($p = 1.5e-5$, paired t-test). Figure 34 shows the artifact scores for all patients. Figure 35 shows patients with artifact scores of +1 and -

1. As demonstrated in this figure, in some cases the differences in artifacts as measured by the artifact score are readily apparent, while others are not obvious to a human observer.

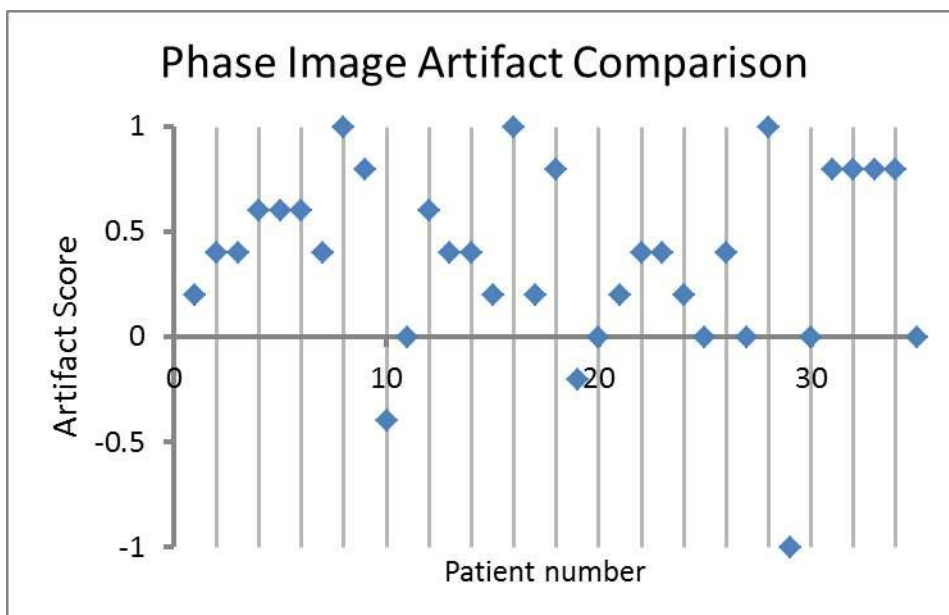


Figure 34: Artifact scores for all patients. Positive values indicate the data driven algorithm produced phase images with fewer and/or less severe artifacts, while negative values indicate the standard method is better.

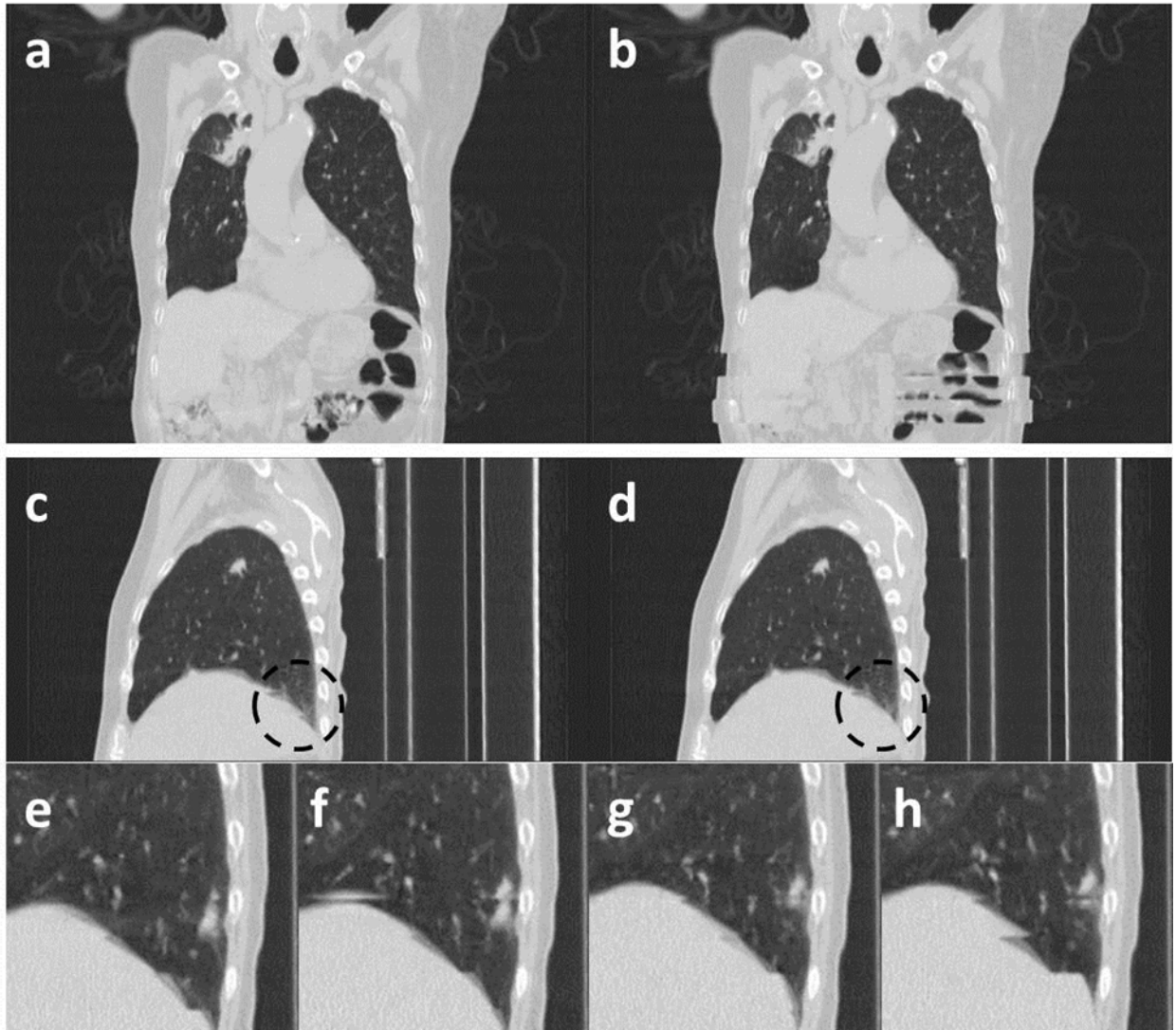


Figure 35: Data driven (a, c, and e and g) and standard (b, d, and f and h) phase images for patients (#8, #26, and #6) with artifact scores of +1, -1, and 0.6, respectively. Reduced artifacts are observed in the abdomen and diaphragm/tumor in patients 8 and 6, respectively. In patient 29, the difference in artifacts is not as visible but some improvement in artifacts with the standard method is observed in the circled region.

No statistical difference was observed between the variation in tumor volume between phase images for the same method (standard deviation/average) or phase-to-phase DSC (average DSC between adjacent phases after rigid registration to account for breathing motion) for the two methods (volume variation: 13.5 for standard vs. 13.1 for data driven, $p=0.9$; DSC: 0.879 for

standard vs. 0.882 for data driven, $p=0.9$). Large differences in these metrics were observed, however, when artifacts were present at tumor level (4 of the 10 patients, including one rare case with more artifacts in the data driven image). Comparing phase images between standard and data driven, the average percent volume change was 13.2% ($p=0.96$), and DSC was 0.77. The difference in the number of unique CINE images used to create the 10 phases images was significant, with the data driven method using fewer (9.2 vs 9.9, $p = 3e-42$ by Wilcoxon signed rank).

4.3.3 Reproducibility

For each patient where the manual contouring process was repeated, the standard deviation of each metric for the three different contours was calculated. The average standard deviation was 1.2% for percent volume difference, 0.005 for DSC, 0.1 mm for mean surface distance, and 1.1 mm for Hausdorff distance.

For the region growing algorithm, the average standard deviation for all parameter variations was 1.9 percent for percent volume difference, 0.011 for DSC, 0.1 mm for mean surface distance, and 0.5 mm for Hausdorff distance. Some large differences were observed, especially when blood vessels that could be included to varying degrees were near the tumor, including a change in percent volume difference from -5.2% to 5.4% by changing the tendril diameter in one patient.

4.4 Discussion

No significant difference between MIP images created using the data driven and standard 4D CT methods was observed in this study. The usually small differences observed were reduced when the IGTV was expanded to a PTV and can be attributed in part to sensitivity to region growing parameters and intra observer variations in manual contouring. While not having contours drawn by a radiation oncologist is in some ways a limitation of this study, the mostly automatic method

reduces the effects of intra and inter observer variations. Larger differences than observed in this study are often seen even if the same image is used due to inter-observer variations in contouring⁷⁷. Not all tumor types were directly tested due to the attempt to minimize manual contouring. However, the data driven method does not directly rely on tumor shape or location and therefore results are not expected to differ, except perhaps in highly diseased lungs where the impact on the lung contour is greater. In practice phase images are often included in the process of creating the final IGTV, either through manual adjustments to MIP generated contours or using deformable image registration (DIR) based contour propagation. A limitation of this study is that it does not directly include this aspect of the target definition process. However, the demonstrated reduction in phase image artifacts by the data driven method suggest that, if anything, the phase image contour adjusting process and DIR based propagation would be more accurate with this method.

Despite small average differences in contours, some individual patients showed larger differences (>10% volume difference, <0.9 DSC, >5 mm Hausdorff distance, and/or >1 mm mean surface separation) that warrant further investigation. Reviewing these patients, most fell under one of two categories. In some cases, many surrounding blood vessels and/or little contrast between the tumor and surrounding lung made the region growing algorithm sensitive to small changes in the image, occasionally resulting in part of a blood vessel being included in one image but not the other. Another situation that was seen in a number of cases, was prominent artifacts appearing in the phase images at the level of the tumor. Especially when the tumor was small and mobile, differences in the amount or severity of artifacts were seen to have a noticeable impact on the shape of the tumor in MIP images. As expected due to the artifact analysis, most of these cases had more artifacts in the standard images. As an example, Figure 36 shows artifacts in the standard image resulting in the tumor being visible at two couch positions in the 10%-30% phases which fills out the middle section of the standard MIP image and makes the standard IGTV larger.

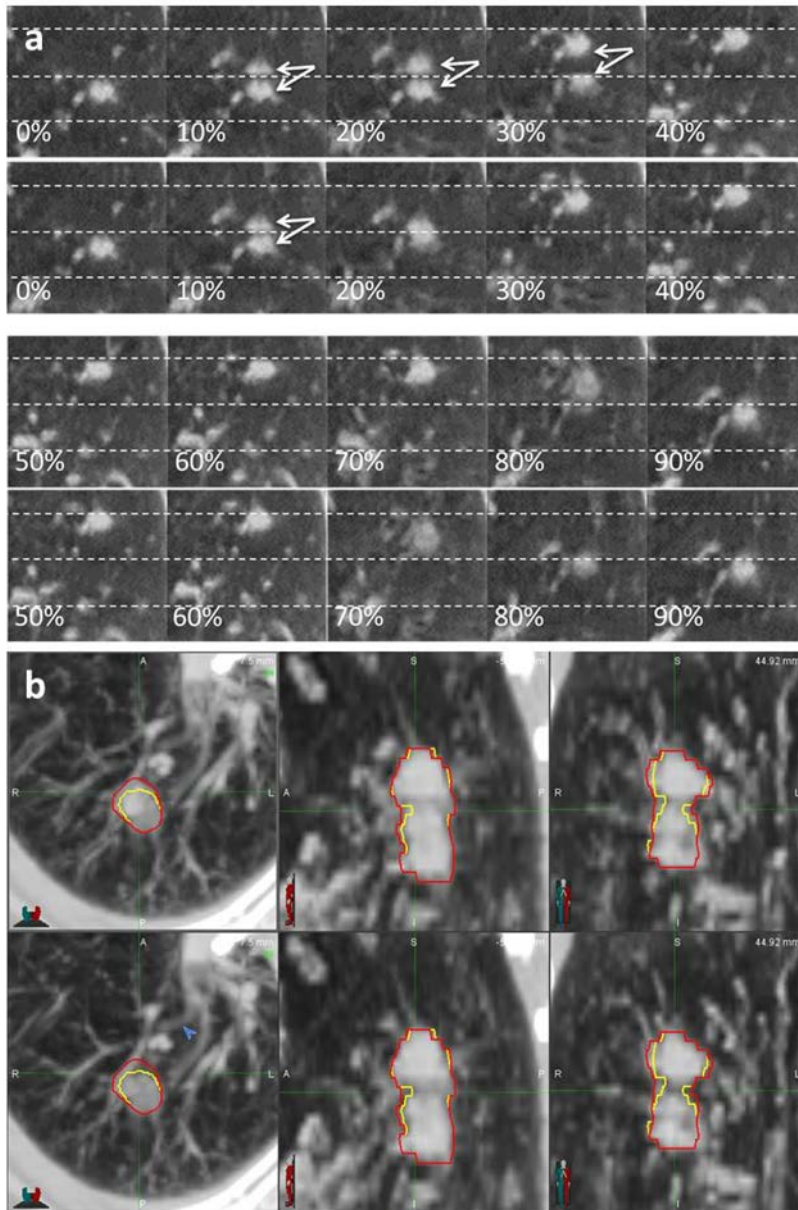


Figure 36: (a) Phase images for standard (upper rows) and data driven (bottom rows) methods for patient 16. Dotted lines show couch position transitions. Artifacts (arrows) in 10%-30% phases for the standard method contribute to a wider center region of the IGTV as shown in (b). (b) shows axial, sagittal, and coronal (left to right) slices of standard (above) and data driven (below) MIP for the same patient. The standard contour is shown in red and data driven contour in yellow, both copied to the opposite image for direct comparison.

As mentioned in the introduction, several studies⁴¹⁻⁴³ show that external motion surrogates are not always well correlated with internal motion, which is closer to target motion. The data driven algorithm relies more on internal information than an external surrogate and determines the signal locally, by couch position. The reliance on local internal motion surrogates helps to minimize the large differences in internal phase between couch positions that contribute to artifacts. Post processing steps, especially relying on amplitude based sorting when large changes in amplitude are detected, additionally help to minimize artifacts. Previous studies of similar data driven methods have shown poor correlation between data driven respiratory signals and RPM when irregular motion was present, and fewer artifacts in data driven images in these cases^{44, 45}. While respiratory signals were not directly compared in this study, the advantage of internal motion surrogates was realized by the reduction in artifacts observed through the normalized cross correlation method of evaluating the artifacts.

In the creation of IGTVs from MIP images, larger contour volumes are considered advantageous⁷⁰ as more of the tumor motion present during the scan is included. What results is a more conservative estimate of the motion that might be present during treatment and not necessarily an accurate representation of the average motion envelope. While data driven method's tendency to minimize differences between neighboring couch positions results in fewer artifacts, it can sometimes (as in Figure 36) lead to a smaller, less conservative, IGTV. Additionally, the use of fewer unique CINE images by the data driven method can lead to smaller IGTVs. That fewer unique images are used is a result of the data driven algorithm using amplitude based binning in cases of irregular motion, and selecting the closest to desired amplitude regardless of whether the CINE image is used for another phase. A check within the amplitude based binning adjustment to avoid previously chosen images may be beneficial in maximizing volume while still reducing artifacts.

The results of this study have shown that the data driven and standard 4D CT produce effectively the same IGTVs. Several advantages of data driven methods exist which suggest a benefit in adopting this technique over standard techniques, including a decrease in image artifacts which can improve quantification of tumor motion and fine adjustments made to IGTVs. Additionally, not having to set up an external motion surrogate on the patient saves some time and reduces the chance of human error. While this study focused on lung tumors, patients with tumors in the liver may also benefit, but the performance of the data driven method in the abdomen requires further investigation.

4.5 Conclusion

The aim of this chapter was to compare a commercially available data driven 4D CT algorithm to existing standard methods in regards to severity of artifacts and internal gross tumor volume. The working hypothesis for this aim was that data driven 4D CT will result in a statistically significant reduction of artifacts and statistically equivalent target volumes compared to standard 4D CT. As proposed in the hypothesis, data driven 4D CT had statistically equivalent target volumes and significantly reduced artifacts.

Chapter 5: Iterative volume of interest based 4D cone-beam CT

5.1 Introduction

As described in the previous chapter, 4D CT is often used to quantify the amount of motion prior to radiation treatment and/or determine a target, known as the internal target volume (ITV), which includes the full motion trajectory. However, the tumor motion trajectory does not necessarily stay constant over the course of the treatment, making ITVs inaccurate and potentially nullifying treatment approach decisions that were based on the amount of motion.

Cone-beam CT (CBCT) attached to the linac gantry is increasingly being employed as part of image guided radiation therapy (IGRT) as it provides 3D information useful for alignment⁷⁸⁻⁸⁰. Respiration correlated CBCT or 4D CBCT has been introduced to provide information on tumor position over time on the treatment couch⁸¹⁻⁸³. 4D CBCT can provide quantitative information on the tumor trajectory^{84, 85} to monitor for any large changes. Even without quantifying the tumor motion, 4D CBCT can be used to visually ensure that the whole tumor remains within the planning target volume (PTV) for the entire respiratory cycle.

4D CBCT has suffered from a number of drawbacks, however, that have limited its clinical application. The small number of radiographic projections that remain after dividing the projections into phases and the gaps in gantry angle between the neighboring respiratory cycles for the same phase result in heavy streak artifacts. These artifacts can be lessened by increasing the length of the scan. The current limited clinical application of 4D CBCT has taken this approach, with scan times of 4 minutes or longer^{83, 86}. However, while these scan times may be

acceptable in stereotactic body radiation therapy (SBRT) and similar treatments, they are not likely to fit in with the workflow of standard fractionation treatments, especially in busy clinics. Additionally, the extra scan time adds to the imaging dose if image SNR is to be maintained.

Another approach presented in literature is to abandon the traditional filtered back projection based Feldkamp-David-Kress (FDK) reconstruction and use reconstructions that can make the most use of the limited radiographic projection data. Iterative approaches such as the algebraic reconstruction technique (ART), iteratively solve the matrix equation that describes the transformation from object to projection image. Another category of approaches is optimization based techniques. Generally a data error term is minimized often along with another quantity such as total variation to reduce noise or other unwanted image features. More recently, compressed sensing techniques have gained popularity as the theory became better understood. Compressed sensing addresses the problem of insufficient data by promoting sparse solutions while constraining the solution to maintain a desired level of data fidelity.⁸⁷ While most medical images are not themselves sparse, there often exists a transformation, such as the image spatial derivative, that is sparse and this transformation is used in the compressed sensing algorithm. Some well-known CBCT reconstructions that use the principles of compressive sensing are ASD-POCS^{88, 89}, which uses adaptive steepest descent technique to solve a constrained minimization problem involving total variation, and prior image constrained compressed sensing (PICCS)^{90, 91}, which includes a comparison to a prior image.

Despite the availability of literature on advanced reconstruction techniques and the image quality benefits they provide, they have not found widespread use in the clinic. Computation time is an important consideration with IGRT techniques as images generally need to be reconstructed while the patient is on the treatment couch waiting for treatment or even in

real-time during treatment. Many advanced CBCT reconstruction algorithms, however, suffer from long computation times. For example, Bergner et al⁹² reports an increase in computational load for ASD-POCS and PICCS of 4800 and 72 times, respectively, over FDK. Additionally, some detail may be lost with these techniques, especially if the various algorithm parameters are not carefully chosen, due to assumptions such as piece-wise image constancy.

To address the problem of heavy streak artifacts in 4D CBCT while keeping image acquisition and computation times low, the authors propose an iterative volume of interest based (I4D VOI) reconstruction. This method builds off the proposal of Ahmad et al³⁵ which we will call FDK VOI. In Ahmad's paper, all projections are used to first create a 3D image. Next the projections are divided into phases and used for a 4D reconstruction exclusively performed within a volume of interest (VOI) around the tumor. Each phase image then includes the 3D background and phase specific VOI. This approach reduces streak artifacts outside the VOI, allowing for it to be used for initial bony anatomy alignment, while providing tumor motion information within the VOI. FDK reconstructions were used in Ahmad's proposal. However, the approach used there can be applied to other reconstruction types. Using an iterative reconstruction method with this approach is the focus of this work. This reconstruction was first proposed in Ahmad's dissertation where it was tested on 4 patients and in a numerical phantom⁹³. The phantom study showed improvements in RMS error of reconstructed voxel values over FDK VOI, providing motivation for further testing of I4D VOI. This work tests I4D VOI on a larger patient data set to see if the benefits of I4D VOI over FDK VOI are observed in patients and compares the VOI approach to an unconstrained total variation minimization technique.

5.2 Methods

5.2.1 Data acquisition

5.2.1.1 CBCT scan

14 lung cancer patients who received a long CBCT scan before one of their radiation treatments at Virginia Commonwealth University (VCU) were used in this study. A material transfer agreement was approved between VCU and our institution for data sharing. The length of the scans ranged from approximately 6.5-12 minutes resulting in approximately 2700-3500 projections per scan. Most scans were done with a single rotation with one patient being scanned with two rotations. The detector was offset by 14.8 cm to increase the field of view. Projection images had a dimension of 512x384 (2x2 binning from the original 1024x768 detector elements). Reconstructed images were 256x256x128 in dimension and had a field of view of 450 mm and height of 225 mm. Patient demographic information is included in Table 12. Further information on these patients and the CBCT scans can be obtained in Hugo et al's paper describing this data set⁹⁴. Patient numbers included in this chapter are the same as in Hugo's publication.

Table 12: Patient demographic information (*measured from fully sampled FDK)

Patient number	sex	age	weight	tumor volume (cc)	tumor location	peak-to-peak SI tumor motion (mm)*	breathing period (s)	irregular breathing?
100	M	66	170	75	RUL	6.5	4.4	
101	F	51	148	27	RUL	5.4	3.7	
102	M	62	194	171	LUL	0.9	2.6	yes
103	M	57	191	58	RUL	3.9	3.1	
104	M	69	206	47	LLL	6.3	3.2	yes
105	F	52	147	33	LLL	13.1	3.1	
106	F	53	234	143	mediastinum	4.0	3.3	
107	F	55	176	18	LUL	3.9	3.0	yes
108	F	61	138	12	RUL	0.8	4.3	yes
110	M	67	203	55	RLL	10.1	8.1	
111	M	59	185	75	RLL	7.8	3.8	
112	F	58	134	31	RUL	0.4	3.5	
114	M	52	156	179	RLL	3.8	3.3	
115	M	65	181	7	RUL	4.6	5.0	

5.2.1.2 RPM respiratory signal

While the patient was being scanned, their respiratory signal was tracked using Varian's real-time position management (RPM) system. An infrared reflector block was placed on the patient's abdomen and its vertical movement was tracked via an infrared camera. Timestamps allowed projection and RPM data to be correlated with CT data, which allowed for the sorting of the projections based on the respiratory data. Peaks of the respiratory signal were identified and used to sort the projections into 8 equally spaced phase bins.

5.2.1.3 Projection reduction method and gold standard

While the long scan times used in this study reduce artifacts common to 4D CBCT and are useful as a gold standard, they are not practical clinically. To mimic shorter scans while still using the same data set, a fraction of the respiratory cycles were removed. For example, for a

reduction factor of 2, projections from every other respiratory cycle were not included. Data was removed in a respiratory cycle basis as opposed to by projections to more closely simulate the projection angular spacing of a patient had they undergone a shorter scan versus a longer one. The reduction factor was selected such that the simulated scan time was as close to 2 minutes as possible. For 3D images (used in VOI based reconstructions as described in Section 5.2.2), the breathing cycles were ignored when projections were being removed. Instead, every 2nd or 3rd projection was kept (for a reduction factor of 2 or 3, respectively, for example). This reduction strategy more closely mimicked the even projection spacing that is expected in a real 2 minute 3D scan.

In this study, the full length scan was used as a gold standard while the 2 minute scans were used to compare the different reconstruction methods. FDK reconstructions (described in the next section) using all projection images from these long scans are essentially lacking in streak artifacts. These images, therefore, became the reference both visually for what structures should be visible, and quantitatively for the amount of tumor motion present. This reconstruction will be referred to as “fully sampled FDK” for the remainder of the chapter.

5.2.2 Reconstructions

5.2.2.1 I4D VOI reconstruction

For the proposed iterative 4D volume of interest (I4D VOI) reconstruction, the linear system of equations $\vec{A}_n \cdot \vec{x} = b_n$ for $n = 1, 2, \dots, N$ is solved iteratively for \vec{x} . In these equations, b_n is the n^{th} projection measurement, \vec{A}_n is the projection operator for the n^{th} projection, \vec{x} is the imaged object at the current phase, and N is the total number of projection measurements. The algebraic reconstruction technique (ART) is used to solve these equations. In this method an

updated estimate of the image, $\vec{x}^{(k+1)}$, is calculated from the previous image estimate, \vec{x}^k , by the equation:

$$\vec{x}^{(k+1)} = \vec{x}^{(k)} - \beta (\vec{A}_n \cdot \vec{x} - b_n) \frac{\vec{A}_n}{\sum_m A_{n,m}^2} \quad \text{Equation 9}$$

where β is a relaxation parameter used to minimize the effect of projection noise or system modeling inaccuracies. The value of β can range from 0 to 1 and was set to 0.1 in this study. In this form of the algorithm, the update is applied sequentially for all N projection data, but it can be modified to update in parallel using a graphics processing unit (GPU) for all or a subset of the projection data. To reduce computation time, this simultaneous iterative reconstruction technique (SIRT) is used for this study. In SIRT, a subset, S_i , of the total projection data, b_n , is used. In this implementation, the subset is a single cone beam projection image. The update equation for SIRT is given by:

$$\vec{x}^{(k+1)} = \vec{x}^{(k)} - \beta \left[\sum_{n \in S_i} \left[(\vec{A}_n \cdot \vec{x} - b_n) \frac{\vec{A}_n}{\sum_m A_{n,m}^2} \right] \right] ./ \vec{\ell}_{S_i} \quad \text{Equation 10}$$

where $./$ is element-by-element division and $\vec{\ell}_{S_i}$ normalizes the update by the sum of weights for each image voxel for subset S_i . It is expressed as:

$$\vec{\ell}_{S_i} = \{\ell_m\}, \quad m = 1, 2, \dots, M$$

$$\ell_m = \sum_{n \in S_i} A_{n,m} \quad \text{Equation 11}$$

In the proposed reconstruction, all projections are used to form a 3D image. Next the projections are sorted by phase as previously discussed and a VOI is selected. The proposed size of the VOI is the planning target volume (PTV). Since planning images were not available, an approximate PTV was drawn and used as the VOI in this study. Next the SIRT algorithm is used to update *only the region within the VOI* for each phase. Mathematically this is represented by a

masking operation with mask M which is 1 inside the VOI and 0 elsewhere. The update equation becomes:

$$\vec{x}^{(k+1)} = \vec{x}^{(k)} - \beta \left[\sum_{n \in S_i} \left[(\vec{A}_n \cdot \vec{x} - b_n) \frac{\vec{A}_n \cdot \vec{M}}{\sum_m A_{n,m}^2} \right] \right] \cdot \vec{\ell}_{S_i} \quad \text{Equation 12}$$

where $\cdot *$ represents element-by-element multiplication. To further reduce computation time, projection rays that do not intersect the VOI, so that $\vec{A}_n \cdot \vec{M} = 0$, are omitted from the summation. The expression $\vec{A}_n \cdot \vec{M}$ was pre-computed to determine what terms in the summation are needed and what can be ignored. The number of iterations used in this study for this reconstruction was 50 as the algorithm was found to converge by this point.

This reconstruction uses an initial guess for the first iteration. For the 3D image, this initial guess was simply an array of zeros, but for the phase images, this initial guess was the 3D image used as the background in this reconstruction.

In theory, FDK could be used to reconstruct the 3D image used in this method. The faster computation time of FDK would assist in keeping the computation time clinically feasible (see Section 5.3.4). Voxel intensity differences between our implementations of FDK and SIRT reconstructions, however, made the use of FDK as an initial guess for SIRT not feasible. Instead, SIRT was used for the 3D images in this chapter. If proper calibration is implemented such that these intensity differences are minimized, FDK is recommended for the 3D image.

As shown in Figure 37, brighter or darker voxels along the border of the VOI are relatively common with this technique, especially for tumors near other structures like the one in Figure 37. To minimize the effect of these border artifacts, two additional steps are taken. Firstly, prior to reconstruction, the mask is expanded isotropically by two voxels (3.5 mm) using image dilation. Once the reconstruction is completed using this mask, only the area within the

original VOI is maintained as 4D, while the rest of expanded VOI is filled in with the 3D image. This process effectively trims off two voxels around the border while still using the original VOI size in the final reconstruction. Secondly, a Gaussian smoothing filter ($\sigma = 0.5$, $3 \times 3 \times 3$ filter size) is applied to the voxels on either side of the border. The effect on the image of these steps is shown in Figure 37.

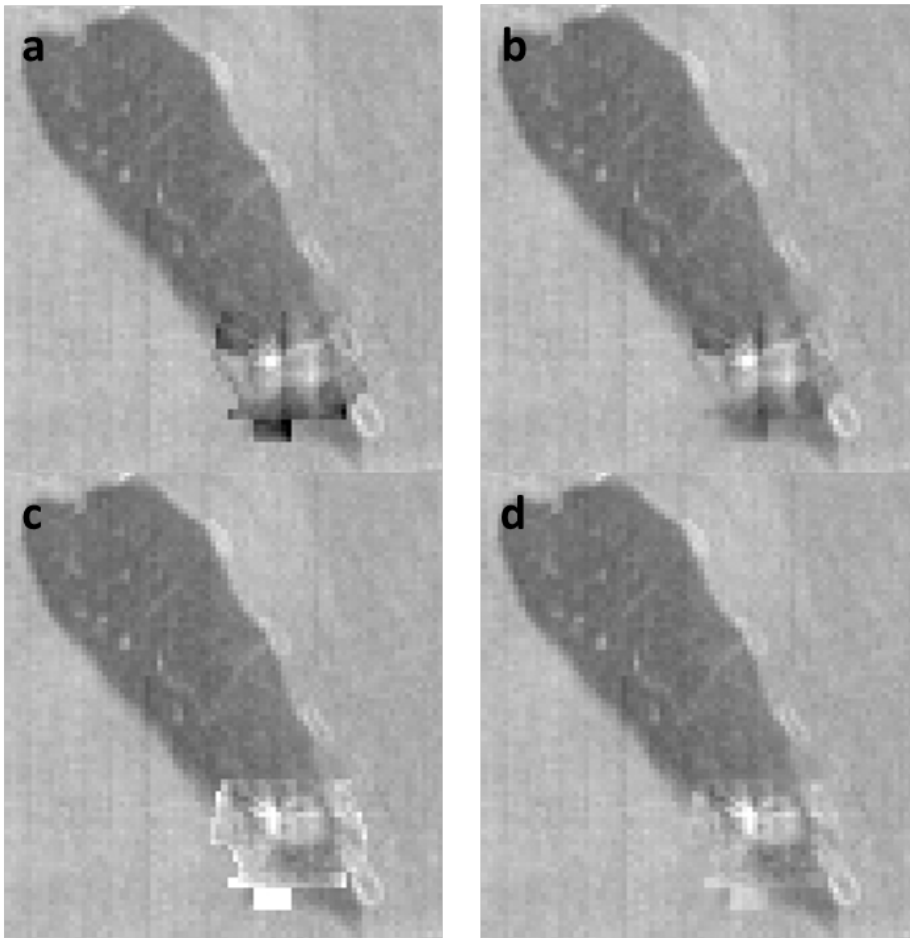


Figure 37: Iterative 4D volume of interest (I4D VOI) images of peak inhale (a and b) and exhale (c and d) for a patient discontinuities at the edges are obvious without correction (a and c). These discontinuities become less noticeable by removing two voxels isotropically around the border (after reconstructing with a VOI expanded by two voxels) and smoothing the border voxels (b and d). Note that the bright area in the center of the VOI is present

5.2.2.2 FDK reconstruction

A standard filtered back projection for CBCT, known as Feldkamp-David-Kress (FDK)⁵⁶, was done using all projections for each patient. This image became the gold standard when evaluating motion tracking as described in Section 5.2.3 and will be referred to as fully sampled FDK for the remainder of this chapter. In addition, a simulated 2-minute FDK image was also reconstructed to compare to the I4D VOI method. For each FDK reconstruction, a Butterworth filter of order 5 was used with a frequency cut-off of 0.3 of Nyquist frequency (to approximate the SNR of a typical clinical 3D CBCT with FDK reconstruction). Since post-reconstruction smoothing is one method of reducing the impact of streak artifacts (with some loss of spatial resolution), we included an FDK reconstruction with Gaussian smoothing ($\sigma=0.5$ voxel, 3x3 filter) in our evaluation. This reconstruction will be referred to as Smooth FDK.

5.2.2.3 FDK VOI reconstruction

Similar to I4D VOI, FDK VOI reconstructions were performed using the method described by Ahmad et al³⁵. In this case, the 4D VOIs were taken from complete FDK phase images and were added to 3D FDK images. In Smooth FDK VOI reconstructions, Gaussian smoothing was added to the 4D phase images as described in the previous section. No Gaussian smoothing was added to the 3D portion of the image. Edge discontinuity correction was applied in the same manner as with I4D VOI.

5.2.2.4 Unconstrained TV minimization reconstruction

The set of equations $\vec{A}_n \cdot \vec{x} = b_n$ can also be solved using an optimization framework. In unconstrained total variation minimization, both the data error and total variation (TV) are minimized through the following equation:

$$\vec{x} = \min \left(\sum_n \|\vec{A}_n \cdot \vec{x} - b_n\|^2 + \lambda TV(\vec{x}) \right) \quad \text{Equation 13}$$

where TV is the ℓ_1 -norm of the gradient image and λ is a regularization parameter that determines the relative importance of total variation in the minimization. To minimize bias in the results from a non-ideal value of λ , two reconstructions with different values of λ representing high and low regularization were performed. To find appropriate values of λ , a range of λ values were tested on one patient as shown in Figure 38. For low regularization, $\lambda = 2$ was chosen as it largely maintained image detail while still reducing streak artifacts, and for high regularization, $\lambda = 10$ was chosen as it fully reduced streak artifacts without the increased smoothing at higher λ . A MATLAB implementation (fminlbfgs) of the large scale Broyden-Fletcher-Goldfarb-Shanno algorithm, a fast Newton gradient-descent type algorithm, was used to solve the minimization problem. The gradient was supplied to the optimizing function to further increase speed. Stopping criteria for the objective function and change in output were chosen such that the algorithm approached convergence, with visible changes in the images at subsequent iterations no longer being seen. The stopping criteria were on the order of 0.1 HU. As with all reconstructions used in this work, forward and back projection operations were performed in parallel for each projection image.

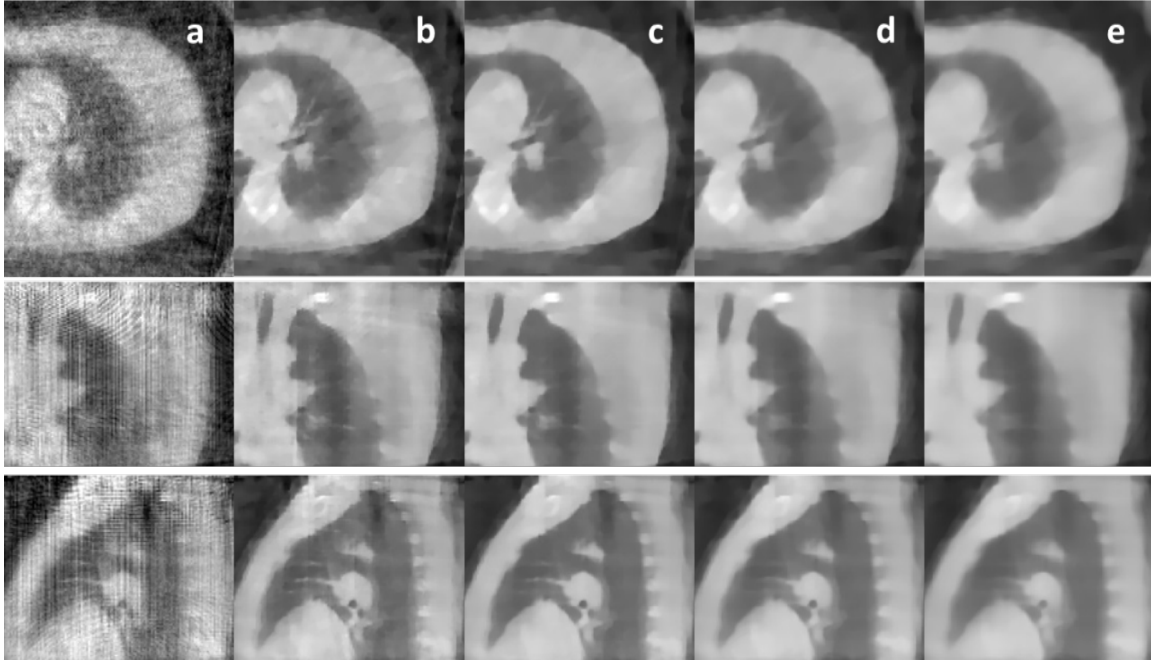


Figure 38: Axial, coronal, and sagittal (top, middle, bottom) slices of TV minimization reconstructions for varying values of λ : (a) 0, (b) 2, (c) 5, (d) 10, and (e) 20.

5.2.3 Registration technique

An intensity-based rigid registration technique was used to track the 3D motion of the tumor. Least squares minimization of the difference in voxel intensities between the test and reference images was used to determine the rigid motion. The function to be minimized was

$$\int T(\vec{r} - \vec{r}_s) - R(\vec{r}) \cdot dV \quad \text{Equation 14}$$

where $T(\vec{r})$ and $R(\vec{r})$ are the test and reference image, respectively, and \vec{r}_s is the translation shift variable. Only voxels within a VOI defined on the reference image were compared. The VOI used was the same that was used for the I4D VOI reconstruction. This rigid registration did not include rotational motion. Within the VOI, lesion rotation during respiration was assumed to be negligible. A multi-resolution strategy with 4 resolution levels was employed to reduce the likelihood of finding local minimums. It is worth noting that as the test image is shifted during

the minimization process, some test image voxels used in the comparison were within the 3D region of the image. The peak expiration image was chosen as the reference image due to motion around exhale being more stable than around peak inhale. Each phase image was registered to the peak exhale image and a displacement vector was computed for each phase. The motion trajectories were determined by tracking those displacements over the course of the respiratory cycle. A sample tumor trajectory comparison for a patient (P100) with moderate motion errors is shown in Figure 39. The motion of the fully sampled FDK reconstruction was considered ground truth and the motion of each of the other reconstructions was compared to it using a root mean square (RMS) error. The RMS error is defined as:

$$RMS = \sqrt{\frac{1}{n-1} \sum_i \left| \vec{r}_m^i - \vec{r}_t^i \right|^2} \quad \text{Equation 15}$$

where \vec{r}_m^i and \vec{r}_t^i are the measured and true (defined by gold standard) positions, respectively, of the tumor in the i^{th} phase.

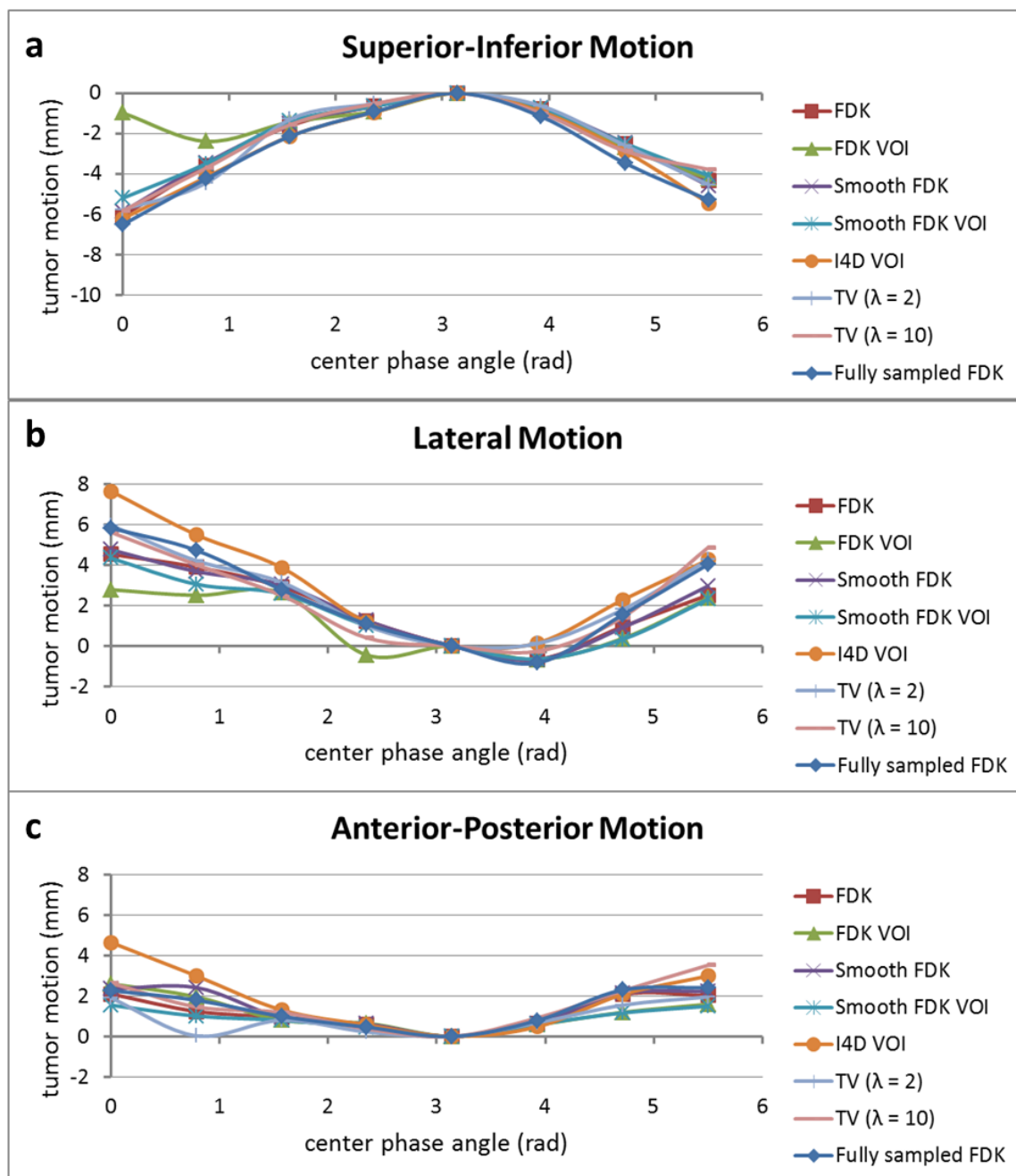


Figure 39: Superior-Inferior (a), lateral (b), and Anterior-Posterior (c) tumor trajectories for a patient (P100) with moderate agreement between the gold standard fully sampled FDK and other reconstruction methods. Tumor position for each phase is measured relative to peak exhale (phase angle = π) using rigid registration within the VOI.

5.2.4 One minute scan time reconstructions

To further explore the differences between Smooth FDK VOI and I4D VOI simulated 1 minute 4D CBCT images were reconstructed using each of these methods. As with the comparison of all reconstructions at 2 minutes, visual differences and RMS error of tumor motion compared to fully sampled FDK were used for comparison.

5.3 Results

5.3.1 Image quality

Axial, coronal and sagittal slices of each reconstruction type at peak inhale and exhale are shown in Figure 40 and Figure 41. P105 (Figure 40) represents a more difficult case for visualization of a small mobile tumor. P107 (Figure 41) represents a larger tumor with moderate motion. As expected, the FDK reconstruction contained heavy streak artifacts, increasing the difficulty of locating the tumor or visualizing bony anatomy used for alignment. The appearance of streak artifacts is somewhat mitigated by applying Gaussian smoothing. In the 3D region for both the FDK VOI and I4D VOI bony anatomy is easily visualized with minimal blurring and streak artifacts are effectively eliminated. While this image quality improvement outside the VOI does not help with visualization or tracking of the tumor, it does allow for alignment of bony anatomy to be made without having to create additional images. It is noted that outside the VOI, structures in the lung are more blurred in the VOI reconstructions than other reconstructions due to the inclusion of projections from all breathing phases by design. Since the portions of the image that can be used for alignment or tumor motion verification are only minimally affected by motion blurring, this aspect of the reconstruction is not considered a disadvantage. Inside the VOI, Smooth FDK VOI and I4D VOI have a similar appearance, with subtle differences in streak artifacts and shape of the tumor being observed (yellow arrows in Figure 41). Overall, there

appeared to be less pronounced streak artifacts and tumor boundaries that were better defined and closer to the gold standard in I4D VOI. However, these differences were small and subjective. Differences are more pronounced in patients such as P108 (Figure 44), where streak artifacts are particularly heavy in FDK reconstructions due to irregular and long breathing cycles. Due to the minimization of total variation, the TV images appear smoothed compared to the FDK and SIRT images. The amount of smoothing and presence of streak artifacts depends on the regularization parameter, λ , with low values of λ giving sharper images with more streak artifacts and higher values of λ giving smoothed out images with few, if any, streak artifacts.

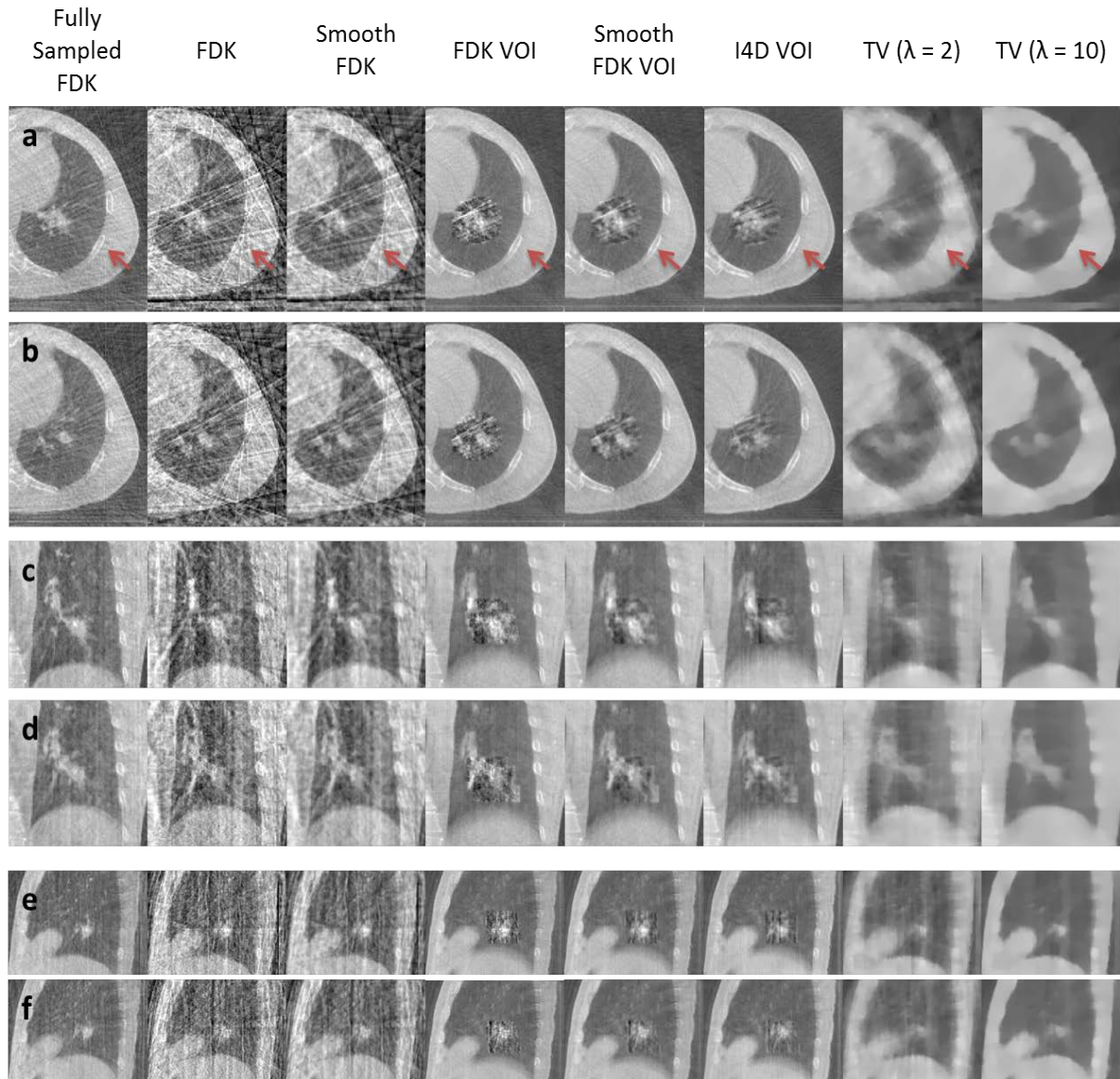


Figure 40: Axial (a, b), coronal (c, d), and sagittal (e, f) slices of peak inhale (a, c, e) and exhale (b, d, f) for each of the reconstructions (left to right): fully sampled FDK, FDK, Smooth FDK, FDK VOI, Smooth FDK VOI, I4D VOI, TV min ($\lambda=2$), and TV min ($\lambda=10$). Red arrows highlight differences in bony anatomy visualization among various reconstructions. P105 pictured here represents a difficult case of a small mobile tumor.

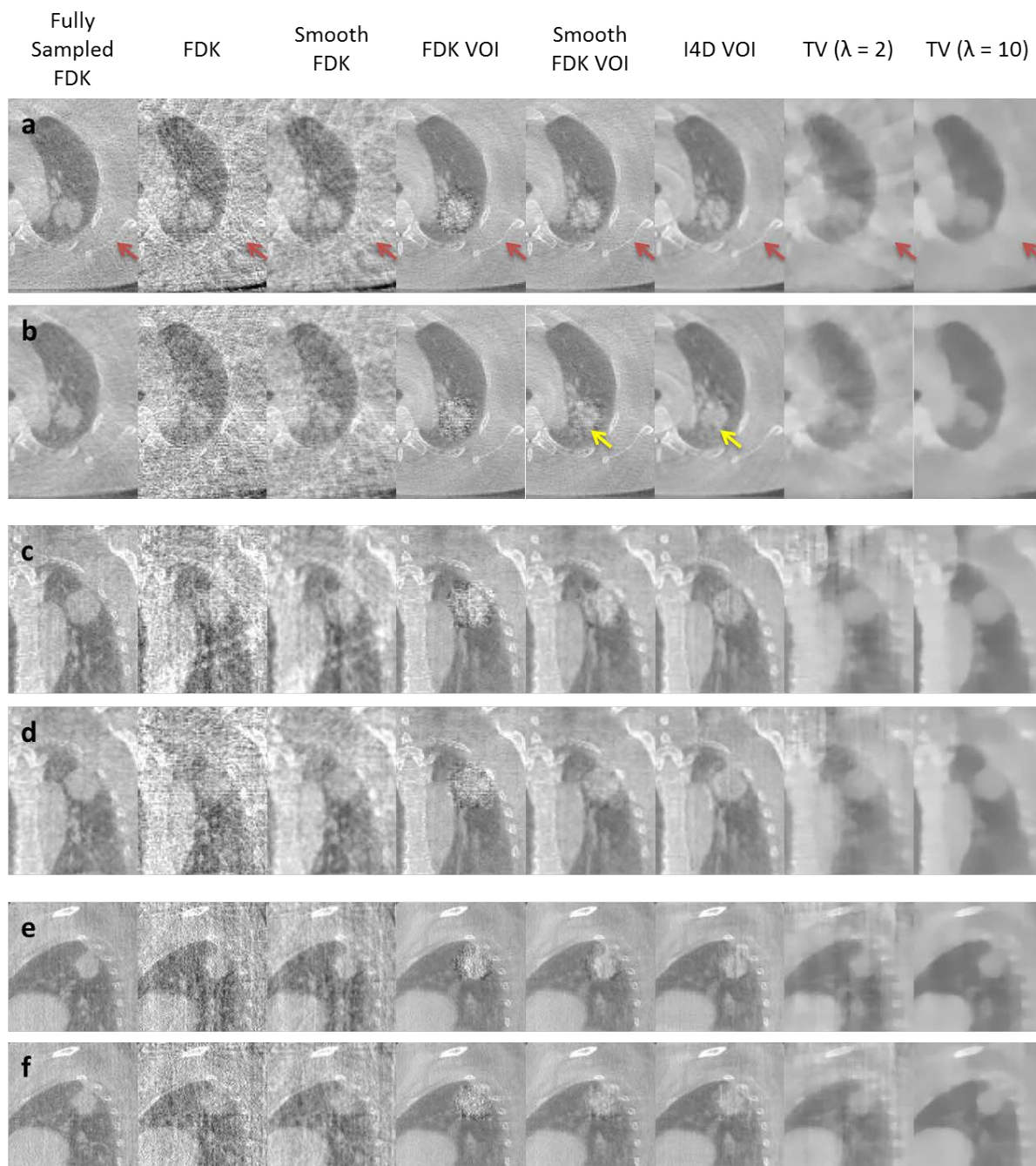


Figure 41: Axial (a, b), coronal (c, d), and sagittal (e, f) slices of peak inhale (a, c, e) and exhale (b, d, f) for each of the reconstructions (left to right): fully sampled FDK, FDK, Smooth FDK, FDK VOI, Smooth FDK VOI, I4D VOI, TV min ($\lambda=2$), and TV min ($\lambda=10$). Red arrows highlight differences in bony anatomy visualization among various reconstructions. Yellow arrows indicate differences between Smooth FDK VOI and I4D VOI. P107 pictured here represents a patient with a relatively large tumor with moderate motion.

5.3.2 Trajectory errors

In patients 110 and 115 (not listed in the results) the registration resulted in large errors (either no motion detected when there was motion or large overestimation of motion) for multiple reconstruction techniques. In these two patients it was noted that there were ring artifacts present in the VOI (these ring artifacts were a result of defective detector elements and were present in a few other patients but were outside of the VOI in these cases). The registration technique used was deemed unreliable in these cases due to these artifacts and these two patients were removed from quantitative analysis. Trajectory error measurements for the remaining patients using each method are shown in Figure 42 (a). Figure 42 (b) shows the average (standard error) RMS error for each method. P-values for paired t-test comparisons are contained in Table 13. I4D VOI had significantly less RMS error than FDK VOI prior to smoothing (1.3 vs 1.9 mm, $p=0.02$), but the difference was no longer significant after smoothing (1.3 vs. 1.4 mm, $p=0.20$). Near significant values were observed for I4D VOI's improvement over FDK before and after smoothing (1.3 vs. 1.8 mm, $p = 0.08$ and 1.3 vs. 1.5 mm, $p=0.07$, respectively). It is noted that there is little change in RMS error before and after smoothing is added for FDK, but a significant difference between FDK VOI and Smooth FDK VOI ($p=0.03$). Since FDK and FDK VOI are identical within the VOI, any difference in tumor motion measurements between these reconstructions is related to the boundary between the VOI and the background image. With smoothing, the VOI and the background are more similar in terms of noise and contrast between background lung and other anatomical structures. This improved similarity likely contributes to the observed smaller RMS errors for Smooth FDK VOI compared to FDK VOI.

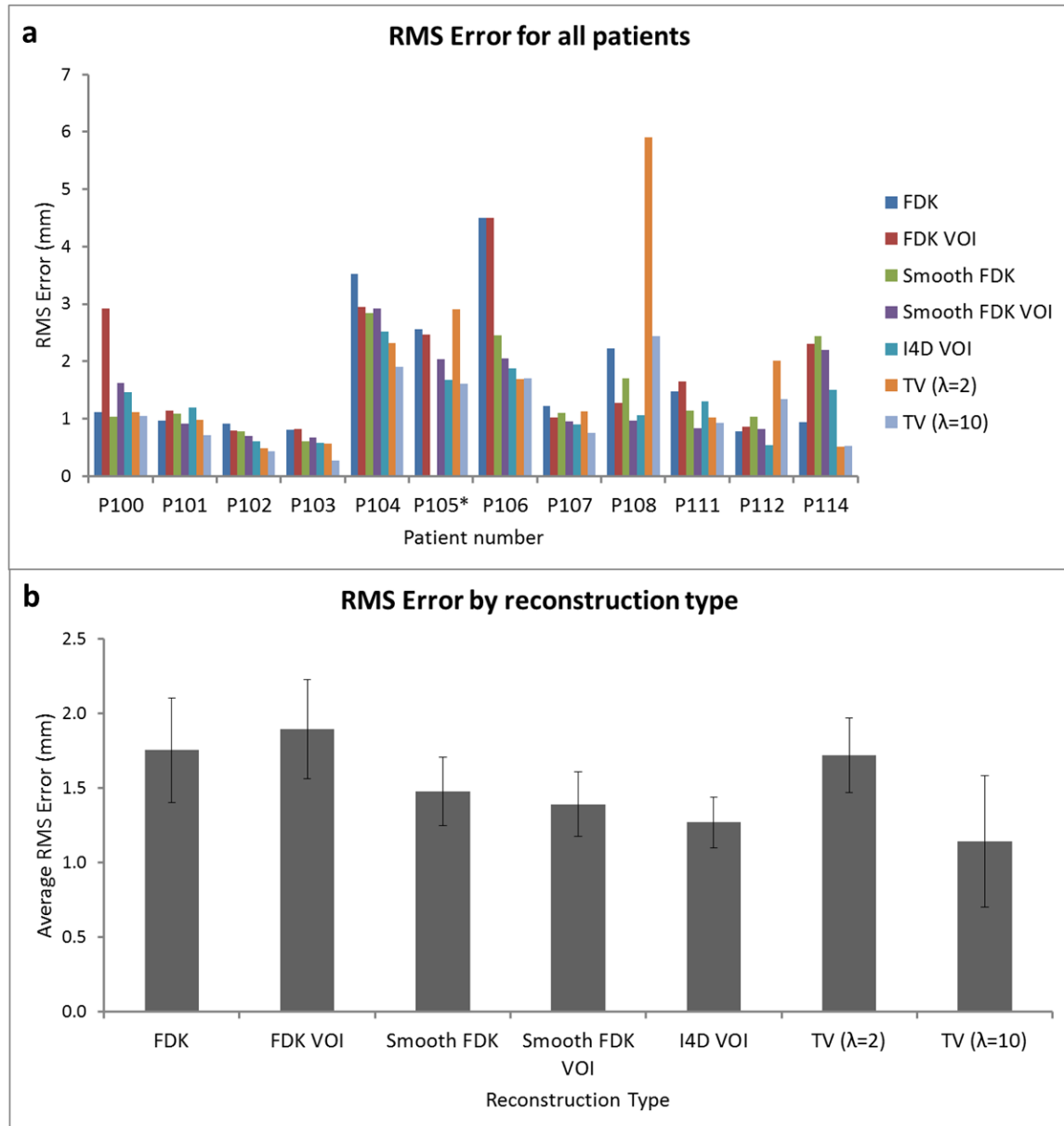


Figure 42: Tumor trajectories for a patient with good agreement between the gold standard fully sampled FDK and other reconstruction methods (a) and a patient where the registration failed to detect motion in the I4D VOI reconstruction (b). Tumor position for each phase is measured relative to peak exhale (phase angle = π) using rigid registration within the VOI. RMS errors for each reconstruction and each patient except those two where the registration failed with two or more registration types are shown in (c).

Table 13: RMS error comparison p-values

	TV min ($\lambda=10$)	TV min ($\lambda=2$)	I4D VOI	Smooth FDK VOI	Smooth FDK	Smooth FDK VOI
FDK	0.03	0.94	0.08	0.19	0.44	0.54
FDK VOI	0.03	0.76	0.02	0.03	0.17	
Smooth FDK	0.10	0.77	0.07	0.18		
Smooth FDK VOI	0.28	0.50	0.20			
I4D VOI	0.50	0.33				
TV ($\lambda=2$)	0.07					

Even when there are no significant difference in the RMS errors, as seen in Figure 42 there are some patients where there are large differences in error amongst the different reconstruction types. In some cases these differences can be attributed to the unpredictable effect of the streak artifacts. While streak artifacts are prevalent in all non-fully sampled FDK images, the exact location of these artifacts can determine whether or not a registration will perform poorly, especially if the tumor size is small. Patients 105 and 106 are examples of streak artifacts coupled with small tumor size causing errors in FDK tumor trajectory measurements (in patient 105 the registration failed to initialize after large error in the previous phase for the Smooth FDK reconstruction). While TV minimization largely reduced these artifacts, some were still present in low regularization reconstructions. In patient 108, these artifacts are more prominent with TV minimization ($\lambda=2$) reconstruction than in other patients, likely due to the irregular spacing between breathing periods observed in the respiratory signal. These artifacts and the small size of the tumor (which was partially blurred due to TV minimization) likely contributed to the higher error for this reconstruction type and patient.

5.3.3 One minute scan time

Figure 43 and Figure 44 show axial, coronal, and sagittal slices of Smooth FDK VOI and I4D VOI reconstructions for 1 and 2 minute simulated scan times compared to fully sampled

FDK. While the difference in Smooth FDK VOI and I4D VOI images is not obvious for 2 minute scans, noticeable differences are observed for 1 minute scans. Streak artifacts increase in the 1 minute Smooth FDK VOI images to the point that it is difficult to make out the tumor boundary (see especially yellow arrows and axial images in Figure 43 and Figure 44). This difficulty is especially apparent in P108 (Figure 44), which has more streak artifacts overall due to irregular breathing and a long breathing period (4.3 seconds). Streak artifacts and blurring increase somewhat in I4D VOI images for 1 minute scans, but the difference between 2 minute and 1 minute scans is less evident and tumor boundaries are still mostly visible.

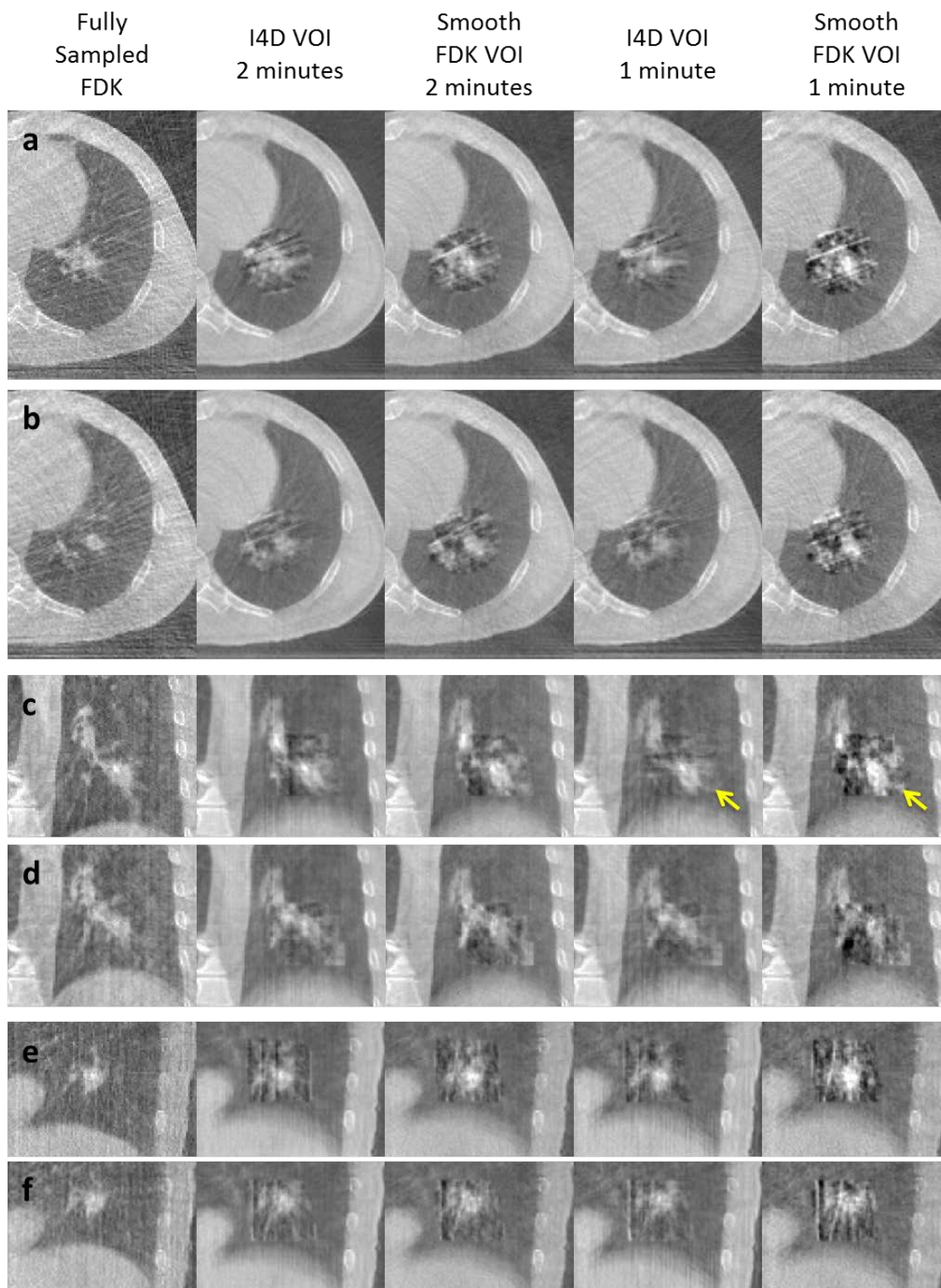


Figure 43: Axial (a, b), coronal (c, d), and sagittal (e, f) slices of peak inhale (a, c, e) and exhale (b, d, f) for 2 and 1 minute VOI reconstructions from left to right: fully sampled FDK, I4D VOI 2 minutes, Smooth FDK 2 minutes, I4D VOI 1 minute, Smooth FDK VOI 1 minute. P105 pictured here represents a difficult case of a small mobile tumor. Differences between the Smooth FDK VOI and I4D VOI become more apparent for 1 minute scan times (especially seen near yellow arrows).

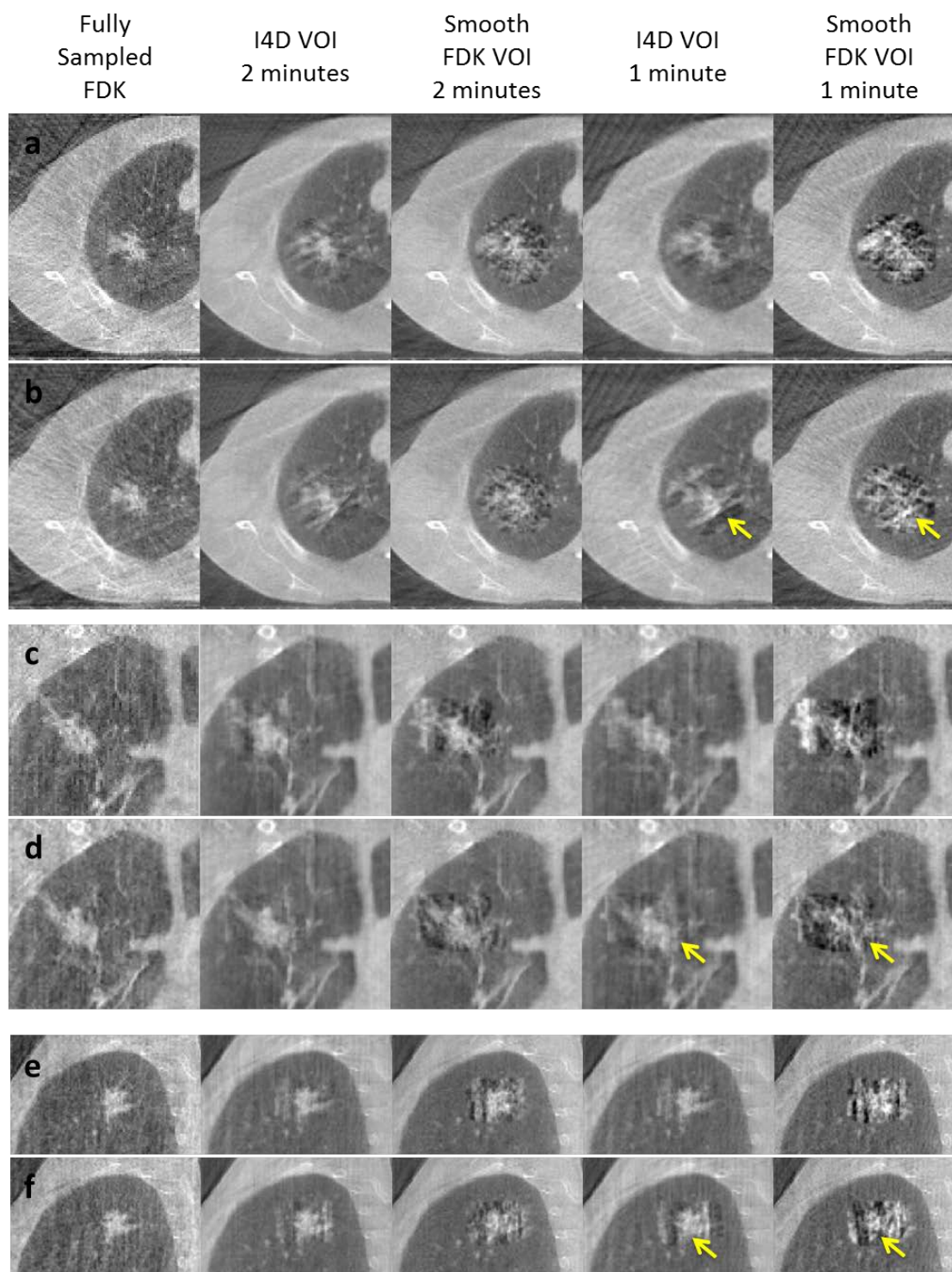


Figure 44: Axial (a, b), coronal (c, d), and sagittal (e, f) slices of peak inhale (a, c, e) and exhale (b, d, f) for 2 and 1 minute VOI reconstructions from left to right: fully sampled FDK, I4D VOI 2 minutes, Smooth FDK 2 minutes, I4D VOI 1 minute, Smooth FDK VOI 1 minute. P108 pictured here represents a difficult case of a small tumor and irregular and long breath cycles. Differences between the Smooth FDK VOI and I4D VOI become more apparent for 1 minute scan times (especially seen near yellow arrows).

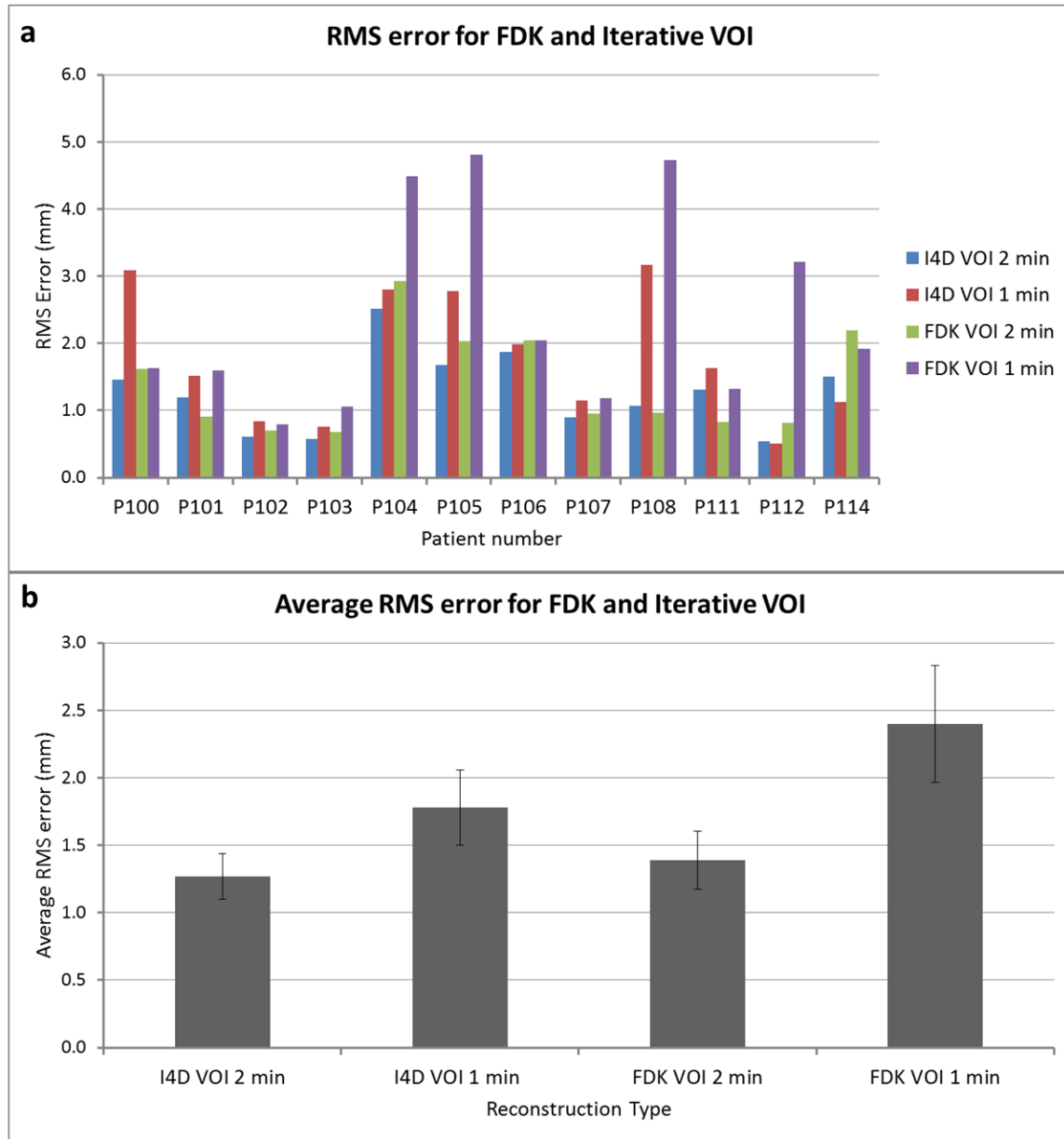


Figure 45: RMS errors for 1 and 2 minute scan time Smooth FDK VOI and I4D VOI reconstructions. Errors for each patient except P110 and P115 are shown in (a) and average (standard error) RMS errors are shown in (b).

5.3.4 Computation time

The reconstruction times for each method were recorded and included in Table 14. Full 4D SIRT reconstruction times were also included for a more direct comparison with TV minimization. The reconstruction times include the reconstruction of all phase images, and, for

I4D VOI, the 3D image. Reconstruction times are divided into time required for the 3D and VOI portions of the reconstruction for I4D VOI. This division is done since by replacing the iterative 3D image with an FDK 3D image the reconstruction time can be reduced to essentially the time for the VOI portion without much loss in image quality. Reconstructions were performed through MATLAB running primarily C code on computer with 18 GB RAM and an Intel Core i7 CPU with 2.67 GHz clock speed. An NVIDIA GeForce GTX 660 GPU was used for the parallel portions of the code. It is important to note that while effort was taken to improve the speed of the reconstructions, including using parallel programming when possible, further optimizations of the hardware and software for speed could be performed as described in the discussion section. Therefore, Table 14 should not be read as the expected computation time for an eventual clinical implementation, but as an approximate comparison of the different reconstruction times. For comparison, Bergner et al⁹² report an increase in computational load for ASD-POCS of 1:4800 over FDK, similar to the increase in computation time for high regularization TV minimization (1:3500 increase over FDK). In an attempt to make comparisons of iterative reconstructions fair, the number of iterations or stopping criteria was chosen to allow for convergence with few iterations past the point where differences in subsequent iterations were observable. The average number of iterations for each reconstruction is included in Table 14.

Table 14: Average reconstruction computation time (minutes) for each reconstruction type

	FDK	I4D VOI	I4D VOI (3D)	I4D VOI (VOI)	SIRT	TV min $\lambda=2$	TV min $\lambda=10$
reconstruction time (mins)	0.2	45.8	38.5	7.3	38.5	111.7	693.0
number of iterations	1	50	50	50	50	20	122

5.4 Discussion

This study demonstrates the improvement of bony anatomy image quality using VOI based reconstructions, which would allow for these images to be used for an initial bony anatomy alignment. As demonstrated by the lack of significant difference in RMS error compared to TV minimization and the overall small RMS errors (maximum 2.5 mm), I4D VOI is able to achieve this improvement in bony anatomy image quality and reconstruction time reduction without sacrificing tumor motion measurement accuracy.

From the relatively small patient population used in this study, no significant difference was observed in tumor motion measurements between I4D VOI and Smooth FDK VOI for either 2 minute or 1 minute scan times. Observed differences in the images (especially at 1 minute) and small p-values suggest that there may be a small difference between the two reconstruction types that could be observed with a larger study. Additionally, the more pronounced difference in tumor visibility between the two reconstruction types in situations with high streak artifacts (1 minute scans, P108) and increase in RMS error difference for 1 minute scans suggest there may be populations of patients or imaging conditions where I4D VOI is advantageous over Smooth FDK VOI. A larger study should be conducted to determine the cohort of patients and imaging conditions where I4D VOI would be beneficial and other patients or conditions where Smooth FDK VOI would suffice.

TV minimization was used in this work as an approximate comparison to what type of streak artifact reduction and image quality that may be expected from optimization based algorithms such as ASD-POCS and PICCS. Additionally, it represents what level of tumor motion accuracy may be achievable with our registration method, since it favors smoother images. While the implementation of TV minimization used in this work is relatively simple and can be

improved upon (such as by the previously mentioned methods), there will always be a tradeoff between streak artifact reduction and spatial resolution. While in TV minimization and similar methods, some general reduction in spatial resolution is accepted for streak artifact reduction, in our method, we sacrifice temporal resolution in the lungs outside of the VOI for streak free and sharp bony anatomy. We found improved image quality inside and outside the VOI compared to FDK and similar tumor motion errors as TV minimization. The VOI constraint can be applied to TV minimization or other reconstructions for potential improvements, at the cost of longer reconstruction times and increased complexity. This is a topic for further research.

Rigid registration was used in this work as it provided a direct comparison between different reconstruction techniques without needing to fine tune parameters for the different image qualities produced by the different reconstructions or for differing amounts of tumor motion. However, rigid registration has its limitations as anatomical motion is inherently non-rigid including the tumor and other structures such as the chest wall or mediastinum moving relative to one another. Additionally, with a VOI reconstruction, shifting the test image during registration results in a comparison of moving portions of the image to the stationary 3D background. For clinical use in quantifying motion, deformable registration optimized for I4D VOI may be beneficial in reducing tumor trajectory errors.

As implemented in this work, the I4D VOI method requires more time than is available in a clinical setting. However, several strategies are available that are expected to reduce the time required for this method to the level of clinical feasibility. In our implementation, the 3D image required the majority of the computation time for this method. As seen from the results, using an FDK image for the 3D image would greatly reduce the overall reconstruction time, while maintaining similar image quality outside the VOI. The VOI portion of the reconstruction

can also benefit from further speed optimization. Using a zero sized VOI, we found that nearly half the time (46% of the time) in the VOI portion of the reconstruction was spent querying each projection pixel to determine if it should be backprojected. Keeping a list of pixels that should be backprojected instead of querying each pixel would therefore likely result in a substantial time decrease for the 4D portion of the reconstruction. Additionally, the computer hardware used in this study does not represent the fastest currently available technology. Using multiple, top-of-the-line GPUs could add a further substantial time decrease. With all of these time-saving techniques implemented, a clinically feasible reconstruction time for the I4D VOI is expected to be achievable with current computer technology.

The size of the VOI used in the I4D VOI reconstruction was chosen as the PTV as this size allows for a convenient method of visually determining if the tumor will remain within the treatment area throughout the treatment. If the tumor remains within the PTV, the clinician should see the whole tumor in each phase without any portion of the tumor being visible in the 3D region or outside the PTV. Additionally, this size lessens the likelihood that the tumor will move in and out the VOI, which could impact registration methods, without adding the unnecessary reconstruction time of a larger VOI. If the tumor does move out of the VOI, a reconstruction with a larger VOI can be retrospectively performed to determine if the amount of tumor motion has changed or if the patient simply needs to be shifted. Since the 3D image would not need to be reconstructed again in this case, the added computation time would be minimal.

In addition to its use in quantifying tumor motion to compare to pre-treatment motion and ensuring the tumor remains in the treatment area, some researchers have suggested 4D CBCT can be used for soft tissue alignment. Since motion blurring is lessened, the tumor can be

registered to planning images such as mid-ventilation 4D CT images to improve registration over bony anatomy alignment.^{84, 85} As the planning CTs were not available for this study, this use of 4D CBCT was not directly tested. However, any reduction in streak artifacts over FDK reconstructions is likely to improve the automatic registration to the streak artifact free planning images and especially manual inspection and adjustments to the registration. As with tumor motion errors, a larger study should be performed to determine which patients would require iterative versus FDK VOI reconstruction to effectively minimize these streak artifacts for this purpose. It should be noted that any soft tissue alignment done with I4D VOI should focus on alignment within the VOI since motion is blurred in the 3D regions or outside the PTV.

5.5 Conclusion

The aim of this chapter was to compare, using a long-scan patient data set, the accuracy of tumor motion determination and bony anatomy image quality of an iterative volume of interest based reconstruction technique for 4D cone-beam CT to existing reconstructions including FDK and TV minimization and to an FDK volume of interest based reconstruction. The hypothesis of this aim was that iterative volume of interest 4D CBCT will improve tumor motion measurements compared to standard FDK and FDK VOI, and will improve computation time with at least as accurate tumor motion measurements as TV minimization. Statistically equivalent tumor motion measurements and decreased computation time compared to TV minimization were observed. However, the difference in tumor motion measurements between I4D VOI and FDK or FDK VOI was not significant with this data set.

Chapter 6: Discussion

In this dissertation we found or tested several methods of improving image quality, quantitative accuracy, and/or workflow in dual energy and 4D computed tomography. Improvements in image quality, quantitative accuracy, and workflow can have a wide array of implications depending on the intended use of the imaging modality. We will now summarize the findings of this dissertation, focusing on the implications and impact of each improvement and areas of future work.

In chapter 2, we discussed the optimization of small animal dual energy cone-beam CT, specifically focusing on the low and high energy kVp. We found an optimal kVp pair, 60kVp for the low energy and 200 kVp for the high energy, for low contrast detectability and precision in Iodine concentration measurements, while not detecting changes in the accuracy of Iodine concentration measurements. Specifically, we observed an 80% increase in CNR and 58% increase in Iodine concentration precision between a standard kVp pair (80kVp/140kVp) and the optimal pair. While other studies have examined the effect of changing the kVp pair on noise or measurement accuracy in both clinical and preclinical settings, most have not looked at energies above 150 kVp and if they did, only examine one representative kVp or use an MV energy scan for the high energy scan. In this study, we showed a continued improvement in CNR and to a lesser extent, Iodine concentration precision, for a range of increasing energies above 140 kVp. Improvements in CNR would allow for either less Iodine to be used, or for more or smaller tumors or other structures of interest to be observed. The former is beneficial since preclinical contrast agents often are expensive, have a short self-life, and require large injection volumes relative to the mouse blood pool, all limiting how often they can be used overall or for an individual animal. The latter is beneficial since it would open up the possibility of imaging structures or tumors not possible before with dual energy or providing a more accurate assessment of disease burden. Improvements in Iodine concentration precision allow for greater confidence or smaller sample

sizes in preclinical studies utilizing a targeted iodine contrast agent. Overall, our results suggest it would be beneficial to invest in higher voltage x-ray tubes (or utilize platforms that already have them, such as the X-RAD) in the design of small animal dual energy CT.

Several limitations were discussed in Chapter 2, including the lack of in vivo studies and noise suppression in the analysis of the optimal kVp pair. These additions represent areas of future work. Noise reduction strategies should be applied and the dependence of CNR on kVp pair should be reevaluated. In vivo studies of mice injected with iodine based contrast agent would allow the evaluation of whether the contrast agent is visible where it is expected, whether CNR within the mouse is sufficient for visualization of iodine filled blood vessels and small areas of iodine buildup, and whether the concentration of iodine observed is within a range where percent errors were observed to be low by our previous experiments.

Bone is often categorized as iodine in dual energy imaging using water and iodine as the basis pairs since its attenuation properties are closer to iodine than water. When imaging iodine filled blood vessels near bone, a dual energy technique that can distinguish the two allow for the distinction between the two. Using a bone substitute and iodine as the material basis pair would allow for such a separation. Bone and iodine are more difficult to distinguish in dual energy than iodine and water due to their similar attenuation curves. It would be interesting to study the effect of increasing energy spectra separation on the ability to distinguish between bone and iodine.

Another method of increasing the separation between the low and high energy spectra is through added filtration. The imaging filter on the X-RAD is removable, so that it can be replaced with a treatment filter. It is feasible, therefore to design custom filters for the low and high energy scans to further increase the spectra separation. Filter materials and thicknesses could be chosen using the simulation package used in this study.

In Chapter 3, we adapted several data driven 4D cone-beam CT methods that had been designed for clinical applications to mice. These data driven methods used projection images that are already available when performing CBCT to form the necessary respiratory signal for 4D CBCT or gated CBCT. Additionally, we modified previous techniques to automatically determine the peak inspirations of these respiratory signals for use in sorting projections for 4D CBCT. Modifications to the clinical methods were especially needed for the Amsterdam Shroud method. The resulting modified Amsterdam Shroud method and an intensity sum method had projection sorting errors of less than 2% of a phase, which was significantly better than the translated Fourier transform phase method or the previously implemented center of mass method. Errors in tumor motion measurement and increased image blurring were observed for high sorting error, illustrating the importance of projection sorting accuracy. Additionally, the modified Amsterdam Shroud and Intensity methods showed the least sensitivity to the placement of the region of interest (to focus the measurements on the diaphragm), which would minimize large errors for a fully automated data driven method.

Small animal 4D CBCT and gated CBCT have a number of potential uses including determining motion management strategies or defining a target area including tumor motion for radiation treatments. While historically, small animal radiation treatment studies have irradiated the whole lung, preclinical irradiators with precision capable of targeting just the tumor allow for treatments that more closely mimic what is delivered clinically and increase the importance of technologies like 4D CBCT. The improved projection sorting accuracy and associated tumor motion measurement accuracy demonstrated in this work contributes to obtaining more clinically realistic treatments in small animals. As mentioned previously, gated CBCT can be used to improve the localization of quantification of Iodine in sequential scanning dual energy CBCT, largely by reducing image blurring. The improved projection sorting accuracy and the associated decrease in image blurring demonstrated in this work would therefore be beneficial to dual energy CBCT.

Areas of future work for this project include ensuring that the tested data driven methods work on other imaging platforms and for other strains of mice and fully automating the process, including ROI placement. Additionally, these techniques can be coupled with small animal dual energy imaging for further optimization of that imaging technique.

In Chapter 4, we studied similar data driven techniques in clinical 4D CT. In this case, a product was already clinically available, but had not been tested independently in its final form. One contribution of this dissertation is to test this technique to ensure that no change in how target volumes are defined is needed and if artifacts can be decreased. We found no significant difference in target volume and a decrease in artifacts when using this data driven 4D CT compared to standard 4D CT. Difference in target volumes in individual patients were often related to the decrease in artifacts. These results can inform physicists' decisions on the use of this technology and increase confidence in target volumes defined from it. Future work could include the evaluation of the clinical impact of artifact reduction from data driven 4D CT on physician definitions of contours, IGTVs defined using deformable image registration to contour phase images, and measurement of tumor motion.

In Chapter 5, we turned our attention to another form of clinical 4D imaging used in radiation therapy, 4D CBCT. While 4D CT is used to evaluate tumor motion prior to the start of treatment, 4D CBCT can be used to ensure tumor motion does not change in a clinically relevant way over the course of treatment. In this dissertation, we tested an iterative volume of interest (I4D VOI) based strategy for reducing the impact of the streak artifacts that plague 4D CBCT with traditional reconstruction. I4D VOI and one reconstruction it was compared against, FDK VOI, were proposed by former student, Moiz Ahmad. However, several modifications were made in this dissertation to improve the continuity between the volume of interest and the background image, including adding Gaussian smoothing to FDK VOI and the edge discontinuity corrections described in Chapter 5. The main contribution of this

dissertation in this area was to compare I4D VOI to FDK VOI and other reconstruction methods in a larger patient data set, examining image quality differences and tumor motion measurement accuracy. We found that I4D VOI performed as well as the more computationally heavy TV minimization reconstruction in terms of tumor motion measurements, and had superior bony anatomy image quality. That I4D VOI performs as well as more computationally advanced reconstructions is important, since with some proposed modifications, I4D VOI could reasonably be performed within the time limits of a radiation therapy treatment. While bony anatomy image quality was improved over standard FDK for both VOI based reconstructions, we were not able to show an improvement in tumor motion measurement between I4D VOI and FDK VOI or standard FDK. However, the data suggested there may be populations of patients and/or imaging conditions where I4D VOI would represent an improvement over FDK VOI.

Before widespread use of VOI based 4D CBCT, several areas of future work should be addressed. One is to determine which patients and under what imaging conditions I4D VOI should be used in place of FDK VOI. A larger patient population would be required for this study. Ideally, long scan CBCT taken with respiratory monitoring would be performed prior to patients' treatments which could be retrospectively reconstructed and compared to a gold standard as with this study. More realistically, 2 or 1 minute CBCT scans with respiratory monitoring could be performed and I4D VOI and FDK VOI could be compared using metrics such as the difference in tumor motion measurement between the two, measured tumor volume, a more quantitative assessment of streak artifacts, and/or physician evaluation. Additionally, these VOI based reconstructions should be applied and tested in small animals, to improve reconstruction time in preclinical 4D CBCT.

Overall, this dissertation sought to address the hypothesis:

Improvements can be made in image quality, quantitative accuracy, and/or workflow to small animal dual energy CT by increasing energy spectra separation and to human and small animal 4D CT imaging by using data driven techniques to obtain the respiratory signal and using a volume of interest based reconstruction.

We show how the hypothesis was addressed by outlining the types of improvements that were made or shown.

For mice:

1. CNR (image quality) was improved by increasing energy spectra separation in dual energy CBCT. Precision, but not accuracy, in Iodine concentration (quantitative accuracy) was also improved by increasing energy spectra separation. (Specific Aim 1)
2. Data driven 4D CBCT methods translated from humans to mice improved projection sorting (quantitative accuracy) over previous methods. Improved projection sorting was demonstrated to be related to improved tumor motion measurement (quantitative accuracy) and less image blurring (image quality). Data driven methods do not require additional setup beyond 3D imaging (workflow).

For humans:

1. Improvements in artifact severity (image quality) over standard methods were shown for a clinically available implementation of data driven 4D CT. (Specific Aim 2)
2. Improvements over standard and more advanced reconstructions in bony anatomy visualization (image quality) were shown for iterative volume of interest based 4D CBCT (I4D VOI). Streak artifacts (image quality) were reduced somewhat compared to FDK and FDK VOI

reconstructions, especially for short scan times, although further work is needed to verify.

Improvements in tumor motion measurement (quantitative accuracy) over FDK VOI were not shown conclusively with this data set. Improvements in reconstruction time (workflow) over TV minimization were observed. (Specific Aim 3)

Bibliography

1. G. C. Kagadis, G. Loudos, K. Katsanos, S. G. Langer and G. C. Nikiforidis, "In vivo small animal imaging: Current status and future prospects", *Medical Physics* **37** (12), 6421-6442 (2010).
2. M. J. Paulus, S. S. Gleason, S. J. Kennel, P. R. Hunsicker and D. K. Johnson, "High resolution X-ray computed tomography: An emerging tool for small animal cancer research", *Neoplasia* **2** (1-2), 62-70 (2000).
3. S. H. Bartling, W. Stiller, W. Semmler and F. Kiessling, "Small animal computed tomography imaging", *Current Medical Imaging Reviews* **3** (1), 45-59 (2007).
4. E. L. Ritman, "Small-animal CT: Its difference from, and impact on, clinical CT", *Nuclear Instruments and Methods in Physics Research, Section A: Accelerators, Spectrometers, Detectors and Associated Equipment* **580** (2), 968-970 (2007).
5. F. Hallouard, N. Anton, P. Choquet, A. Constantinesco and T. Vandamme, "Iodinated blood pool contrast media for preclinical X-ray imaging applications - A review", *Biomaterials* **31** (24), 6249-6268 (2010).
6. E. J. Moding, D. P. Clark, Y. Qi, Y. Li, Y. Ma, K. Ghaghada, G. A. Johnson, D. G. Kirsch and C. T. Badea, "Dual-energy micro-computed tomography imaging of radiation-induced vascular changes in primary mouse sarcomas", *Int J Radiat Oncol Biol Phys* **85** (5), 1353-1359 (2013).
7. X. Fouillet, H. Tournier, H. Khan, S. Sabitha, S. Burkhardt, F. Terrier and M. Schneider, "Enhancement of computed tomography liver contrast using iomeprol-containing liposomes and detection of small liver tumors in rats", *Acad Radiol* **2** (7), 576-583 (1995).

8. X. Montet, C. M. Pastor, J. P. Vallée, C. D. Becker, A. Geissbuhler, D. R. Morel and P. Meda, "Improved visualization of vessels and hepatic tumors by micro-Computed Tomography (CT) using iodinated liposomes", *Investigative Radiology* **42** (9), 652-658 (2007).
9. C. T. Badea, K. K. Athreya, G. Espinosa, D. Clark, A. P. Ghafoori, Y. Li, D. G. Kirsch, G. A. Johnson, A. Annapragada and K. B. Ghaghada, "Computed tomography imaging of primary lung cancer in mice using a liposomal-iodinated contrast agent", *PLoS One* **7** (4), e34496 (2012).
10. K. H. Diehl, R. Hull, D. Morton, R. Pfister, Y. Rabemampianina, D. Smith, J. M. Vidal and C. Van De Vorstenbosch, "A good practice guide to the administration of substances and removal of blood, including routes and volumes", *Journal of Applied Toxicology* **21** (1), 15-23 (2001).
11. R. E. Alvarez and A. Macovski, "Energy-selective reconstructions in X-ray computerized tomography", *Phys Med Biol* **21** (5), 733-744 (1976).
12. R. A. Rutherford, B. R. Pullan and I. Isherwood, "Measurement of effective atomic number and electron density using an EMI scanner", *Neuroradiology* **11** (1), 15-21 (1976).
13. S. M. Johnston, G. A. Johnson and C. T. Badea, "Temporal and spectral imaging with micro-CT", *Med Phys* **39** (8), 4943-4958 (2012).
14. C. T. Badea, X. Guo, D. Clark, S. M. Johnston, C. D. Marshall and C. A. Piantadosi, "Dual-energy micro-CT of the rodent lung", *Am J Physiol Lung Cell Mol Physiol* **302** (10), L1088-1097 (2012).
15. P. V. Granton, S. I. Pollmann, N. L. Ford, M. Drangova and D. W. Holdsworth, "Implementation of dual- and triple-energy cone-beam micro-CT for postreconstruction material decomposition", *Med Phys* **35** (11), 5030-5042 (2008).
16. C. Bouckaert, B. Vandeghinste, C. Vanhove and S. Vandenberghe, 2012 (unpublished).

17. L. E. J. R. Schyns, I. P. Almeida, S. J. Van Hoof, B. Descamps, C. Vanhove, G. Landry, P. V. Granton and F. Verhaegen, "Optimizing dual energy cone beam CT protocols for preclinical imaging and radiation research", *British Journal of Radiology* **90** (1069) (2017).
18. F. Kelcz, P. M. Joseph and S. K. Hilal, "Noise considerations in dual energy CT scanning", *Med Phys* **6** (5), 418-425 (1979).
19. A. N. Primak, J. C. Ramirez Giraldo, X. Liu, L. Yu and C. H. McCollough, "Improved dual-energy material discrimination for dual-source CT by means of additional spectral filtration", *Med Phys* **36** (4), 1359-1369 (2009).
20. R. A. Rutherford, B. R. Pullan and I. Isherwood, "X ray energies for effective atomic number determination", *Neuroradiology* **11** (1), 23-28 (1976).
21. N. L. Ford, H. N. Nikolov, C. J. D. Norley, M. M. Thornton, P. J. Foster, M. Drangova and D. W. Holdsworth, "Prospective respiratory-gated micro-CT of free breathing rodents", *Med. Phys.* **32** (9), 2888-2898 (2005).
22. A. Kavanagh, P. M. Evans, V. N. Hansen and S. Webb, "Obtaining breathing patterns from any sequential thoracic x-ray image set", *Phys Med Biol* **54** (16), 4879-4888 (2009).
23. J. J. Sonke, L. Zijp, P. Remeijer and M. Van Herk, "Respiratory correlated cone beam CT", *Medical Physics* **32** (4), 1176-1186 (2005).
24. L. Zijp, J.-J. Sonke and M. van Herk, in *International Conference on the Use of Computers in Radiation Therapy* (Jeong Publishing, 2004), pp. 507-509.
25. H. Yan, X. Wang, W. Yin, T. Pan, M. Ahmad, X. Mou, L. Cerviño, X. Jia and S. B. Jiang, "Extracting respiratory signals from thoracic cone beam CT projections", *Phys Med Biol* **58** (5), 1447-1464 (2013).

26. I. Vergalasova, J. Cai, W. Giles, W. P. Segars and F. F. Yin, "Evaluation of the effect of respiratory and anatomical variables on a Fourier technique for markerless, self-sorted 4D-CBCT", *Phys Med Biol* **58** (20), 7239-7259 (2013).
27. I. Vergalasova, J. Cai and F. F. Yin, "A novel technique for markerless, self-sorted 4D-CBCT: Feasibility study", *Med. Phys.* **39** (3), 1442-1451 (2012).
28. C. Chavarrías, J. J. Vaquero, A. Sisniega, A. Rodríguez-Ruano, M. L. Soto-Montenegro, P. García-Barreno and M. Desco, "Extraction of the respiratory signal from small-animal CT projections for a retrospective gating method", *Phys Med Biol* **53** (17), 4683-4695 (2008).
29. J. Hu, S. T. Haworth, R. C. Molthen and C. A. Dawson, "Dynamic small animal lung imaging via a postacquisition respiratory gating technique using micro-cone beam computed tomography", *Acad Radiol* **11** (9), 961-970 (2004).
30. S. H. Bartling, J. Dinkel, W. Stiller, M. Grasruck, I. Madisch, H. U. Kauczor, W. Semmler, R. Gupta and F. Kiessling, "Intrinsic respiratory gating in small-animal CT", *Eur Radiol* **18** (7), 1375-1384 (2008).
31. J. Kuntz, J. Dinkel, S. Zwick, T. Bäuerle, M. Grasruck, F. Kiessling, R. Gupta, W. Semmler and S. H. Bartling, "Fully automated intrinsic respiratory and cardiac gating for small animal CT", *Phys Med Biol* **55** (7), 2069-2085 (2010).
32. D. Ertel, Y. Kyriakou, R. M. Lapp and W. A. Kalender, "Respiratory phase-correlated micro-CT imaging of free-breathing rodents", *Phys Med Biol* **54** (12), 3837-3846 (2009).
33. F. Verhaegen, P. Granton and E. Tryggestad, "Small animal radiotherapy research platforms", *Physics in Medicine and Biology* **56** (12), R55-R83 (2011).

34. R. Clarkson, P. E. Lindsay, S. Ansell, G. Wilson, S. Jelveh, R. P. Hill and D. A. Jaffray, "Characterization of image quality and image-guidance performance of a preclinical microirradiator", *Medical Physics* **38** (2), 845-856 (2011).
35. M. Ahmad, P. Balter and T. Pan, "Four-dimensional volume-of-interest reconstruction for cone-beam computed tomography-guided radiation therapy", *Medical Physics* **38** (10), 5646-5656 (2011).
36. D. A. Low, M. Nystrom, E. Kalinin, P. Parikh, J. F. Dempsey, J. D. Bradley, S. Mutic, S. H. Wahab, T. Islam, G. Christensen, D. G. Polite and B. R. Whiting, "A method for the reconstruction of four-dimensional synchronized CT scans acquired during free breathing", *Medical Physics* **30** (6), 1254-1263 (2003).
37. T. Pan, T. Y. Lee, E. Rietzel and G. T. Y. Chen, "4D-CT imaging of a volume influenced by respiratory motion on multi-slice CT", *Medical Physics* **31** (2), 333-340 (2004).
38. E. Rietzel, T. Pan and G. T. Y. Chen, "Four-dimensional computed tomography: Image formation and clinical protocol", *Medical Physics* **32** (4), 874-889 (2005).
39. E. Rietzel, G. T. Y. Chen, N. C. Choi and C. G. Willet, "Four-dimensional image-based treatment planning: Target volume segmentation and dose calculation in the presence of respiratory motion", *International Journal of Radiation Oncology*Biophysics* **61** (5), 1535-1550 (2005).
40. M. Ezhil, S. Vedam, P. Balter, B. Choi, D. Mirkovic, G. Starkschall and J. Y. Chang, "Determination of patient-specific internal gross tumor volumes for lung cancer using four-dimensional computed tomography", *Radiation Oncology* **4** (2009).

41. J. D. P. Hoisak, K. E. Sixel, R. Tirona, P. C. F. Cheung and J. P. Pignol, "Correlation of lung tumor motion with external surrogate indicators of respiration", *International Journal of Radiation Oncology Biology Physics* **60** (4), 1298-1306 (2004).
42. C. Ozhasoglu and M. J. Murphy, "Issues in respiratory motion compensation during external-beam radiotherapy", *International Journal of Radiation Oncology Biology Physics* **52** (5), 1389-1399 (2002).
43. P. C. M. Chi, P. Balter, D. Luo, R. Mohan and T. Pan, "Relation of external surface to internal tumor motion studied with cine CT", *Medical Physics* **33** (9), 3116-3123 (2006).
44. R. Li, J. H. Lewis, L. I. Cerv o and S. B. Jiang, "4D CT sorting based on patient internal anatomy", *Physics in Medicine and Biology* **54** (15), 4821-4833 (2009).
45. C. Hui, Y. Suh, D. Robertson, T. Pan, P. Das, C. H. Crane and S. Beddar, "Internal respiratory surrogate in multislice 4D CT using a combination of Fourier transform and anatomical features", *Medical Physics* **42** (7), 4338-4348 (2015).
46. G. Carnes, S. Gaede, E. Yu, J. Van Dyk, J. Battista and T.-Y. Lee, "A fully automated non-external marker 4D-CT sorting algorithm using a serial cine scanning protocol", *Physics in Medicine and Biology* **54** (7), 2049 (2009).
47. S. Xu, R. H. Taylor, G. Fichtinger and K. Cleary, "Lung Deformation Estimation and Four-dimensional CT Lung Reconstruction", *Academic Radiology* **13** (9), 1082-1092 (2006).
48. R. Zeng, J. A. Fessler, J. M. Balter and P. A. Balter, "Iterative sorting for four-dimensional CT images based on internal anatomy motion", *Medical Physics* **35** (3), 917-926 (2008).

49. Smart Deviceless 4D. Retrived December 6, 2016, from http://www3.gehealthcare.com/en/products/categories/computed_tomography/radiation_therapy_planning/smart_deviceless_4d.
50. H. Shirato, K. Suzuki, G. C. Sharp, K. Fujita, R. Onimaru, M. Fujino, N. Kato, Y. Osaka, R. Kinoshita, H. Taguchi, S. Onodera and K. Miyasaka, "Speed and amplitude of lung tumor motion precisely detected in four-dimensional setup and in real-time tumor-tracking radiotherapy", International Journal of Radiation Oncology Biology Physics **64** (4), 1229-1236 (2006).
51. G. Poludniowski, G. Landry, F. DeBlois, P. M. Evans and F. Verhaegen, "SpekCalc: a program to calculate photon spectra from tungsten anode x-ray tubes", Phys Med Biol **54** (19), N433-438 (2009).
52. G. G. Poludniowski and P. M. Evans, "Calculation of x-ray spectra emerging from an x-ray tube. Part I. electron penetration characteristics in x-ray targets", Med Phys **34** (6), 2164-2174 (2007).
53. G. G. Poludniowski, "Calculation of x-ray spectra emerging from an x-ray tube. Part II. X-ray production and filtration in x-ray targets", Med Phys **34** (6), 2175-2186 (2007).
54. S. Richard and J. H. Siewerdsen, "Optimization of dual-energy imaging systems using generalized NEQ and imaging task", Medical Physics **34** (1), 127-139 (2007).
55. N. A. Shkumat, J. H. Siewerdsen, A. C. Dhanantwari, D. B. Williams, S. Richard, N. S. Paul, J. Yorkston and R. Van Metter, "Optimization of image acquisition techniques for dual-energy imaging of the chest", Medical Physics **34** (10), 3904-3915 (2007).
56. I. A. Feldkamp, L. C. Davis and J. W. Kress, "PRACTICAL CONE-BEAM ALGORITHM", Journal of the Optical Society of America A: Optics and Image Science, and Vision **1** (6), 612-619 (1984).

57. C. Maaß, M. Baer and M. Kachelrieß, "Image-based dual energy CT using optimized precorrection functions: A practical new approach of material decomposition in image domain", *Medical Physics* **36** (8), 3818-3829 (2009).
58. W. A. Kalender, E. Klotz and L. Kostaridou, "Algorithm for noise suppression in dual energy ct material density images", *IEEE Transactions on Medical Imaging* **7** (3), 218-224 (1988).
59. R. J. Warp and J. T. Dobbins, 3rd, "Quantitative evaluation of noise reduction strategies in dual-energy imaging", *Med Phys* **30** (2), 190-198 (2003).
60. S. C. Kappadath and C. C. Shaw, "Dual-energy digital mammography for calcification imaging: noise reduction techniques", *Phys Med Biol* **53** (19), 5421-5443 (2008).
61. C. H. McCollough, M. S. Van Lysel, W. W. Pepler and C. A. Mistretta, "A correlated noise reduction algorithm for dual-energy digital subtraction angiography", *Med Phys* **16** (6), 873-880 (1989).
62. B. Li, B. Li, J. Luo, P. Tang, J. Mao and X. Wu, "Simultaneous reduction in noise and cross-contamination artifacts for dual-energy x-ray CT", *BioMed Research International* **2013** (2013).
63. R. Martin, A. Rubinstein, M. Ahmad, L. Court and T. Pan, "Evaluation of intrinsic respiratory signal determination methods for 4D CBCT adapted for mice", *Medical Physics* **42** (1) (2015).
64. A. Vinegar, E. E. Sinnett and D. E. Leith, "Dynamic mechanisms determine functional residual capacity in mice, *Mus musculus*", *Journal of Applied Physiology Respiratory Environmental and Exercise Physiology* **46** (5), 867-871 (1979).
65. A. Rubinstein, J. Yang, R. Martin, C. Kingsley, J. Delacerda, K. Michel, L. Zhang, R. Taylor, T. Pan, P. Yang, J. Hazel and L. Court, "Respiratory Motion Management for High-Precision Small Animal Irradiation", *Medical Physics* **40** (6), 116 (2013).

66. R. Martin and T. Pan, "Target volume and artifact evaluation of a new data-driven 4D CT", Practical Radiation Oncology (2016).
67. P. Liu, J. Dong and S. Wang, U.S. Patent No. US20130195341 A1 (2013).
68. E. Rietzel, A. K. Liu, G. T. Y. Chen and N. C. Choi, "Maximum-Intensity Volumes for Fast Contouring of Lung Tumors Including Respiratory Motion in 4DCT Planning", International Journal of Radiation Oncology*Biology*Physics **71** (4), 1245-1252 (2008).
69. R. W. M. Underberg, F. J. Lagerwaard, B. J. Slotman, J. P. Cuijpers and S. Senan, "Use of maximum intensity projections (MIP) for target volume generation in 4DCT scans for lung cancer", International Journal of Radiation Oncology*Biology*Physics **63** (1), 253-260 (2005).
70. D. A. Zamora, A. C. Riegel, X. Sun, P. Balter, G. Starkschall, O. Mawlawi and T. Pan, "Thoracic target volume delineation using various maximum-intensity projection computed tomography image sets for radiotherapy treatment planning", Medical Physics **37** (11), 5811-5820 (2010).
71. A. C. Riegel, J. Y. Chang, S. S. Vedam, V. Johnson, P. C. M. Chi and T. Pan, "Cine Computed Tomography Without Respiratory Surrogate in Planning Stereotactic Radiotherapy for Non-Small-Cell Lung Cancer", International Journal of Radiation Oncology Biology Physics **73** (2), 433-441 (2009).
72. L. R. Dice, "Measures of the Amount of Ecologic Association Between Species", Ecology **26** (3), 297-302 (1945).
73. K. H. Zou, S. K. Warfield, A. Bharatha, C. M. C. Tempany, M. R. Kaus, S. J. Haker, W. M. Wells Iii, F. A. Jolesz and R. Kikinis, "Statistical Validation of Image Segmentation Quality Based on a Spatial Overlap Index", Academic Radiology **11** (2), 178-189 (2004).

74. A. P. Zijdenbos, B. M. Dawant, R. A. Margolin and A. C. Palmer, "Morphometric Analysis of White Matter Lesions in MR Images: Method and Validation", *IEEE Transactions on Medical Imaging* **13** (4), 716-724 (1994).
75. G. Cui, B. Jew, J. C. Hong, E. W. Johnston, B. W. Loo Jr and P. G. Maxim, "An automated method for comparing motion artifacts in cine four-dimensional computed tomography images", *Journal of applied clinical medical physics / American College of Medical Physics* **13** (6), 3838 (2012).
76. P. Bowden, R. Fisher, M. Mac Manus, A. Wirth, G. Duchesne, M. Millward, A. McKenzie, J. Andrews and D. Ball, "Measurement of lung tumor volumes using three-dimensional computer planning software", *International Journal of Radiation Oncology Biology Physics* **53** (3), 566-573 (2002).
77. J. Van de Steene, N. Linthout, J. de Mey, V. Vinh-Hung, C. Claassens, M. Noppen, A. Bel and G. Storme, "Definition of gross tumor volume in lung cancer: inter-observer variability", *Radiotherapy and Oncology* **62** (1), 37-49 (2002).
78. I. S. Grills, G. Hugo, L. L. Kestin, A. P. Galerani, K. K. Chao, J. Wloch and D. Yan, "Image-Guided Radiotherapy via Daily Online Cone-Beam CT Substantially Reduces Margin Requirements for Stereotactic Lung Radiotherapy", *International Journal of Radiation Oncology Biology Physics* **70** (4), 1045-1056 (2008).
79. D. Létourneau, R. Wong, D. Moseley, M. B. Sharpe, S. Ansell, M. Gospodarowicz and D. A. Jaffray, "Online planning and delivery technique for radiotherapy of spinal metastases using cone-beam CT: Image quality and system performance", *International Journal of Radiation Oncology Biology Physics* **67** (4), 1229-1237 (2007).

80. T. G. Purdie, J. P. Bissonnette, K. Franks, A. Bezjak, D. Payne, F. Sie, M. B. Sharpe and D. A. Jaffray, "Cone-Beam Computed Tomography for On-Line Image Guidance of Lung Stereotactic Radiotherapy: Localization, Verification, and Intrafraction Tumor Position", *International Journal of Radiation Oncology Biology Physics* **68** (1), 243-252 (2007).
81. L. Dietrich, S. Jetter, T. Tücking, S. Nill and U. Oelfke, "Linac-integrated 4D cone beam CT: First experimental results", *Physics in Medicine and Biology* **51** (11), 2939-2952 (2006).
82. S. Kriminski, M. Mitschke, S. Sorensen, N. M. Wink, P. E. Chow, S. Tenn and T. D. Solberg, "Respiratory correlated cone-beam computed tomography on an isocentric C-arm", *Physics in Medicine and Biology* **50** (22), 5263-5280 (2005).
83. J. Lu, T. M. Guerrero, P. Munro, A. Jeung, P. C. M. Chi, P. Balter, X. R. Zhu, R. Mohan and T. Pan, "Four-dimensional cone beam CT with adaptive gantry rotation and adaptive data sampling", *Medical Physics* **34** (9), 3520-3529 (2007).
84. J. J. Sonke, M. Rossi, J. Wolthaus, M. van Herk, E. Damen and J. Belderbos, "Frameless Stereotactic Body Radiotherapy for Lung Cancer Using Four-Dimensional Cone Beam CT Guidance", *International Journal of Radiation Oncology Biology Physics* **74** (2), 567-574 (2009).
85. J.-J. Sonke, J. Lebesque and M. van Herk, "Variability of Four-Dimensional Computed Tomography Patient Models", *International Journal of Radiation Oncology*Biological*Physics* **70** (2), 590-598 (2008).
86. T. Li and L. Xing, "Optimizing 4D cone-beam CT acquisition protocol for external beam radiotherapy", *International Journal of Radiation Oncology*Biological*Physics* **67** (4), 1211-1219 (2007).

87. E. J. Candès, J. Romberg and T. Tao, "Robust uncertainty principles: Exact signal reconstruction from highly incomplete frequency information", *IEEE Transactions on Information Theory* **52** (2), 489-509 (2006).
88. E. Y. Sidky, C. M. Kao and X. Pan, "Accurate image reconstruction from few-views and limited-angle data in divergent-beam CT", *Journal of X-Ray Science and Technology* **14** (2), 119-139 (2006).
89. E. Y. Sidky and X. Pan, "Image reconstruction in circular cone-beam computed tomography by constrained, total-variation minimization", *Physics in Medicine and Biology* **53** (17), 4777-4807 (2008).
90. G. H. Chen, J. Tang and S. Leng, "Prior image constrained compressed sensing (PICCS): A method to accurately reconstruct dynamic CT images from highly undersampled projection data sets", *Medical Physics* **35** (2), 660-663 (2008).
91. S. Leng, J. Tang, J. Zambelli, B. Nett, R. Tolakanahalli and G. H. Chen, "High temporal resolution and streak-free four-dimensional cone-beam computed tomography", *Physics in Medicine and Biology* **53** (20), 5653-5673 (2008).
92. F. Bergner, T. Berkus, M. Oelhafen, P. Kunz, T. Pan, R. Grimmer, L. Ritschl and M. Kachelrie, "An investigation of 4D cone-beam CT algorithms for slowly rotating scanners", *Medical Physics* **37** (9), 5044-5053 (2010).
93. M. Ahmad, "Design and Optimization of Four-dimensional Cone-beam Computed Tomography in Image-guided Radiation Therapy", *UT GSBS Dissertations and Theses*, (2012).
94. G. D. Hugo, E. Weiss, W. C. Sleeman, S. Balik, P. J. Keall, J. Lu and J. F. Williamson, "A longitudinal four-dimensional computed tomography and cone beam computed tomography dataset for image-guided radiation therapy research in lung cancer", *Medical physics* **44** (2), 762-771 (2017).

Vita

Rachael Marianne Martin was born in Pasadena, California on March 9, 1987, the daughter of Elaine Marie Waters Martin and Robert Charles Martin. After completing her work at Pasadena High School, Pasadena, California in 2005, she entered Harvey Mudd College in Claremont, California. She received the degree of Bachelor of Science with a major in physics from Mudd in May, 2009. In August of 2011 she entered The University of Texas MD Anderson Cancer Center UTHealth Graduate School of Biomedical Sciences.

Permanent Address:

4045 Linkwood Drive Apartment 826
Houston, Texas 77025